Fractal Geometries: Scaling of Intrinsic Volumes

Masterarbeit aus der Physik

Vorgelegt von

Philipp Schönhöfer

3. November 2014

Institut für Theoretische Physik I
Friedrich-Alexander-Universität Erlangen-Nürnberg

1. Gutachter: Prof. Dr. Klaus Mecke
2. Gutachter: PD Dr. Gerd Schröder-Turk

Contents

1. Introduction

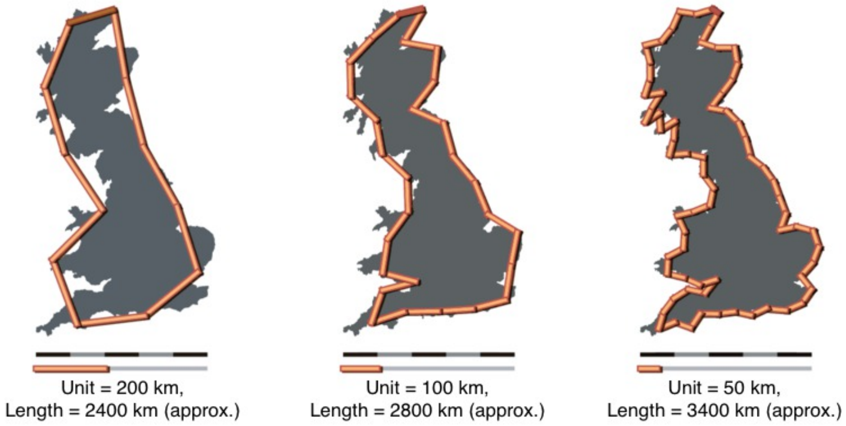

Figure 1.1.: The coast of Britain is measured with different length scales [2].

“. . . consider a stretch of coastline. (. . .) the typical coastline is irregular and winding and there is no question it is much longer than the straight line between its end points. (. . .) The coastline length turns out to be an elusive notion that slips between the fingers of one who wants to grasp it. All measurement methods ultimately lead to a conclusion that the typical coastline’s length is very large and so ill determined that it is best considered infinite. Hence, if one wishes to compare different coastlines from the viewpoint of their “extent”, length is an inadequate concept.”[1]
– Mandelbrot, 1982

In 1967 Benoît B. Mandelbrot asked the question how long the coast of Britain is? Since then self-similar structures gained great attention in mathematics and scientific studies [3]. Mandelbrot noticed that traditional geometry was inadequate to describe shapes like a rough coastline. In this example the coast length differs depending on the scale δ that is used for its measurement: By decreasing the scale, the path is covered more precisely and the length increases (see Fig. 1.1). Eventually, the length diverges to infinity. Mandelbrot realized that he had to introduce an alternative description leading to fractal geometry to compare Britain with coastlines of other countries. In this new approach structures are described by fractal dimensions which are not implicitly integers but rather real numbers. The fractal dimension determines the scaling behavior of the n-dimensional volume F of the fractal due to δ [4]

$$F \propto \delta^{-d_f}. \tag{1.1}$$

n is the topological dimension of the structure and the maximum value which the fractal dimension can attain. The fractal dimension of the west coast of Great Britain is $d_{\mathrm{GB}} = 1.25$, as measured by L. F. Richardson and cited by Mandelbrot [3].

Since publication of the book *The Fractal Geometry of Nature* [1] in 1982, these so called fractals were studied in many areas of science like biology, medicine, and economics [5, 6, 7]. For physicists, the more interesting fractals are fractals occurring in physical processes. For instance, the distribution of galaxies in astronomy or fractal properties of cosmic string networks in cosmology are modeled by fractals [8, 9]. Especially in statistical physics fractals are important. At some sorts of phase transitions a property becomes apparent which is typical for fractal structures [10, 11]. Here we concern about self-similarity. Self-similarity means that objects have the equal statistical properties for different scales. A stronger version is the scale invariance where this applies for all scales. In this context the coastline is a good example for scale invariance as well. By considering parts of a coast, one notices that its physical appearance does not change qualitatively when zooming out or into the scenery (see Fig. 1.2). Consequently, it is not possible to

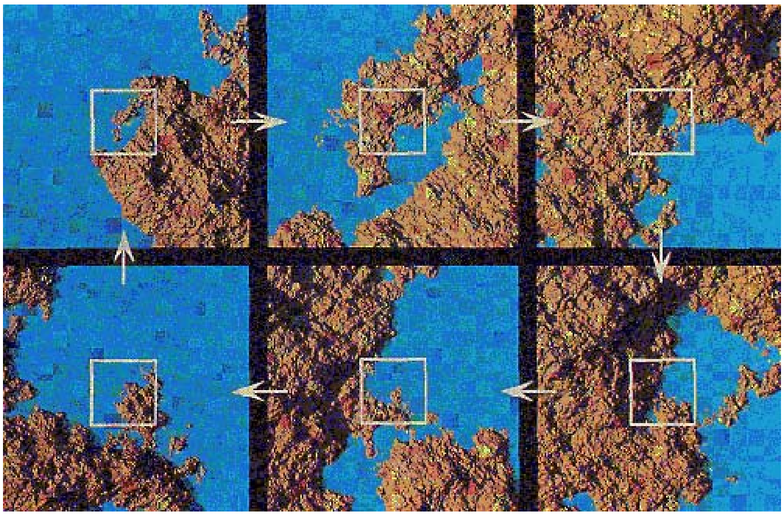

Figure 1.2.: A coastline is observed within different scaled observation windows. The scale invariance becomes apparent [12].

determine the scale of the observation window without any further information.

To explain the motivation and aim behind this Master's thesis, the thesis can be divided into one smaller and into one bigger topic. In all the scientific areas mentioned above where fractals are used it is a challenge to describe certain processes or structures by characterizing them by fractals. Therefore, the simulation of fractals is an important topic in computational physics. This is the reason why it is of great interest to improve the simulation techniques to be able to work with larger objects and, with that included, to decrease simulation time. To check the validity of the construction algorithms, the fractal dimensions are calculated. The algorithm is tested whether the objects are produced correctly thereby. For most fractals the fractal dimension is indeed enough to characterize and thus to distinguish distinct objects. Nevertheless, sometimes the fractal dimension alone is insufficient and more information is needed to characterize shape. The Viscek box fractals are one example (see Fig. 1.3) [13, 14]. Both fractals look similar: one looks like the other one rotated by an angle of 45°. This also shows in the fractal dimension of both being $\frac{\ln 5}{\ln 3}$. However, they are not the same because one is built out of crosses and one out of Xs. As a consequence, an extension to the fractal dimension is necessary to differentiate the structures mathematically. The first and bigger topic investigated in this thesis is the determination of additional fractal dimensions which are not only based on the volume of the object. The scale behaviors of other properties like the boundary length U and the Euler characteristics χ of the fractal $\mathcal{F}$ are examined. In the process the fractals are observed within different sized observation windows W with length x. This scaling of the window length x corresponds to the scaling of the inverse measurement length δ (see chapter 2.2). Eq. (1.1) changes to $F \propto x^{d_f}$. Using the very same example of the Viscek box fractals, it was conjectured [15] that U and χ are further characterized by

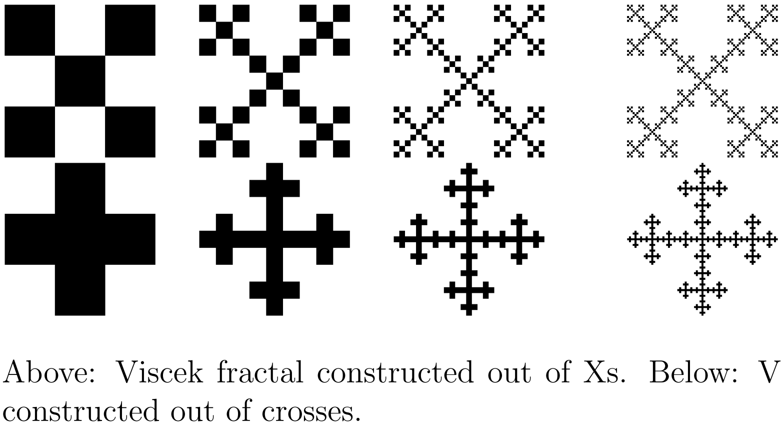

Figure 1.3.: Above: Viscek fractal constructed out of Xs. Below: Viscek fractal constructed out of crosses.

fractal *subterms* in addition to the fractal term of F (see Eq. (1.1))

$$\begin{aligned} F(\mathcal{F} \cap W) &= F^{(0)} x^{d_0} \\ U(\mathcal{F} \cap W) &= U^{(0)} x^{d_0} + U^{(1)} x^{d_1} \\ \chi(\mathcal{F} \cap W) &= \chi^{(0)} x^{d_0} + \chi^{(1)} x^{d_1} + \chi^{(2)} x^{d_2}. \end{aligned} \tag{1.2}$$

The first exponent d_0 is the conventional fractal dimension. The exponents d_1 and d_2 are called *subdimensions.* $F^{(i)}$, $U^{(i)}$, and $\chi^{(i)}$ are amplitudes of the dimension d_i. If $i > 0$, the amplitudes are also called *subdimensional amplitudes.* The major aim of the thesis is to verify these subdimensions and the pyramidic subterm structure indicated in Eq. (1.2). The properties which are examined are the Minkowski scalars and 2-ranked Minkowski tensors. These Minkowski functionals are used because the Minkowski scalars describe the shape of objects and can be identified by F, U, and χ in two dimensions. The Minkowski tensors contain further information about the shape but also about the orientation of the objects. The Minkowski functionals are described in greater detail in chapter 2.1.

Another reason to investigate fractals and to look for these potential subdimensions is the deeper understanding of phase transitions. By determining additional dimensions and the corresponding amplitudes of fractals at phase transitions, the question arises what information is contained within these dimensions and amplitudes? Do they determine only the morphology of the structure? Or do the subterms contain any additional information about the phase transition like the transition threshold or the universal critical exponents [16, 17]? The critical exponents describe the behavior of certain quantities at a system parameter p close to the transition threshold p_c. The idea behind the critical exponents at a phase transition contained within subterms is interesting because fractals of critical systems with the same dimension and symmetry of the order parameter have the same critical exponents. If the subterms are stated by these exponents, two fractals emerging at phase transitions with equal critical exponents should have equal subdimensions and subdimensional amplitudes.

This thesis is structured in the following way. First, the Minkowski functionals and the fractal dimension are defined and explained in greater detail in chapter 2. In the same chapter also the simulation, the computational calculation techniques, and the analysis process are introduced. In general, fractals can be assigned into three types of fractals. The first fractal type is investigated in chapter 3. The fractals are deterministic fractals often called iterated fractals. The shape of these fractals is fixed. Consequently, two representatives of an iterated fractal are entirely identical. The two iterated fractals in this thesis are the two dimensional

Sierpiński carpet and the three dimensional Menger's sponge. In this chapter the existence of the subterms is proven. In chapter 4 the second type of fractals, the random iterated fractals, are considered namely the Mandelbrot percolation clusters and the generalized random carpets. The construction algorithms of these fractals are similar to the algorithms of the iterated fractals. However, random iterated fractals have random features, in other words these are stochastic geometries. Two representatives of a random iterated fractal are not necessarily identical. To reveal the information behind the subdimensions and subdimensional amplitudes in the following chapter 5, the fractal geometry is generalized. Additionally the scaling behavior of the fractals at the boundary of the observation window is examined. In the last chapter 6 two random fractals are considered; the diffusion limited aggregation cluster and the percolation cluster. The random fractals are the last type of fractals which often occur in nature. The shapes of two representatives of a random fractal are certainly different but have equal statistical properties.

2. Theoretical and Computational Background

2.1. Minkowski Functionals

Before introducing the fractals which are investigated, it is necessary to choose a convenient method to analyze the morphology and shape of fractals in this thesis, as for other structures occurring in physical processes [18, 19]. It has been shown that *scalar Minkowski functionals*, also called intrinsic volumes, are a suitable tool describing the shape of a structure [20]. However, the scalar Minkowski functionals are insufficient for analyzing anisotropy. A method to characterize the orientation and anisotropy is needed. Common methods are, for example, basing on Fourier transforms [21] or correlation functions [22]. The disadvantage of Fourier transforms ,however, are the effects due to a finite observation window which makes this attempt to characterize anisotropy impractical. Here the *tensorial Minkowski functionals* which generalize the Minkowski scalars are used. One has to start with the definition of the scalar Minkowski functionals to define these tensors. There are three common ways of defining the Minkowski scalars. The first way is to define them by using the Euler characteristic [23]. For the second way one observes the parallel body of the structure and uses fundamental measure theory. The Minkowski functionals are defined as weights of the volume of the parallel body due to Steiner's formula [24]. Although this definition is more fundamental, a definition based on curvature-weighted integrals of position or surface normal vectors over the structures has been established in physics [25, 26]. The third way is used in this thesis.

We consider objects in two and three dimensions. The scalars in two dimensions are given by [25]

$$W_0 := \int_K \mathrm{d}^2 r, \qquad W_1 := \frac{1}{2}\int_{\partial K} \mathrm{d}r, \qquad W_2 := \frac{1}{2}\int_{\partial K} \kappa \mathrm{d}r. \tag{2.1}$$

K is a convex body with a smooth boundary contour ∂K in 2D Euclidean space $\mathbb{E}^2$ and κ is the local curvature of the contour ∂K. W_0 is the volume of the body, W_1 is proportional to the boundary length, and W_2 describes the Euler characteristic.

In three dimensions the scalars are given by [26]

$$W_0 := \int_K \mathrm{d}^3 r, \qquad W_1 := \frac{1}{3}\int_{\partial K} \mathrm{d}^2 r, \qquad W_2 := \frac{1}{3}\int_{\partial K} G_2 \mathrm{d}^2 r, \\ W_3 := \frac{1}{3}\int_{\partial K} G_3 \mathrm{d}^2 r. \tag{2.2}$$

K is a compact body with a smooth bounding surface ∂K in 3D Euclidean space $\mathbb{E}^3$, $G_2 = \frac{\kappa_1+\kappa_2}{2}$ is the mean curvature on ∂K, and $G_3 = \kappa_1 \cdot \kappa_2$ is the point wise Gaussian curvature. This can be extended to higher dimensions where the number of scalar intrinsic volumes in n dimensions is $n+1$. By using tensor products of the position vector $\vec{r}$ and the normal vector $\vec{n}$ on the boundary with $(\vec{a}\otimes\vec{b})_{ij} = \frac{a_i b_j + a_j b_i}{2}$ the Minkowski scalars can be generalized to vectors and tensors in the following way [25]

$$W_0^{a,b} := \int_K \vec{r}^a \otimes \vec{n}^b \mathrm{d}^2 r, \quad W_1^{a,b} := \frac{1}{2}\int_{\partial K} \vec{r}^a \otimes \vec{n}^b \mathrm{d}r, \quad W_2^{a,b} := \frac{1}{2}\int_{\partial K} \kappa\, \vec{r}^a \otimes \vec{n}^b \mathrm{d}r \tag{2.3}$$

in two dimensions and [26]

$$W_0^{a,b} := \int_K \vec{r}^a \otimes \vec{n}^b \mathrm{d}^3 r, \quad W_1^{a,b} := \frac{1}{3}\int_{\partial K} \vec{r}^a \otimes \vec{n}^b \mathrm{d}^2 r, \quad W_2^{a,b} := \frac{1}{3}\int_{\partial K} G_2\, \vec{r}^a \otimes \vec{n}^b \mathrm{d}^2 r \\ W_3^{a,b} := \frac{1}{3}\int_{\partial K} G_3\, \vec{r}^a \otimes \vec{n}^b \mathrm{d}^2 r \tag{2.4}$$

in three dimensions. An advantage of the Minkowski functionals is the robustness against small levels of noise where small irregularities are of no major consequences. The expression $\vec{r}^a \otimes \vec{n}^b$ is in terms of the tensor product

$$\vec{r}^a \otimes \vec{n}^b = \underbrace{\vec{r} \otimes \cdots \otimes \vec{r}}_{a} \otimes \underbrace{\vec{n} \otimes \cdots \otimes \vec{n}}_{b}. \tag{2.5}$$

Already the rank-2 tensors, namely all tensors with $a + b = 2$, give sufficient information to characterize shape, anisotropy, and orientation in many areas of studies where morphology is necessary. Thus only rank-2 Minkowski tensors are considered.

For a better understanding of the Minkowski tensors, some of their properties are examined. The behavior under translation and rotation of K of the tensorial Minkowski functionals is

$$W_\nu^{a,b}(K \uplus \vec{t}) = \sum_{i=0}^{a} \binom{a}{i} \vec{t}^i \otimes W_\nu^{a-i,b}(K) \tag{2.6}$$

and

$$W_\nu^{a,b}(\hat{O}K) = \hat{O}W_\nu^{a,b}(K) \tag{2.7}$$

where $K \uplus \vec{t}$ is a translation of K by $\vec{t}$ and $\hat{O}$ is a rotation. Being motion covariant and in general not motion invariant, the Minkowski tensors depend on the origin of the coordinate system. $W_\nu^{0,b}$ is translation invariant fulfilling the equation $W_\nu^{0,b}(K \uplus \vec{t}) = W_\nu^{0,b}(K)$ out of Eq. (2.6). Due to the envelope theorem of Müller $W_\nu^{1,1}$ are also translation invariant [27]. The other tensors depend on the origin.

Another property used in this thesis is the additivity for finite unions of convex bodies

$$W_\nu^{a,b}(K \cup K') = W_\nu^{a,b}(K) + W_\nu^{a,b}(K') - W_\nu^{a,b}(K \cap K'), \tag{2.8}$$

such that the bodies do not have smooth boundaries necessarily. As a consequence, bodies do not have to be convex. All concave body which are discussed in this thesis can be seen as a finite union of convex bodies. Scaling the body K by a factor $\lambda \geq 0$, the tensors behave as

$$W_\nu^{a,b}(\lambda K) = \lambda^{n+a-\nu} W_\nu^{a,b}(K). \tag{2.9}$$

It is not necessary to observe all rank two Minkowski tensors as some linear dependencies exist. The equation

$$E_n W_\nu = \nu W_\nu^{0,2} + (n-\nu) W_{\nu+1}^{1,1} \tag{2.10}$$

shows their dependencies [28]. Additionally the tensors $W_0^{a,b}$ with $b \neq 0$ are not defined because the normal vectors are not defined as well when integrating over the interior but only its contour. A basis of rank-2 tensorial Minkowski functionals in two and three dimensions is listed in Table 2.1.

One has to considered whether the Minkowski functionals are complete in terms of shape and anisotropy description. Alesker's theorem states for rank-2 tensors that any isometry covariant, additive continuous functional ϕ on general convex bodies in $\mathbb{E}^n$, taking values in the space of symmetric tensors of rank two over $\mathbb{E}^n$, is a linear combination of the basic tensor valuations [29]. That is

$$\phi(K) = \sum_{\nu}^{n} (\phi_\nu^{0,0} W_\nu(K) E_n + \sum_{a=0}^{2} \phi_\nu^{a,2-a} W_\nu^{a,2-a}(K)). \tag{2.11}$$

with $\phi_\nu^{a,b} \in \mathbb{R}$ being coefficients that are independent of the convex body for all a, b, and ν.

Homogeneity	rank-2 Minkowski tensors 2D	rank-2 Minkowski tensors 3D
λ^5	–	$W_0^{2,0}$
λ^4	$W_0^{2,0}$	$W_1^{2,0}$
λ^3	$W_1^{2,0}$	$W_2^{2,0}$
	–	$W_0 E_3$
λ^2	$W_2^{2,0}$	$W_3^{2,0}$
	$W_0 E_2$	$W_1^{0,2}$
	–	$W_1 E_3$
λ	$W_2^{1,1}$	$W_2^{0,2}$
	$W_1 E_2$	$W_2 E_3$
λ^0	$W_2 E_2$	$W_3 E_3$

Table 2.1.: A set of linearly independent Minkowski tensors is given which describe an object completely due to Eq. (2.11). The homogeneity shows the behavior under scaling, see Eq. (2.9).

2.2. Fractal Dimension

After sorting out the mathematical tools, the connection between the Minkowski functionals and fractal geometry has to be addressed. Therefore, the *fractal dimension* d_f is defined [4]. To describe the notion of dimension for arbitrary sets, one needs the s-dimensional Hausdorff measure $\mathcal{H}^s(\mathcal{F}) = \lim_{\delta \to 0} \mathcal{H}^s_\delta(\mathcal{F})$ where $\mathcal{F} \subset \mathbb{R}^n$ is the fractal set. $\mathcal{H}^s_\delta(\mathcal{F})$ is defined as

$$\mathcal{H}^s_\delta(\mathcal{F}) = \inf\{\sum_{i=0}^{\infty} (\mathrm{diam}(U_i))^s : \mathcal{F} \subseteq \bigcup_{i=0}^{\infty} U_i, \mathrm{diam}(U_i) < \delta\}. \tag{2.12}$$

Here U_i are countable covers of $\mathcal{F}$ satisfying $\mathrm{diam}(U_i) < \delta$. $\mathrm{diam}(U)$ is defined as

$$\mathrm{diam}(U) = \inf\{r : r = |x_1 - x_2|, x_1\, x_2 \in U\} \tag{2.13}$$

and can be interpreted as a diameter of the set U. The dimension is then defined as the value of s at which $\mathcal{H}^s(\mathcal{F})$ changes from 0 to ∞ (see Fig. 2.1)

$$\dim_H(\mathcal{F}) = \inf\{s : \mathcal{H}^s(\mathcal{F}) = 0\} = \sup\{s : \mathcal{H}^s(\mathcal{F}) = \infty\}. \tag{2.14}$$

This definition of dimension known as the *Hausdorff-Besicovitch-dimension* has the disadvantage that it is difficult to calculate for many structures. Here we use another definition which is based on the same idea, namely the *similarity dimen-*

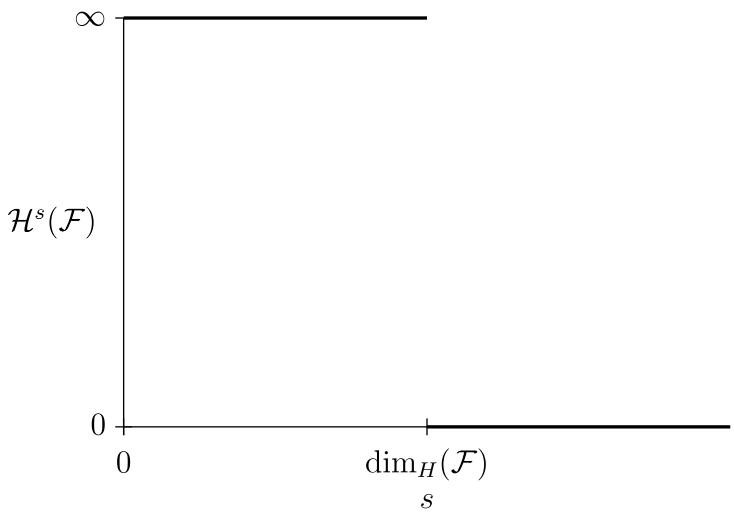

Figure 2.1.: The Hausdorff measure changes from ∞ to 0 at $\dim_H(\mathcal{F})$ as described in Eq. (2.14).

sion. The similarity dimension is easier to calculate for the fractals used in the following chapters and is equal to the Hausdorff-Besicovitch-dimension. However, it can not be calculated for all fractals. Instead of covers one calculates the volume and thus $W_0(\delta)$ of the set, measuring at a scale of δ. Irregularities smaller than δ are not taken into account. If $W_0(\delta, \mathcal{F}) = c \cdot \delta^{-s}$, s can be seen as a dimension and c as a s-dimensional amplitude.

Another dependency than δ is the size of an observation window. In contrast to neglect irregularities smaller than δ, they are not disregarded and the object is analyzed within an observation window instead. An advantage in this case is that one does not need the whole object to analyze it because often it is sufficient only to consider a part of the fractal within the specific window. By increasing the side length x of the window and hence examining more of the fractal, the approach for self-similar objects is equivalent to decreasing δ. For the dependency of x one has to replace $\delta = \alpha \cdot x^{-1}$. Therefore, s can be calculated in the following way

$$s = \lim_{\delta \to 0} -\frac{\ln W_0(\delta, \mathcal{F})}{\ln \delta} = \lim_{x \to \infty} \frac{\ln W_0(x, \mathcal{F})}{\ln x}. \tag{2.15}$$

This dimension is not defined for all sets as some fractals do not follow a power law. However, the set of fractals considered here do follow a power law. s is called the fractal dimension of the set $\mathcal{F}$ and is symbolized by d_f. However, also other Minkowski functionals are used in this thesis. If W_ν is not only defined by the

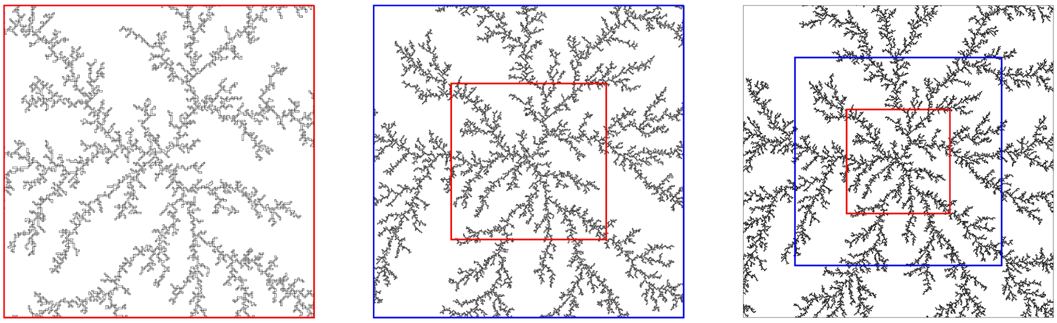

Figure 2.2.: A DLA cluster within a observation window of length 200, 400 and 600 respectively, from left to right is shown.

fractal term as it is assumed in Eq. (1.2) but also by an additional subterm, W_ν would be

$$W_\nu(x, \mathcal{F}) = c_0 \cdot x^{d_f} + c_1 \cdot x^{d_1} \tag{2.16}$$

The additional dimension d_1 is then called subdimension. The amplitude is called subdimensional amplitude c_1. This can be extended to an arbitrary number of i subterms. The dimension d_i is the i-th subdimension and the amplitude c_i is the i-th subdimensional amplitude. If the fractal term is the dominant one, d_i is smaller than d_f

$$\Delta_i d = d_i - d_f \leq 0. \tag{2.17}$$

2.3. Analysis Technique

In the course of this thesis many fractals are investigated where it is possible to determine the Minkowski functionals and fractal dimensions analytically (see chapter 3 and chapter 4). However, the Minkowski functionals of the fractals are also calculated numerically. Firstly, this checks the analytical results and secondly, for some of the structures the Minkowski functionals can only be calculated this way (see chapter 6). Thus, the software packages which calculates the functionals is briefly discussed.

2.3.1. Software

The software package for analyzing two dimensional structures is called *Papaya* [25]. It calculates the Minkowski functionals from triangulated, pixelated, or polygonized data. Papaya is able to calculate all three scalars, the vectors, and the rank-2 tensors $W_0^{0,2}$, $W_1^{0,2}$, $W_1^{2,0}$, $W_2^{1,1}$ and $W_2^{2,0}$. Comparing them to Table 2.1, all necessary Minkowski functionals up to the rank-2 tensors are implemented.

Papaya verson 1.5 is used.

The software *Karambola* and *Bilimbi* are used for calculating Minkowski functionals of 3-dimensional fractals. Both are included in the Karambola software package version 1.5 [26]. Karambola uses polygonized data as well. All necessary Minkowski functionals listed in Table 2.1 can be calculated. However, Karambola is not applicable for all of the fractal used in the following chapters. Thus, Bilimbi has to be used. Bilimbi calculates the functionals from voxelized data by using the marching cubes algorithm. It computes the scalars W_0, W_1, and W_3, the vector $W_0^{1,0}$, and the rank-2 tensors $W_0^{2,0}$, $W_1^{0,2}$, and $W_2^{0,2}$. Consequently, not all shape and anisotropy information can be obtained.

2.3.2. Sandbox Method

Until now it is not explained how the fractals and potential subdimensions are determined by Minkowski functionals which can not be calculated analytically. The Minkowski functionals are not calculated for the whole fractal but only parts of it. The object is considered within a quadratic and cubic observation window with length x, respectively. The center of the observation window is the origin of the fractal as well. The functionals are calculated only within the observation window. One starts with a small observation window and increases the length x by a certain step size Δx (see Fig. 2.2) until the window contains the whole fractal. If the data obtained for W_0 follows a power law, one can obtain the fractal dimension directly from the slope δ_f of the graph: $d_f = \delta_f$. This method is called Sandbox method or more precisely the Minkowski density method [30].

The Sandbox method has to be modified to calculate the subdimensions . One proceeds from Eq. (2.16) and uses a Minkowski tensor $W_\nu^{a,b}$ except W_0. Consequently, to cancel the dominant fractal term and to calculate the subterm exponents, $W_\nu^{a,b}$ is first divided by W_0. The tensors $W_\nu^{2,0}$ are also divided by x^2. This is caused by the integration over r^2 in Eq. (2.3) and Eq. (2.4). Because the fractal dimension is bigger than all the subdimensions, the second term exponent becomes negative with $\Delta_i d = d_i - d_f$. The graph of the modified data converges towards the ratio between the amplitude of the fractal term of W_0 c_f and the amplitude of the fractal term of $W_\nu^{a,b}$ c_0. Finally, this value $c = \frac{c_0}{c_f}$ is subtracted from $\frac{W_\nu^{a,b}}{W_0}$ and $\frac{W_\nu^{a,b}}{x^2 \cdot W_0}$, respectively. The second dominant term of the power law becomes dominant. By plotting $\frac{W_\nu^{a,b}}{W_0} - c$ and $\frac{W_\nu^{a,b}}{x^2 \cdot W_0} - c$, respectively, double logarithmically, the slope δ_1 of the data is equal to the difference between the first subdimension d_1 and the fractal dimension: $\delta_1 = \Delta_1 d$. To avoid errors occurring from potential further subterms, the slope is calculated at the highest possible x.

3. Iterated Fractals

To prove the existence of subdimensions and to get an idea about them and the simulation/analysis technique, the first fractals are considered which are the easiest type of fractals to determine: *deterministic, iterated fractals*. An iterated fractal is an object constructed from a starting configuration called *initiator* and a set of N generating function $f_i : X \to X \ \forall i \in \{1, \dots, N\}$ each mapping a complete metric space X to itself [31]. The set is called the generator or *iterated function system* (IFS). For every remapping of the set by the IFS, the structure gradually forms a fractal. The number of mappings is called the iterated step. This construction of fractals allows to generate complex structures with a few iterated steps. Moreover, the final objects can be handled analytically. The fractals which turn out to be qualified for our calculation method are one of the Sierpiński fractals, introduced by Wacław Sierpiński in 1916, in two dimensions and the Menger's sponge in three dimensions. These fractals are suitable because their mapping functions are simple and straightforward to implement.

3.1. Construction of Iterated Fractals

Before these examples of iterated fractals are investigated, the construction algorithm employed in this thesis is shown. It is important to mention that the method used here is slightly different from the common way of constructing an iterated fractal. The common and mathematical method which is based on fractal strings and sprays is explained later in chapter 5.1.3.

Let the initiator $I \subset \mathbb{R}^d$ be a closed interval around the origin $0^d = (\overbrace{0\,0\,0\,\dots\,0}^{d})^\top \in I$. For the first iterated step a set of N functions $\tilde{\phi}_i : \mathbb{R}^d \to \mathbb{R}^d$ is defined which scales the interval I by the factor $s_i \geq 1$ $s_i \in \mathbb{R}$ and then translates it by the vector $t_i \in \mathbb{R}^d$

$$\begin{aligned} \tilde{\phi}_i(x) &= s_i \cdot x + t_i && \forall i \in \{1, \dots, N\} \\ \tilde{\phi}_i(I) \cap \phi_j(I) &= \emptyset && \forall i, j : i \neq j. \end{aligned} \tag{3.1}$$

Next to the set of these functions, there is also the function $\Psi_r : \mathbb{R}^d \to \mathbb{R}^d$ with $\Psi_r(x) = r \cdot x$. The factor r is defined as the smallest number of $\mathbb{R}$ for which the union of all $\tilde{\phi}_i(I)$ is barely a subset of the image of $\Psi_r(I)$

$$r := \inf\{s \in \mathbb{R}\colon \bigcup_{i=1}^{N} \tilde{\phi}_i(I) \subseteq \Psi_s(I)\}. \tag{3.2}$$

In the following r is called the *zoom factor* or *scaling factor* of the fractal F. Consequently, the functions of the n-th iterated step $\phi_i^{[n]}$ can be described by

$$\phi_i^{[n]}\colon I^{[n-1]} \to I^{[n]} \qquad \phi_i^{[n]}(x) = s_i \cdot x + r^{n-1} t_i \tag{3.3}$$

where the sets $I^{[n]}$ are defined as

$$I^{[n]} := \Psi_r^{[n]} = \overbrace{\Psi_r \circ \cdots \circ \Psi_r}^{n}(I) \qquad I^{[0]}(I) = \mathrm{id}(I) = I. \tag{3.4}$$

One gets for every iterated step an iterated function system

$$\mathrm{IFS}^{[n]} := \{\phi_i^{[n]}\colon i \in \{1, \dots, N\}\}. \tag{3.5}$$

The set F_n after n iterated steps is defined as

$$\begin{gathered} F_n := \bigcup_{i=1}^{N} \Phi_i^{[n]}(I) \\ \Phi_i^{[n]}(I) := \phi_i^{[n]} \left(\bigcup_{i=1}^{N} \Phi_i^{[n-1]}(I) \right) \qquad \Phi_i^{[0]}(I) := \mathrm{id}(I). \end{gathered} \tag{3.6}$$

The actual fractal set F is the limit of Eq. (3.6)

$$F = F_\infty = \lim_{n\to\infty} \bigcup_{i=1}^{N} \Phi_i^{[n]}(I). \tag{3.7}$$

3.2. The Sierpiński Carpet

One of the most famous iterated fractals, the *Sierpiński carpet* [32], shown in Fig. 3.1 is considered. The initiator of this fractal is the unit interval around the origin $[-0.5, 0.5]^2 \subset \mathbb{R}^2$ which forms a square shaped motif. In the first step the interval is mapped by eight functions $\phi_i(x) = x + t_i$ with $s_i = 1$. t_i are the eight different translation vectors with $t_i = (a_i, b_i)^\top$ $a_i, b_i \in \{-1, 0, 1\}$. The case $a_i = b_i = 0$ does not occur. Consequently, the scaling factor of the Sierpiński carpet is $r = 3$. The elements of $\mathrm{IFS}^{[n]}$ for the n-th iterated step are in agreement

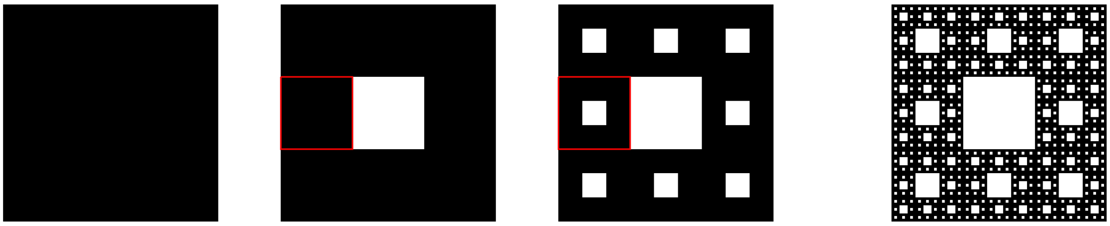

Figure 3.1.: Sierpiński carpet in the zeroth, first, second, and fourth iterated step, from left to right.

with Eq. (3.3)

$$\phi_i^{[n]} \colon [-3^n \cdot 0.5, 3^n \cdot 0.5]^2 \to [-3^{n-1} \cdot 0.5, 3^{n-1} \cdot 0.5]^2 \qquad \phi_i^{[n]}(x) = x + 3^{n-1} t_i. \quad (3.8)$$

For the iterated fractals the Sandbox method has to be slightly varied. Here the reason of constructing the fractals as explained in the last section becomes obvious. Instead of building the whole fractal and observing parts of it within different observation window sizes, it is enough to build the structures of the first iterated steps and to observe simply the progression of the Minkowski functionals on the iterated step. Conveniently the algorithm is conceptualized that every structure of a step is a part of the structure of the next step without rescaling. Additionally, the Minkowski functionals can be calculated for all steps with this technique. We know that the fractals become larger for every step n thus the observation window also becomes larger. Strictly speaking, x increases by the factor 3 for every iterated step. Thus one has an observation window length of $x = 3^n$ after n steps. The slopes of the obtained graph as one proceeds as in chapter 2.3.2 are consequently not the actual dimensions since this zooming factor 3 has to be considered. All slopes have to be divided by $\ln 3$ to get the actual dimension. Furthermore, the functionals are not plotted double logarithmic but only logarithmic on the y-axis because through the relation between x and n the logarithm of x is already contained. However, the amplitudes of the terms are not effected on this change, such that one does not have to modify them.

First of all, the Minkowski functionals are calculated numerically for the first steps with Papaya. The origin of the coordinate system is set to the center of the object for every step n. The contours are parallel to the x- and y-axis, such that the tensors only have non-zero entries on their main diagonal. These are all equal because the object is always point-symmetric for every step n. Thus, it is enough to consider the traces. The fractal dimension is calculated from W_0 starting with a square with a surface of 1. The slope of the graph of W_0 plotted logarithmically in Fig. 3.2 is $\delta_0 = \ln 8$. Taking the zoom factor into account, the fractal dimension

$d_f = d_0 = \frac{\ln 8}{\ln 3}$ is obtained. This is exactly the literature value of the fractal dimension of the Sierpiński carpet [33]. By plotting the functionals logarithmically as well, one determines that W_1 and W_2 both have similar slopes as W_0. By comparing them for the very first steps, like in Fig. 3.2, it becomes apparent that W_1 initially approaches a straight line with the fractal dimension as its slope. This gives evidence that the contour length follows a power law where the dominant term has the fractal dimension as its exponent and at least one subdominant term. The tensors $W_\nu^{2,0}$, however, have a dominant term with the exponent $d_f + 2$. This difference of 2 is due to the integration over r^2 in Eq. (2.3).

With this first evidence of existence of the subdimensions the functionals of the first iterated steps are calculated analytically. The progressions of the functionals are calculated out of these results (see Appendix A). The Minkowski scalars are

$$\begin{aligned} W_0(n) &= 8^n, \\ W_1(n) &= \frac{2}{5}8^n + \frac{8}{5}3^n, \text{ and} \\ W_2(n) &= -\frac{1}{7}\pi 8^n + \frac{8}{7}\pi. \end{aligned} \tag{3.9}$$

The traces of the Minkowski tensors are

$$\begin{aligned} \mathrm{Tr}[W_0^{2,0}](n) &= \frac{3}{16}72^n - \frac{1}{48}8^n, \\ \mathrm{Tr}[W_1^{0,2}](n) &= \frac{2}{5}8^n + \frac{8}{5}3^n, \\ \mathrm{Tr}[W_1^{2,0}](n) &= \frac{3}{40}72^n + \frac{128}{285}27^n + \frac{65}{456}8^n, \text{ and} \\ \mathrm{Tr}[W_2^{2,0}](n) &= -\frac{3}{112}\pi 72^n + \frac{12}{7}\pi 9^n - \frac{19}{16}\pi 8^n. \end{aligned} \tag{3.10}$$

There are indeed subdimensions observable. W_1 shows that next to the fractal term there is also a surface subterm with an exponent of $d_s = d_1 = 1$. The difference $\Delta_1 d = \log_3 \frac{3}{8} \approx -0.893$ slightly varies from the intuitive guess -1. This guess seemed logical because W_0 is dealing with the area of the structure whereas W_1 represents the contour length. Also the curvature shows a subdimensional term. The subdimension calculated here is $d_c = d_2 = 0$. Consequently, the surface term does not appear in the scaling of W_2, at least in case of the Sierpiński carpet. It turns out that the additional term is a constant instead.

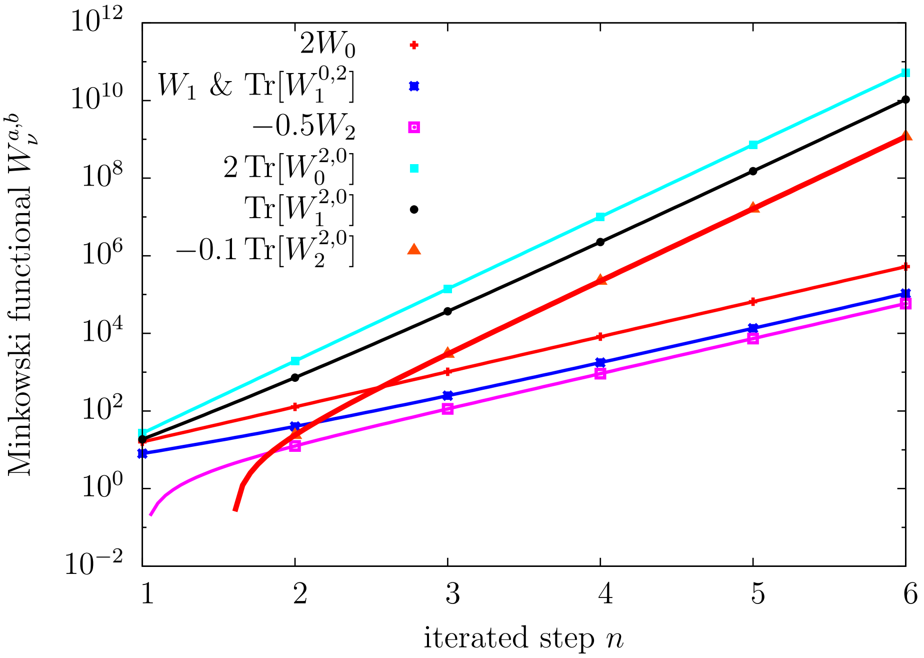

Figure 3.2.: The progressions of the Minkowski scalars and rank-2 tensors of the Sierpiński carpet for the first 5 iterated steps are depicted. The functions in Eq. (3.9) and in Eq. (3.10) are plotted as well. In the very first steps W_2 and $W_2^{2,0}$ are zero and positive, respectively.

ν	0	1	2	3
d_ν	$\log_3 8$	1	0	$d_0 - 2$
$w_{0;\nu}$	1	–	–	–
$w_{1;\nu}$	$\frac{2}{5}$	$\frac{8}{5}$	–	–
$w_{2;\nu}$	$-\frac{1}{7}\pi$	0	$\frac{8}{7}\pi$	–
$w_{0;\nu}^{2,0}$	$\frac{3}{16}$	–	–	$-\frac{1}{48}$
$w_{1;\nu}^{0,2}$	$\frac{2}{5}$	$\frac{8}{5}$	–	–
$w_{1;\nu}^{2,0}$	$\frac{3}{40}$	$\frac{128}{285}$	–	$\frac{65}{456}$
$w_{2;\nu}^{2,0}$	$-\frac{3}{112}\pi$	0	$\frac{12}{7}\pi$	$-\frac{19}{16}\pi$

Table 3.1.: This table determines the Minkowski fuctionals of the Sierpiński carpet up to the rank-2 tensors (see Eq. (3.11)). The fractal dimension, the subdimensions, and the corresponding fractal amplitudes are listed. The values are obtained from Eq. (3.9) and Eq. (3.10).

The tensor $W_1^{0,2}$ gives no further information because the structure is symmetric and the contours are parallel to one of the axis. Therefore, it is equivalent to W_1. However, $W_0^{2,0}$ has next to the expected dominant term with the exponent $d_f + 2$ another term which is basically the fractal term again. By considering the addition +2 to the dimension for the tensors $W_\nu^{2,0}$ due to Eq. (2.3), the subdimension is $d_f - 2$. Also in the definition of the tensors $W_1^{2,0}$ and $W_2^{2,0}$ these two terms occur. The third subdimension of $W_1^{2,0}$ and $W_2^{2,0}$ is basically the subdimension of the scalar they are based on. The only modification is that they are increased by 2 as it happens for the dominant term. Consequently, these functionals have a first term with $d_f + 2$, a second term with $d_1 + 2$ and $d_2 + 2$, respectively, and the initial fractal dimension $d_3 + 2 = d_f$.

With this results one can make the first assumption

$$\begin{aligned}
W_0(x) &= w_{0;0}x^{d_f} \\
W_1(x) &= w_{1;0}x^{d_f} + w_{1;1}x^{d_1} \\
W_2(x) &= w_{2;0}x^{d_f} + w_{2;1}x^{d_1} + w_{2;2}x^{d_2} \\
\mathrm{Tr}[W_0^{2,0}](x) &= w_{0;0}^{2,0}x^{d_f+2} + w_{0;3}^{2,0}x^{d_3+2} \\
\mathrm{Tr}[W_1^{0,2}](x) &= w_{1;0}^{0,2}x^{d_f} + w_{1;1}^{0,2}x^{d_1} \\
\mathrm{Tr}[W_1^{2,0}](x) &= w_{1;0}^{2,0}x^{d_f+2} + w_{1;1}^{2,0}x^{d_1+2} + w_{1;3}^{2,0}x^{d_3+2} \\
\mathrm{Tr}[W_2^{2,0}](x) &= w_{2;0}^{2,0}x^{d_f+2} + w_{2;1}^{2,0}x^{d_1+2} + w_{2;2}^{2,0}x^{d_2+2} + w_{2;3}^{2,0}x^{d_3+2}.
\end{aligned} \tag{3.11}$$

$w_{\nu;i}^{a,b}$ are the corresponding amplitudes. To state the dimensions and amplitudes in a better way, they are outlined for the Sierpiński carpet in Table 3.1. In Fig. 3.2 the numerical and analytical results are compared. One can see that they agree within numerical errors.

In the next step one proceeds as given in chapter 2.3.2 to make the subdimensions visible and to test the Sandbox method. The only difference is using 3^{2n} instead of x^2 for the division of $W_\nu^{2,0}$. The constant c which has to be subtracted to obtain the subdimensions are the amplitudes $w_{\nu;0}^{a,b}$ of the first terms in Eq. 3.9 and Eq. 3.10. The resulting graphs of the functionals are plotted in Fig. 3.3. These plots and the determined slopes which are listed in Table 3.2 show that the second ranked terms are ascertained with this method as well. Nevertheless, this method indicates a few disadvantages. For functionals with more than two terms only the first two terms can be determined. Furthermore, the lower terms are causing an error in calculating the amplitudes and exponents of the more dominant terms because the window is rather small in the beginning of the construction. The effect is indeed small for this example (compare the calculated dimensions of W_1

and $W_1^{2,0}$ in Table 3.2), however, one should consider it especially if more than two subterms occur.

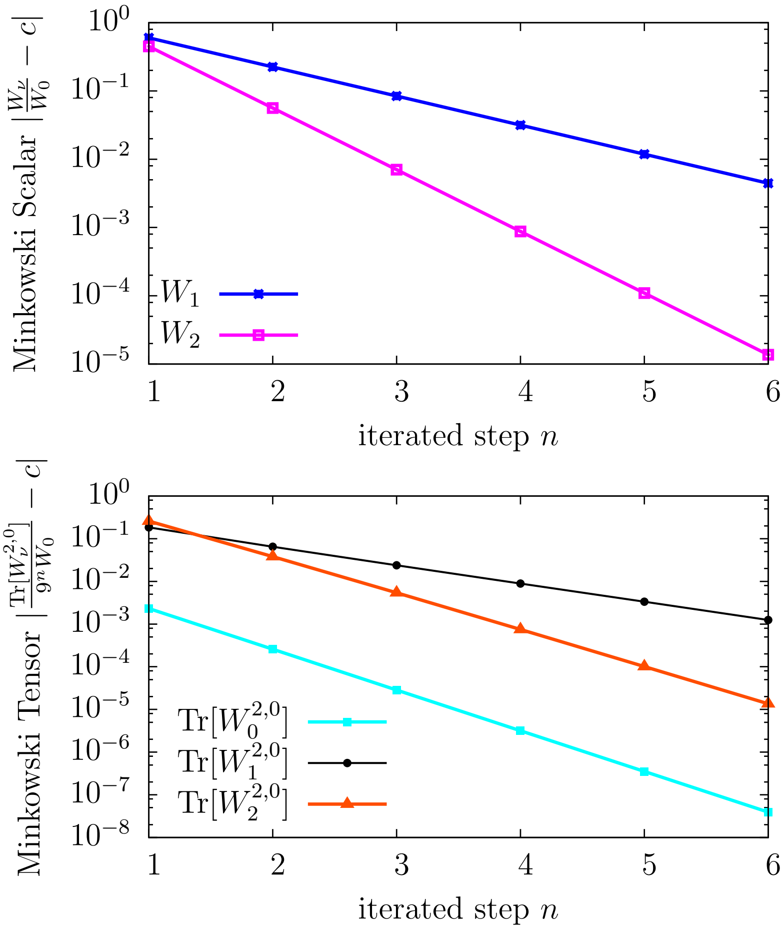

Figure 3.3.: The progressions of the subterms of the Minkowski functionals for the Sierpiński carpet are depicted using the Sandbox method. The subtracted constants are calculated in Eq. (3.9) and Eq.(3.10).

$W_\nu^{a,b}$	W_1	W_2	$\mathrm{Tr}[W_0^{2,0}]$	$\mathrm{Tr}[W_1^{2,0}]$	$\mathrm{Tr}[W_2^{2,0}]$
δ_1	ln(0.375)	ln(0.125)	ln(0.111)	ln(0.373)	ln(0.138)
$\Delta_1 d$	-0.893	-1.893	-2.001	-0.898	-1.803

Table 3.2.: The slopes δ_1 and the dimension difference $\Delta_1 d$ of the subdominant terms of $W_\nu^{a,b}$ are listed due to analyzing the Sierpiński carpet with the Sandbox method. The corresponding data is plotted in Fig. 3.3.

3.3. The Menger's Sponge

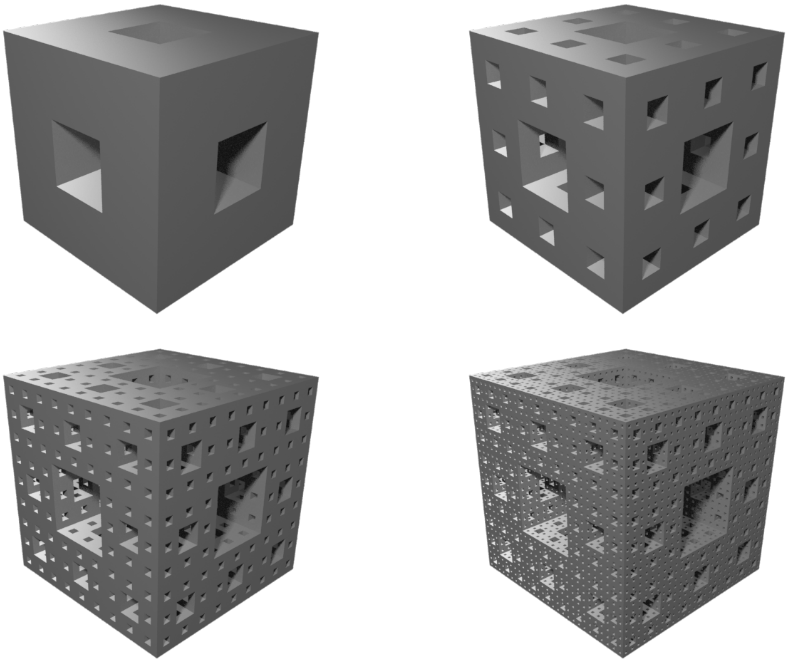

Figure 3.4.: The Menger's sponge in the first, second, third, and fourth iterated steps.

Now the three dimensional *Menger's sponge* is considered [34]. This object is the three dimensional analogue of the Sierpiński Carpet (Fig. 3.4). The initiator is the unit interval around the origin $[-0.5, 0.5]^3 \subset \mathbb{R}^3$ which forms a cubic shaped motif. In the first step the interval is mapped by 20 functions $\phi_i(x) = x + t_i$. t_i are the 20 different translation vector with $t_i = (a_i, b_i, c_i)^\top$ $a_i, b_i, c_i \in \{-1, 0, 1\}$ without the cases $x = y = 0$ $\forall x, y \in \{a_i, b_i, c_i\}\colon x \neq y$. The factor is $s_i = 1$ for all $i \in \{1, \dots, 20\}$. Consequently, the scaling factor of the Menger's sponge is the same as the scaling factor of the Sierpiński carpet $r = 3$. The elements of $\mathrm{IFS}^{[n]}$ for the n-th iterated step are

$$\phi_i^{[n]}\colon [-3^n \cdot 0.5, 3^n \cdot 0.5]^3 \to [-3^{n-1} \cdot 0.5, 3^{n-1} \cdot 0.5]^3 \qquad \phi_i^{[n]}(x) = x + 3^{n-1} t_i. \quad (3.12)$$

Now one can construct the structure F_n for every step n computationally and calculate the Minkowski funtionals.

Plotting the graphs of W_0 and the other scalars close together (see Fig. 3.5), one notices that they have similar slopes at high values of $n > 3$. The slope of W_0

reveals the fractal dimension $d_f = d_0 = \log_3 20$ which matches the literature value [1]. Only at the very beginning of W_1, W_2, and W_3 the slopes differ significantly. The other functionals show the same behavior except of $W_\nu^{2,0}$ for the very same reason as for the Sierpiński carpet (see Eq. (2.4)). This similarity between 2D and 3D supports the assumption that subdimensions are also observed in 3D.

At first, the functionals are calculated analytically (see Appendix B). The Minkowski scalars are thus given by

$$\begin{aligned}
W_0(n) &= 20^n, \\
W_1(n) &= \frac{2}{3}20^n + \frac{4}{3}8^n, \\
W_2(n) &= -\frac{1}{51}\pi 20^n + \frac{4}{15}\pi 8^n + \frac{64}{85}\pi 3^n, \text{ and} \\
W_3(n) &= -\frac{4}{19}\pi 20^n - \frac{8}{21}\pi 8^n + \frac{256}{133}\pi.
\end{aligned} \tag{3.13}$$

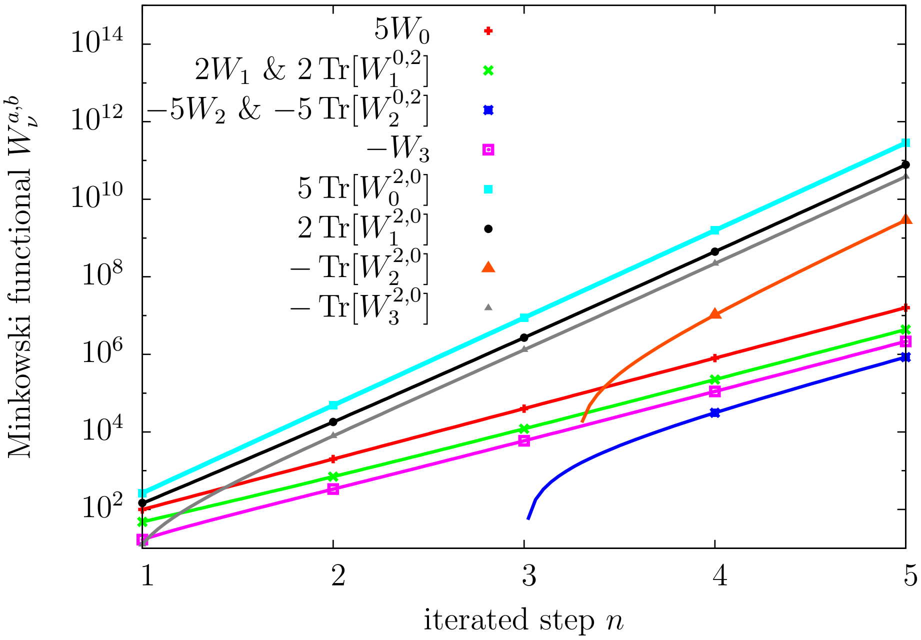

Figure 3.5.: The progressions of the Minkowski scalars and rank-2 tensors of the Menger's sponge for the first 5 iterated steps are shown. The functions in Eq. (3.13) and in Eq. (3.14) are plotted as well. In the very first steps W_2, $W_2^{0,2}$, and $W_2^{2,0}$ are positive.

ν	0	1	2	3	4	5
d_ν	$\log_3 20$	$\log_3 8$	1	0	$d_0 - 2$	$d_1 - 2$
$w_{0;\nu}$	1	–	–	–	–	–
$w_{1;\nu}$	$\frac{2}{3}$	$\frac{4}{3}$	–	–	–	–
$w_{2;\nu}$	$-\frac{1}{51}\pi$	$\frac{4}{15}\pi$	$\frac{64}{85}\pi$	–	–	–
$w_{3;\nu}$	$-\frac{4}{19}\pi$	$-\frac{8}{21}\pi$	0	$\frac{256}{133}\pi$	–	–
$w_{0;\nu}^{2,0}$	$\frac{3}{10}$	–	–	–	$-\frac{1}{20}$	–
$w_{1;\nu}^{0,2}$	$\frac{2}{3}$	$\frac{4}{3}$	–	–	–	–
$w_{1;\nu}^{2,0}$	$\frac{1}{5}$	$\frac{25}{52}$	–	–	$\frac{211}{1170}$	$-\frac{1}{36}$
$w_{2;\nu}^{0,2}$	$-\frac{1}{51}\pi$	$\frac{4}{15}\pi$	$\frac{64}{85}\pi$	–	–	–
$w_{2;\nu}^{2,0}$	$-\frac{1}{170}\pi$	$\frac{5}{52}\pi$	$\frac{3632}{6783}\pi$	–	$-\frac{2251}{16380}\pi$	$\frac{65}{684}\pi$
$w_{3;\nu}^{2,0}$	$-\frac{6}{95}\pi$	$-\frac{25}{182}\pi$	0	$\frac{5952}{1463}\pi$	$\frac{641}{2145}\pi$	$-\frac{19}{6}\pi$

Table 3.3.: This table determines the Minkowski fuctionals of the Menger's sponge up to the rank-2 tensors (see Eq. (3.15)). The fractal dimension, the subdimensions, and the corresponding fractal amplitudes are listed. The values are obtained from Eq. (3.13) and Eq. (3.14).

The Minkowski tensors are given by

$$\begin{aligned}
\mathrm{Tr}[W_0^{2,0}](n) &= \frac{3}{10}180^n - \frac{1}{20}20^n, \\
\mathrm{Tr}[W_1^{0,2}](n) &= \frac{2}{3}20^n + \frac{4}{3}8^n, \\
\mathrm{Tr}[W_1^{2,0}](n) &= \frac{1}{5}180^n + \frac{25}{52}72^n + \frac{211}{1170}20^n - \frac{1}{36}8^n, \\
\mathrm{Tr}[W_2^{0,2}](n) &= -\frac{1}{51}\pi 20^n + \frac{4}{15}\pi 8^n + \frac{64}{85}\pi 3^n, \\
\mathrm{Tr}[W_2^{2,0}](n) &= -\frac{1}{170}\pi 180^n + \frac{5}{52}\pi 72^n + \frac{3632}{6783}\pi 27^n - \frac{2251}{16380}\pi 20^n + \frac{65}{684}\pi 8^n, \text{ and} \\
\mathrm{Tr}[W_3^{2,0}](n) &= -\frac{6}{95}\pi 180^n - \frac{25}{182}\pi 72^n + \frac{641}{2145}\pi 20^n + \frac{5952}{1463}\pi 9^n - \frac{19}{6}\pi 8^n.
\end{aligned} \tag{3.14}$$

As in two dimensions there are indeed subterms observed in three dimensions. And in other ways a similar behavior as for the two dimensional Sierpiński carpet becomes apparent as well. W_1 shows the predicted surface term with $d_s = d_1 = \log_3 8$. And also W_2 and W_3 show the expected number of additional terms. Despite the Sierpiński carpet has not shown the surface term for W_2, both the mean and the Gaussian curvature scales with a surface and two different curvature terms

$d_c = d_2 = \log_3 3 = 1$ and $d_g = d_3 = \log_3 1 = 0$. Looking at the differences of the dimensions $\Delta_1 d = \log_3 \frac{2}{5} \neq -1$, $\Delta_2 d = \log_3 \frac{3}{20} \neq -2$ and $\Delta_3 d = \frac{1}{20} \neq -3$, the hypothesis $\Delta d = -1$ not to be true again. The tensors display the familiar behavior as well. The dimensions of the first terms are attributed to the dimensions of the Minkowski scalars: $d_0 + 2$, $d_1 + 2$, $d_2 + 2$ and $d_3 + 2$. Nevertheless, there are differences in the additional terms. For $W_\nu^{2,0}$ one gets also the initial fractal term d_f and a new term which has the dimension d_s. Thus we get not only one additional subdimension $d_4 = d_f - 2$, but also a second additional subdimension $d_5 = d_s - 2$. Consequently, Eq. (3.11) and Table 3.1 has to be generalized and extended in three dimensions. The assumption in three dimensions is

$$\begin{aligned}
W_0(x) &= w_{0;0} x^{d_f} \\
W_1(x) &= w_{1;0} x^{d_f} + w_{1;1} x^{d_1} \\
W_2(x) &= w_{2;0} x^{d_f} + w_{2;1} x^{d_1} + w_{2;2} x^{d_2} \\
W_3(x) &= w_{3;0} x^{d_f} + w_{3;1} x^{d_1} + w_{3;2} x^{d_2} + w_{3;3} x^{d_3} \\
\mathrm{Tr}[W_0^{2,0}](x) &= w_{0;0}^{2,0} x^{d_f+2} + w_{0;4}^{2,0} x^{d_4+2} \\
\mathrm{Tr}[W_1^{0,2}](x) &= w_{1;0}^{0,2} x^{d_f} + w_{1;1}^{0,2} x^{d_1} \\
\mathrm{Tr}[W_1^{2,0}](x) &= w_{1;0}^{2,0} x^{d_f+2} + w_{1;1}^{2,0} x^{d_1+2} + w_{1;4}^{2,0} x^{d_4+2} + w_{1;5}^{2,0} x^{d_5+2} \\
\mathrm{Tr}[W_2^{0,2}](x) &= w_{2;0}^{0,2} x^{d_f} + w_{2;1}^{0,2} x^{d_1} + w_{2;2}^{0,2} x^{d_2} \\
\mathrm{Tr}[W_2^{2,0}](x) &= w_{2;0}^{2,0} x^{d_f+2} + w_{2;1}^{2,0} x^{d_1+2} + w_{2;2}^{2,0} x^{d_2+2} + w_{2;4}^{2,0} x^{d_4+2} + w_{2;5}^{2,0} x^{d_5+2} \\
\mathrm{Tr}[W_3^{2,0}](x) &= w_{3;0}^{2,0} x^{d_f+2} + w_{3;1}^{2,0} x^{d_1+2} + w_{3;2}^{2,0} x^{d_2+2} + w_{3;3}^{2,0} x^{d_3+2} + w_{3;4}^{2,0} x^{d_4+2} + w_{3;5}^{2,0} x^{d_5+2} .
\end{aligned} \tag{3.15}$$

The extended Table 3.3 is shown using the example of the Menger's sponge.

The Sandbox method and Karambola are also tested in the three dimensional case. The constants which have to be subtracted to obtain the subdimensions are the amplitudes of the first terms in Eq. (3.13) and Eq. (3.14). The resulting graphs of the functionals are plotted in Fig. 3.6. The slopes are listed in Table 3.4. The just calculated amplitudes and dimensions match well with the numerical results. However, the mentioned disadvantage occurs here. The mean curvature and the gaussian subdimensions can not be calculated being the third term exponents of W_2 and W_3, respectively.

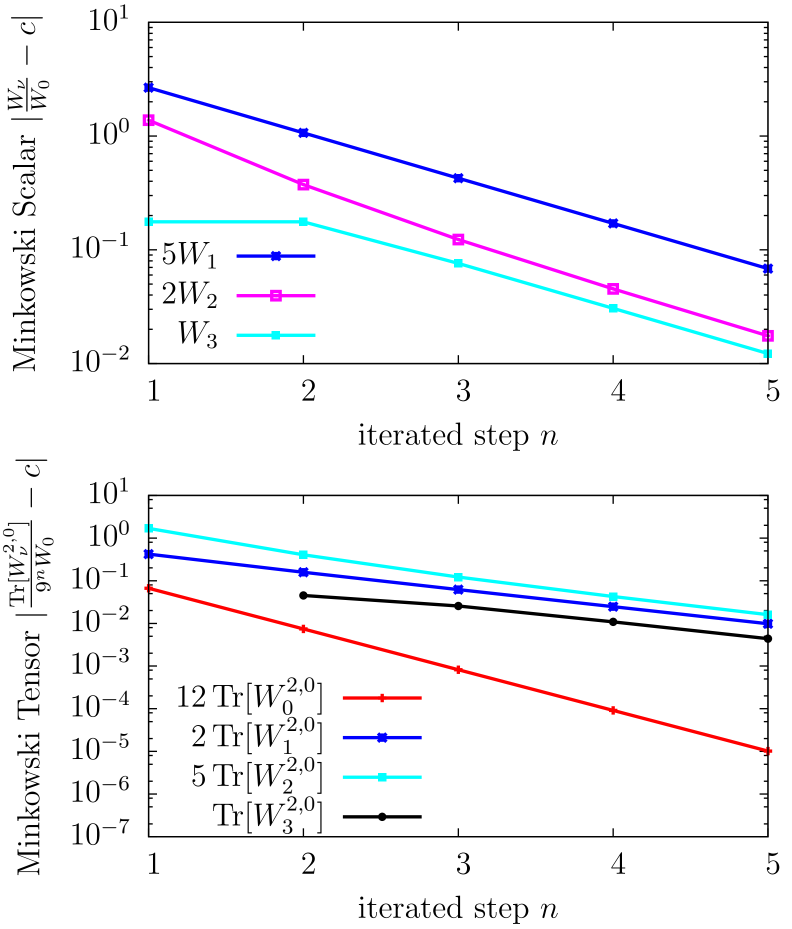

Figure 3.6.: The progressions of the subterms of the Minkowski functionals for the Menger's sponge are depicted, using the Sandbox method. The subtracted constants c are calculated in Eq. (3.13) and Eq. (3.14). $\frac{\mathrm{Tr}[W_3^{2,0}]}{9^n W_0} - c$ changes from positive values at $n = 1$ to negative values at $n = 2$. This is why it is not plotted at $n = 1$.

$W_\nu^{a,b}$	W_1	W_2	W_3	$\mathrm{Tr}[W_0^{2,0}]$	$\mathrm{Tr}[W_1^{2,0}]$	$\mathrm{Tr}[W_2^{2,0}]$	$\mathrm{Tr}[W_3^{2,0}]$
δ_1	ln(0.400)	ln(0.371)	ln(0.403)	ln(0.111)	ln(0.398)	ln(0.353)	ln(0.420)
$\Delta_1 d$	-0.834	-0.903	-0.827	-2.001	-0.839	-0.948	-0.790

Table 3.4.: The slopes δ_1 and the dimension difference $\Delta_1 d$ of the subdominant terms of $W_\nu^{a,b}$ are listed due to analyzing the Menger's sponge with the Sandbox method. The corresponding data is plotted in Fig. 3.6.

4. Random Iterated Fractals

The iterated fractals are a great field of fractals because all of their representatives have the advantage of being analytically calculable. Unfortunately the iterated fractals do not cover the whole field of fractal geometric structures and geometries. After the existence of the subdimensions are proven, one now can examine some more complex type of fractals. Therefore, the second type of fractals handled in this thesis are the *random iterated fractals*. As the name already reveals, the random iterated fractals are close to the iterated fractals, but have some random features. Those fractals can be seen as an intermediate fractal structure between fully deterministic and fully random fractal structures. Although the mean values of the Minkowski functionals for random fractals are investigated, they can be still determined analytically for the first iterated steps. Furthermore, it is easy to built a random iterated fractal out of an iterated fractal as one can see in the construction algorithm which is described in the following section.

4.1. Construction of Random Iterated Fractals

The construction algorithm is similar to the algorithm of iterated structures in chapter 3.1.

The initiator I is again an interval in $\mathbb{R}^d$ with the origin 0^d being an element of I. The definitions of ϕ_i, $\phi_i^{[n]}$, and r are the same as in Eq. (3.1), Eq. (3.2), and Eq. (3.3). The difference is that $\mathrm{IFS}^{[n]}$ does not necessarily contain all possible maps $\phi_i^{[n]}$. A random number $p_i^{[n]}$ between 0 and 1 is assigned to every function $\phi_i^{[n]}$. If $p_i^{[n]}$ is smaller than the probability p, the function $\phi_i^{[n]}$ is an element of $\mathrm{IFS}^{[n]}$. This holds for every iterated step and every $\phi_i^{[n]}$ independently from all other $\phi_i^{[n]}$ $i \neq j$ and all previous $\mathrm{IFS}^{[\tilde{n}]}$ $n > \tilde{n} > 0$. In other words, the probability $\mathbb{P}(\phi_i^{[n]})$ that $\phi_i^{[n]}$ maps the structure is $\mathbb{P}(\phi_i^{[n]}) = p \in [0,1]$ $\forall n, i$. For every step n there is a set M_n which determines all actual $\phi_i^{[n]}$ which are element of $\mathrm{IFS}^{[n]}$

$$M_n := \{i \in \{1, \dots, N\} \colon \phi_i^{[n]} \in \mathrm{IFS}^{[n]}\}. \tag{4.1}$$

Referring to Eq. (3.6), the structure after n iterated steps is

$$F_n = \bigcup_{i \in M_n} \Phi_i^{[n]}(I). \tag{4.2}$$

One has to take care that the image after the $(n-1)$-th step acts as the pre-image of the n-th step

$$\Phi_i^{[n]}(I) = \phi_i^{[n]} \left(\bigcup_{i \in M_{n-1}} \Phi_i^{[n-1]}(I) \right). \tag{4.3}$$

4.2. The Mandelbrot Percolation

The first example which can be counted among the random iterated fractals is the *Mandelbrot percolation cluster* (MPC), also known as fractal percolation [1]. The MPC is a special case of a random Cantor set. Mandelbrot came up with the idea to create this type of fractal in 1974. For example, it is used to model the distribution of galaxies or intermittency in turbulence [35]. Often Cantor sets are defined by substitutions [36]. The system within a square set is tessellated into subsquares and represented by tensors also called *symbols.* The entries of the tensors indicate whether a certain subsquare at a certain point is part of the whole structure or not. These entries of the symbols are called *words.*

First a set of all $r = 2^{m^2}$ possible $m \times m$ ($m \geq 2$) sized matrices $\{U_1, U_2, \ldots, U_r\}$ which entries are either 0 or 1 is defined to construct the Cantor set. σ is characterized as a substitution if it maps a word onto one of the symbols U_i. $\sigma(0) = 0_{m\times m}$ is the $m \times m$ matrix with all entries being 0. However, $\sigma(1)$ is U_i with the probability $p_i \in [0,1]$ and $\sum\limits_{i=1}^{r} p_i = 1$

$$\sigma(0) := 0_{m\times m}, \quad \sigma(1) := U_i \text{ with probability } p_i. \tag{4.4}$$

Now one can apply this substitution on an initial symbol. The initiator of the Cantor set is a square interval $C_0 = [-0.5, 0.5]^2 \subset \mathbb{R}^2$ and can be represented by a symbol which consists simply of the single word 1. For the first step one gets the matrix $\sigma(1)$. For the next step the substitution is applied on all words of $\sigma(1)$. This is done for all the next steps, such that in the n-th step the symbol is a $m^n \times m^n$ matrix $\sigma_{ij}^n(1)$. All the words at the entries $\sigma_{ij}^n(1)$ represent congruent,

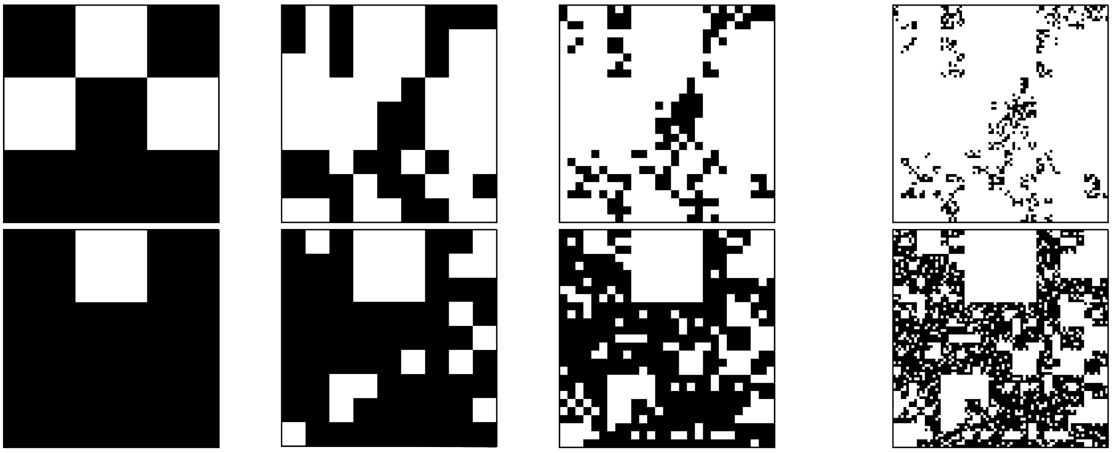

Figure 4.1.: Representative structures of the ${}_3$MPC with probability $p = 0.5$ (above) and $p = 0.8$ (below) in the first, second, third, and fourth iterated step – from left to right – are depicted.

not intersecting squares with volume 1

$$V_{ij}^n := [(i-1) - \frac{m^n}{2}, i - \frac{m^n}{2}] \times [(j-1) - \frac{m^n}{2}, j - \frac{m^n}{2}] \\ \forall i, j \in \{1, \ldots, m^n\}. \tag{4.5}$$

The Cantor set after the n-th step is then defined as

$$\mathrm{C}_n := \bigcup_{\substack{i,j \\ \sigma_{ij}^n = 1}} V_{ij}^n. \tag{4.6}$$

One can see that the natural number m states the square root of the number of squares which are maximally created out of one initial square. The further thesis just handles clusters with $m = 2$ and $m = 3$. If $p_i = p' \ \forall i$, C_n is called a ${}_n$MPC and the procedure can be simplified by setting every entry of $\sigma(1)$ individually to 1 with probability p or to 0 with probability $1 - p$. By repeating this infinitely, one gets the Mandelbrot percolation MPC. Some MPCs with different values of p are depicted in Fig 4.1.

4.2.1. The Random Carpet

By comparing the construction algorithm of the MPC with the algorithm of the random iterated fractals in chapter 4.1, the attentive reader notices that they do not match. There is also no other way of constructing the Mandelbrot percolations

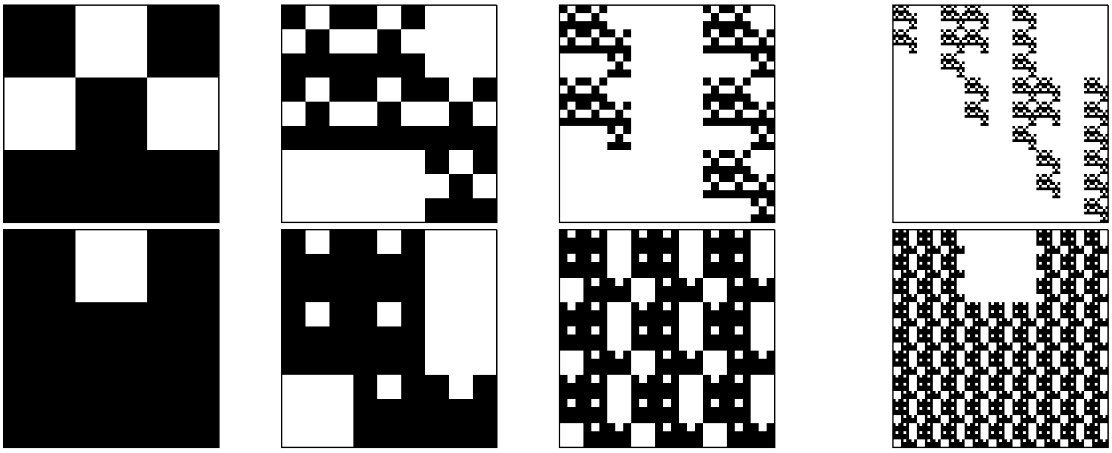

Figure 4.2.: Representative structures of the ${}_3$RC with probability $p = 0.5$ (above) and $p = 0.8$ (below) in the first, second, third, and fourth iterated step – from left to right – are depicted.

which is in better agreement with the random iterated fractal algorithm. However, the MPC is still called a random iterated fractal. A structure which morphology is statistically equal up to the rank-2 tensors can be built with the random iterated algorithm. In this thesis this structure is called *random carpet* (RC) referring to the Sierpiński carpet. It is defined in the following way.

As for MPC two specific RCs are covered. The initiator of the first RC is an interval [-0.5,0.5]$^2 \subset \mathbb{R}^2$. One has $N = 9$ maps $\phi_i(x) = x + s_i t_i$. These maps are the same maps as for the Sierpiński carpet with $s_i = 1$ and $t_i = (a_i, b_i)^\top$ $a_i, b_i \in \{-1, 0, 1\}$. The only difference is that the map with $a_i = b_i = 0$ is included within the IFS. The scaling factor of this RC is $r = 3$. In the following this random carpet cluster is called ${}_3$RC. The second RC is a smaller version of the first one. The initiator is again the interval [-0.5,0.5]$^2 \subset \mathbb{R}^2$. In this case only $N = 4$ functions $\tilde{\phi}_i(x) = x + \tilde{t}_i$ with $\tilde{s}_i = 1$ and $\tilde{t}_i = (\tilde{a}_i, \tilde{b}_i)^\top$ $\tilde{a}_i, \tilde{b}_i \in \{-0.5, 0.5\}$ map the structure. The scaling factor of this RC is $\tilde{r}$=2. This cluster is called ${}_2$RC. As a consequence, it yields for $\phi_i^{[n]}$ as in Eq. (3.8) and for $\tilde{\phi}_i^{[n]}$

$$\begin{aligned} \phi_i^{[n]} &: [-3^{n-1} \cdot 0.5, 3^{n-1} \cdot 0.5]^2 \to [-3^n \cdot 0.5, 3^n \cdot 0.5]^2 \qquad & \phi_i^{[n]}(x) &= x + 3^{n-1} t_i \\ \tilde{\phi}_i^{[n]} &: [-2^{n-1} \cdot 0.5, 2^{n-1} \cdot 0.5]^2 \to [-2^n \cdot 0.5, 2^n \cdot 0.5]^2 \qquad & \tilde{\phi}_i^{[n]}(x) &= x + 2^{n-1} \tilde{t}_i . \end{aligned} \tag{4.7}$$

Some RCs with different probabilities p are depicted in Fig. 4.2.

4.2.2. The Generalized Random Carpet

The random carpet is a special case of a more general type of fractals, the *generalized random carpet* (GRC). Therefore, the construction algorithm and especially the definition of M_n in Eq. (4.1) has to be generalized as well.

To clarify the difference between RC and GRC the set M_n is redefined. Considering this, a multi-index $\hat{i}_j$ of length j with entries

$$\hat{i}_j = (i_1, i_2, \ldots, i_j) \tag{4.8}$$

is needed. The set M_k does not determine just one step like it does determine the k-th step for RC but j steps from the $((k-1)\cdot j+1)$-th to the $(k\cdot j)$-th step

$$M_k := \{\hat{i}_j \in \{1, \ldots, N\}^j : p_{i_1}^{[(k-1)\cdot j+1]} \cdot p_{i_2}^{[(k-1)\cdot j+2]} \cdot \cdots \cdot p_{i_j}^{[k\cdot j]} < p^j\}. \tag{4.9}$$

The structure after n iterated steps is

$$\mathrm{GRC}_n = \bigcup_{\hat{i}_j \in M_{\lceil \frac{n}{j} \rceil}} \Phi_{\hat{i}_j}^{[\lceil \frac{n}{j} \rceil]}(I). \tag{4.10}$$

As for the initial RC the image after the previous steps acts as the pre-image

$$\Phi_{\hat{i}_j}^{[k]}(I) = \phi_{\hat{i}_j}^{[k]}\left(\bigcup_{\hat{i}_j \in M_{k-1}} \Phi_{\hat{i}_j}^{[k-1]}(I)\right) \tag{4.11}$$

$$\phi_{\hat{i}_j}^{[k]}() = \phi_{i_j}^{[k\cdot j]}\left(\phi_{i_{j-1}}^{[k\cdot(j-1)]}\left(\cdots\left(\phi_{i_1}^{[(k-1)\cdot j+1]}()\right)\cdots\right)\right). \tag{4.12}$$

If $\lceil \frac{n}{j} \rceil \neq \frac{n}{j}$, the missing $p_i^{[n]}$ which are required to fill up $M_{\lceil \frac{n}{j} \rceil}$ are set to p. Additionally the missing maps are not defined as in Eq (3.3) but as the identity function id().

In contrast to the RC, the GRC is not mapped for every iterated step to the effect that the structure is fixed for the next steps. Only the structure of every j-th step is saved. Hence, for the first iterated step a random number $p_i^{[1]}$ is referred to all N unit cells due to the maps $\phi_i^{[1]}$ which are creating these cells. Like for the RC the cells with $p_i^{[1]} < p$ are created. In the next steps the unit cells get the random number $p_i^{[2]}$ due to $\phi_i^{[2]}$ and inherits the corresponding $p_i^{[1]}$. The cells are shown if the product of the random numbers smaller then p^2. This procedure is repeated till the j-th step. After this step the procedure starts again from step 1

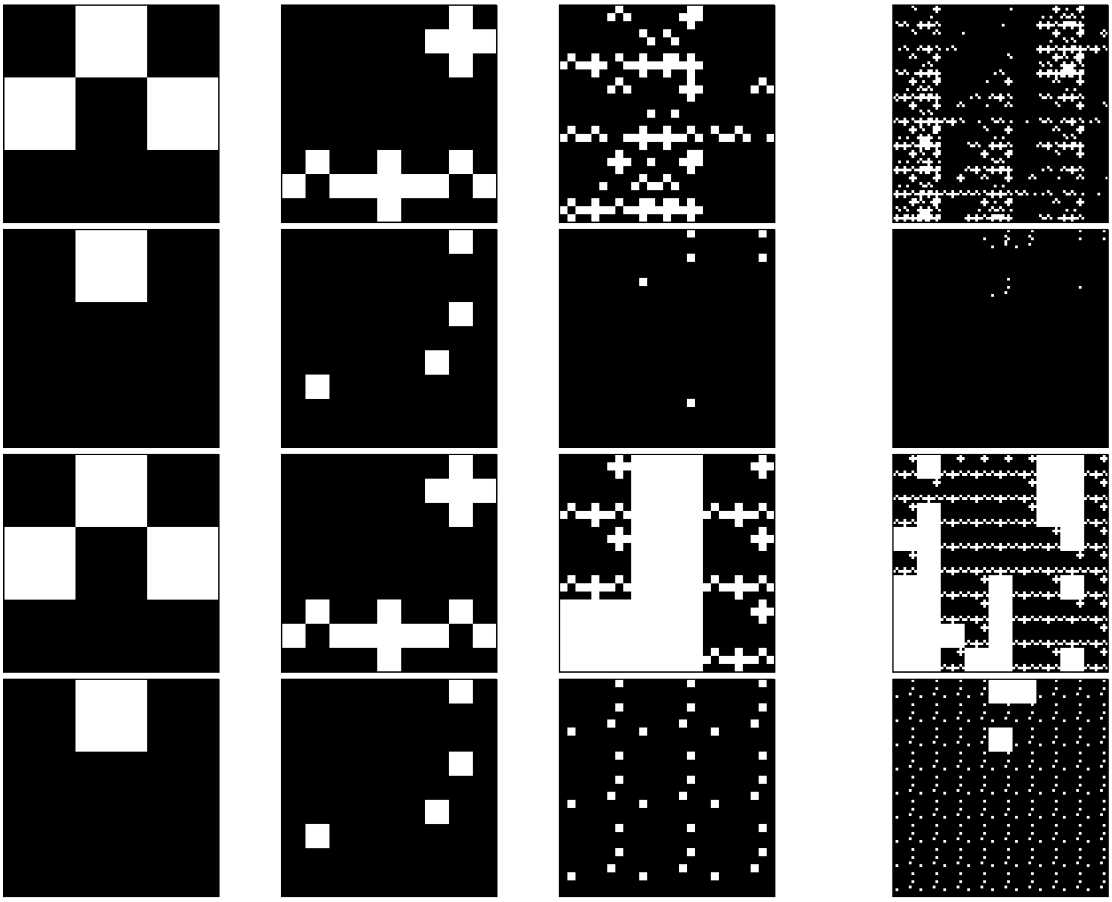

Figure 4.3.: The two top structures are representatives of the $_3$IRC with probability $p = 0.5$ (above) and $p = 0.8$ (below) in the first, second, third, and fourth iterated step, from left to right. The bottom structures are representatives of the $_3$GRC of type 2 with probability $p = 0.5$ (above) and $p = 0.8$ (below) in the first, second, third, and fourth iterated step, from left to right.

except that the structure after step j is used. The random numbers of all steps before are discarded. The structure is now called a generalized random carpet of type j. If $j = 1$, the set of Eq. (4.10) coincides with RC (see Eq. (4.2)). If $j = \infty$, the structure is dependent of all random numbers of all previous steps for every iterated step. In this thesis it is called the *infinite random carpet* (IRC). The IRS and the GRC of type 2 are depicted in Fig. 4.3.

By comparing the structures with the sets of Fig. 4.2 and Fig. 4.1, one notices that they differ except for the first step. The RC has a strong correlation between

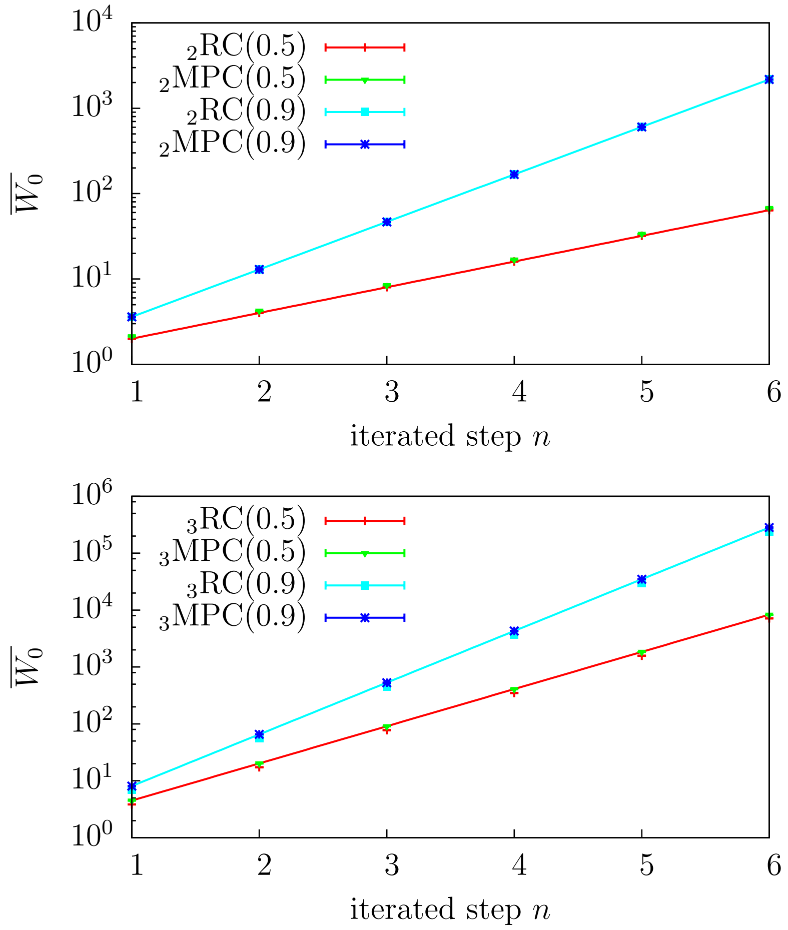

Figure 4.4.: The mean values $\overline{W_0}$ of $_2$MPC and $_2$RC at the top and of $_3$MPC and $_3$RC at the bottom are plotted using the probabilities $p = 0.5$ and $p = 0.9$ and lie within each error bars.

different cells. The MPC and IRC have no such obvious correlations. Thus, first the claim that MPC and RC are statistically equal up to the second rank tensors has to be proven. In order to do this the Minkowski functionals of 10,000 structures of $_2$MPC, $_2$RC, $_3$MPC, and $_3$RC with probability from $p = 0.5$ to $p = 0.9$ are calculated for the first six iterated steps. Thus, the mean values can be determined accurately. For the calculations it is necessary to determine that two sets which are only sharing a vertex are defined as not linked. One notices that all Minkowski functionals are similar and lie within the standard deviation of each other. In Fig. 4.4 this is illustrated using the example of W_0. This yields for $_2$MPC-$_2$RC as well as for $_3$MPC-$_3$RC. This is plausible because the single cells are part of the structure after step n with probability p^n independently from the rest of the structure. Thus, it does not matter if one talk about Mandelbrot percolation or random carpet in terms of the mean Minkowski functionals up to the rank-2 tensors.

4.2.3. Geometrical Properties

Cantor sets have extensively been investigated fractals. In these studies the structure and morphology of the cluster plays a major role. Dekking and Meester proved that with increasing the density with p from 0 to 1 a random Cantor set C in 2D passes through six phases [36]. These phases concern the projection of C onto one of the coordinate axes $\pi()$, the one dimensional Lebesgue measure $\lambda()$ and the Hausdorff dimension dim(). One has to take notice that in this procedure the Cluster is rescaled onto the unit square $[-0.5,0.5]^2$ after the construction is done. The phases are

I $C = \emptyset$

II $\mathbb{P}(C \neq \emptyset) > 0$ and $\dim(\pi(C)) = \dim(C)$

III $\dim(\pi(C)) < \dim(C)$

IV $0 < \lambda(\pi(C)) < 1$

V $\mathbb{P}(\lambda(\pi(C)) = 1) > 0$ but C does not percolate

VI C percolates with positive probability.

Let us explain these phases in some detail and also determine for which values of p the Cantor sets are in all these stages. To determine the transition thresholds of MPC the substitutions σ has to be consulted again (see chapter 4.2). Along with it, the sum m_i of probabilities in the i-th column of $\sigma(1)$ is defined. Because every entry is 1 with probability p, it yields $m_i = m \cdot p$ for all columns. Additionally, the phases are depicted in Fig. 4.5.

The first phase **I** emerges for small values of p, such that the set becomes almost surely an empty set after a finite number of steps. This happens if the expectation value of squares which are created by $\sigma(1)$ is not exceeding 1

$$\sum_{i=1}^{m} m_i \leq 1. \tag{4.13}$$

Consequently, for the MPC the boundaries of p are $0 \leq p \leq \frac{1}{m^2} = p_{I\to II}$. The critical values from phase I to II are $p_{I\to II} = \frac{1}{4}$ ($_2$MPC) and $p_{I\to II} = \frac{1}{9}$ ($_3$MPC).

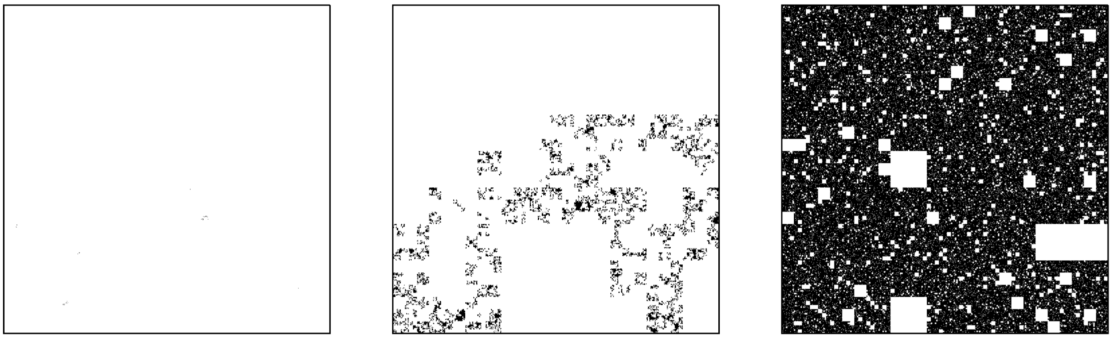

Figure 4.5.: The ${}_3$MPCs with different probabilities, representing the different phases of the Mandelbrot percolation are depicted. Counting from the left, the first structure is constructed with the probability $p = 0.2$ (phase II), the second with $p = 0.6$ (phase V), and the third with $p = 0.95$ (phase VI).

In phase **II** the probability that the set is even after infinite steps not empty becomes bigger than 0. Nevertheless, no noticeable clusters evolve. The set forms an often called dust. It is characterized by small values of its Hausdorff dimension which means that the dimension is nearly 0. If the dust is "thin" enough, the Hausdorff dimension of the projection onto the axis is as small as the actual dimension of the set. The transition probability from phase II to III can be calculated exactly as well [36]. It holds

$$\sum_{i=1}^{m} m_i \log m_i \leq 0 \tag{4.14}$$

and such $\frac{1}{m^2} \leq p \leq \frac{1}{m} = p_{II \to III}$. For ${}_2$MPC and ${}_3$MPC yields $p_{II \to III} = \frac{1}{2}$ and $p_{II \to III} = \frac{1}{3}$, respectively.

In phase **III** the set is still a dust. However, it is much "denser" than in phase II, such that the dimension of the set becomes greater than the dimension of its projection. Here the upper boundary can also be calculated exactly. p has to be small enough, such that

$$\sum_{i=1}^{m} \log m_i \leq 0. \tag{4.15}$$

However, the resulting upper boundary matches exactly with $p_{II \to III}$. Consequently, one can say that phase III does not appear for a MPC.

A set in phase **IV** shapes small visible clusters. Now the set is not defined as a dust anymore. As a consequence of these clusters, the projection set is no union of scattered points but has a noticeable extension. The Lesbegue measure becomes larger than 0. However, the clusters are too small, such that the possibility that the projection is equal to the unit interval [-0.5,0.5] is almost surely 0. Falconer et. al. proved that as phase III this phase does not exist for any MPC [37]. Therefore, the MPC jumps from phase II directly to phase V, such that it is better to redefine $p_{II \to III}$ to $p_{II \to V}$.

The most studied phase transition is the transition between phase **V** and **VI**. In phase V the clusters are so large that π(MPC)=[-0.5,0.5] with positive probability. However, the system does not percolate. This first happens in phase VI. A system percolates if the set has a connected subset which has a nonempty intersection with the upper and lower side of the unit square. However, until yet there is no way found to calculate the transition between these phases equivalent to the critical probability $p_c = p_{V \to VI}$ analytically. Hence, there is a great effort to give boundaries and narrow them down. The latest results of the boundaries of a recently published paper by Don [38] yield

$$\begin{array}{lll} {}_2\text{MPC} & 0.881 & \leq p_c(2) \leq 0.993 \\ {}_3\text{MPC} & 0.784 & \leq p_c(3) \leq 0.940. \end{array} \tag{4.16}$$

To get more precise values, the percolation threshold p_c has to be calculated numerically. A finite size scaling analysis is performed [39, 40]. The pseudo critical points $p_c(n)$ of ${}_2$MPC and ${}_3$MPC are plotted against the inverse value of the iterated step n.[1] The plots can be seen in Fig. 4.6. In this plots the data intersects the y-axis at the point $p_c(\infty)$ which is identified as the percolation threshold of the infinitely iterated cluster p_c. By subtracting the data from p_c and plotting it double logarithmically, it follows a straight line. Thus, one determines that the fitting function is

$$p_c(n) \approx p_c + c \cdot n^{-\frac{1}{\nu}}. \tag{4.17}$$

Although this law is empirical for MPC, it can be deduced for RC.

Assume a random carpet ${}_\nu$RC. Let q be be the probability that the map is no element of IFS $q = 1 - p$. $Q_0(q)$ is the probability that a percolating system is also percolating after the next step

$$Q_0(q) = q^N + c_{n-1} q^{n-1} p + \cdots + c_\nu q^\nu p^{n-\nu}. \tag{4.18}$$

---

[1] Please note that now the initial definition of construction is used again. The structure is not rescaled and the observation window increases by the factor m for every step.

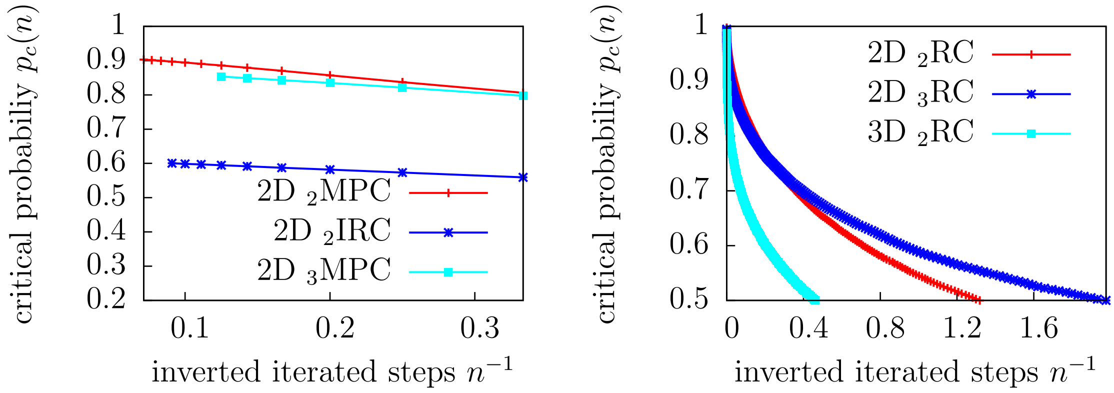

Figure 4.6.: The finite size scaling of $_2$MPC, $_3$MPC, $_2$IRC, $_2$RC and $_3$RC in two dimensions and $_2$RC in three dimensions.

The probability $Q(q,n)$ that the percolation terminates at step n is

$$Q(q,n) = Q_0(q)(1 - Q_0(q))^{n-1}. \tag{4.19}$$

The mean step $\overline{n}$ at which the system does not percolate anymore is

$$\begin{aligned}
\overline{n} &= \sum_{\tilde{n}=1}^{\infty} \tilde{n} Q(q,\tilde{n}) = Q_0(q) \sum_{\tilde{n}=1}^{\infty} \tilde{n}(1 - Q_0(q))^{\tilde{n}-1} = \\
&= -Q_0(q) \frac{\partial}{\partial x} \sum_{i=0}^{\infty} (1-x)^i \bigg|_{x=Q_0(q)} = \\
&= -Q_0(q) \frac{\partial}{\partial x} \frac{1}{x} \bigg|_{x=Q_0(q)} = \frac{1}{Q_0(q)} \\
&\xrightarrow{p\to 1} \frac{1}{c_\nu} q^{-\nu}.
\end{aligned} \tag{4.20}$$

It yields for the percolation threshold of the structure after n iterated steps

$$p_c(n) \xrightarrow{n\to\infty} 1 - c_\nu^{-\frac{1}{\nu}} n^{-\frac{1}{\nu}}. \tag{4.21}$$

Using $p_c = 1$ and $c = -c_\nu^{-\frac{1}{\nu}}$, one gets Eq. (4.17).

With this knowledge the parameters c and $\frac{1}{\nu}$ are predicted. The only necessary quantities due to Eq. (4.18) and Eq. (4.21) are the smallest number of cells ν which are able to terminate the percolation after a step and their number of

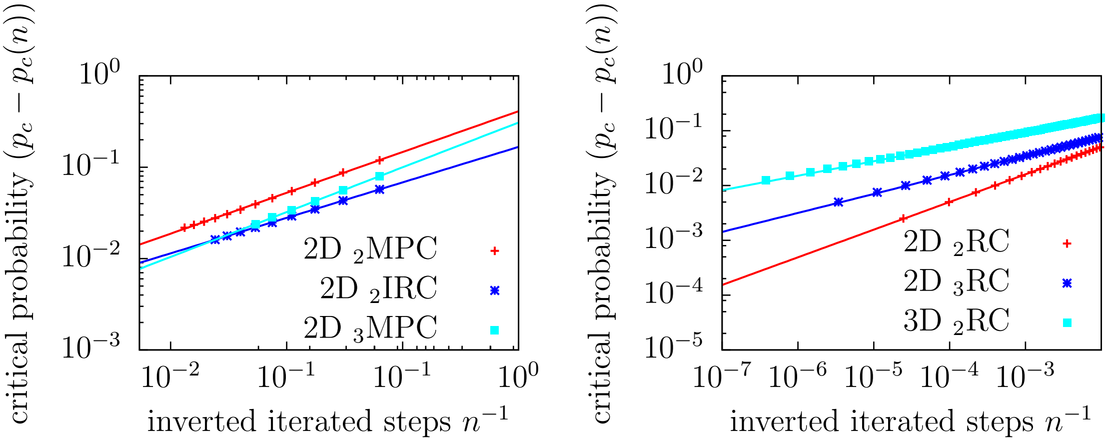

Figure 4.7.: The finite size scaling of $_2$MPC, $_3$MPC, $_2$IRC, $_2$RC, and $_3$RC in two dimensions and $_2$RC in three dimensions. The critical probability is subtracted by the critical probability of a system after the n-th iterated step to calculate ν out of the slope.

combination c_ν. For $_2$RC in two and three dimensions the values are $\nu = 2$ and $c_2 = 4$ and $\nu = 4$ and $c_4 = 16$, respectively. The parameters are $(c,\frac{1}{\nu})$=(0.5,0.5) $_2$RC in 2D and $(c,\frac{1}{\nu})$=(0.25,0.5) $_2$RC in 3D. For $_3$RC in two dimensions the values are $\nu = 3$, $c_3 = 18$ and $(c,\frac{1}{\nu})=(\frac{1}{3}, \frac{1}{\sqrt[3]{18}} \approx 0.382)$. In Fig. 4.7 the finite size scaling of these RCs are also plotted. By fitting the data to the fitting function, the prediction vindicates. This can be seen for the fitting parameter which are listed in Table 4.1. p_c is 1 for every RC, thus close to the analytically calculated parameter.

Let us return to MPC and also consult IRC. The results of the fits are also listed in Table 4.1. The percolation thresholds of MPC seems reliable. For both sets p_c lies within the range bounded in Eq. (4.16). However, no claims can be done for the parameter c and ν as it can be done for RC. Furthermore, ν must not be confused with the critical exponent concerning the correlation length ξ. As already mentioned in the Introduction 1, the critical exponents describe the behavior of certain quantities close or at the threshold p_c. It holds [40, 41]

$$\xi \approx |p_c - p|^{-\nu_{crit}}. \tag{4.22}$$

At $p_c(x)$ ξ can be replaced by the system size x because of the self-similarity and the correlation due to percolation at that range. The iterated step n states the size x of the set indeed. Nevertheless, it can not be equated with ξ.

For that same reason only p_c is discussed for GRC. In general, the threshold depends on the type of the GRC. The higher the type of the GRC is the lower

structure	${}_2$RC 2D	${}_2$RC 3D	${}_3$RC 2D	${}_2$MPC 2D	${}_3$MPC 2D	${}_2$IRC 2D
p_c	1	1	1	0.925	0.877	0.617
c	0.520	0.582	0.377	0.411	0.309	0.166
$\frac{1}{\nu}$	0.504	0.264	0.346	1.12	1.232	0.963

Table 4.1.: The fitting parameter of a finite size scaling are listed in this Table. At this the percolation thresholds and other parameter due to Eq. (4.17) of some iterated random fractals are calculated. The corresponding plots are depicted in Fig. 4.6 and Fig. 4.7.

is the threshold. Therefore, the range is bounded above by the threshold of RC which is calculated $p_c = 1$ and bounded below by the threshold of IRC. Here the fitted critical probability attracts attention. It is very close to the percolation threshold of the site-percolation $p_{site} = 0.592746010(2)$ [42]. This structure is one of the fundamental percolating problems which will be approached and explained in greater detail in chapter 6.3. Briefly speaking, it is a set of unit cells on a $m \times m$ lattice which are a part of the structure with probability p. At the limit $n \to \infty$ it can be argued that the IRC transitions into a site percolation cluster on an infinite lattice. In this case every cell has a product of infinitely many random numbers. Consequently, the products become uncorrelated among themselves. The unit cell is not vanished after infinite steps with probability p. This is equivalent to site-percolation. The threshold is identified as $p_{c,\mathrm{IRC}} = p_{site}$. Now one can state the boundaries of p_c of GRC

$$p_{c,\mathrm{IRC}} = 0.592746 \leq p_{c,\mathrm{GRC}} \leq p_{c,\mathrm{RC}} = 1. \tag{4.23}$$

4.3. Subterms of Mandelbrot Percolation

Taking a closer look at the Minkowski functionals and plotting them, one recognize the already achieved observations for every probability (see Fig. 4.8 and Fig. 4.9). The assumption of d_f and $d_f + 2$ being the dominant term, respectively, is given.

To get the exact values, the Minkowski functionals are also calculated analytically shown in Appendix C. At this calculations the functionals of a structure are weighted with the probability that this particular structure occurs $P = p^m(1-p)^{N-m}$ with $m = |M_n|$. The Minkowski functionals of ${}_3$MPC are determined by Table 4.2. The functionals of ${}_2$MPC are shown in Table 4.3.

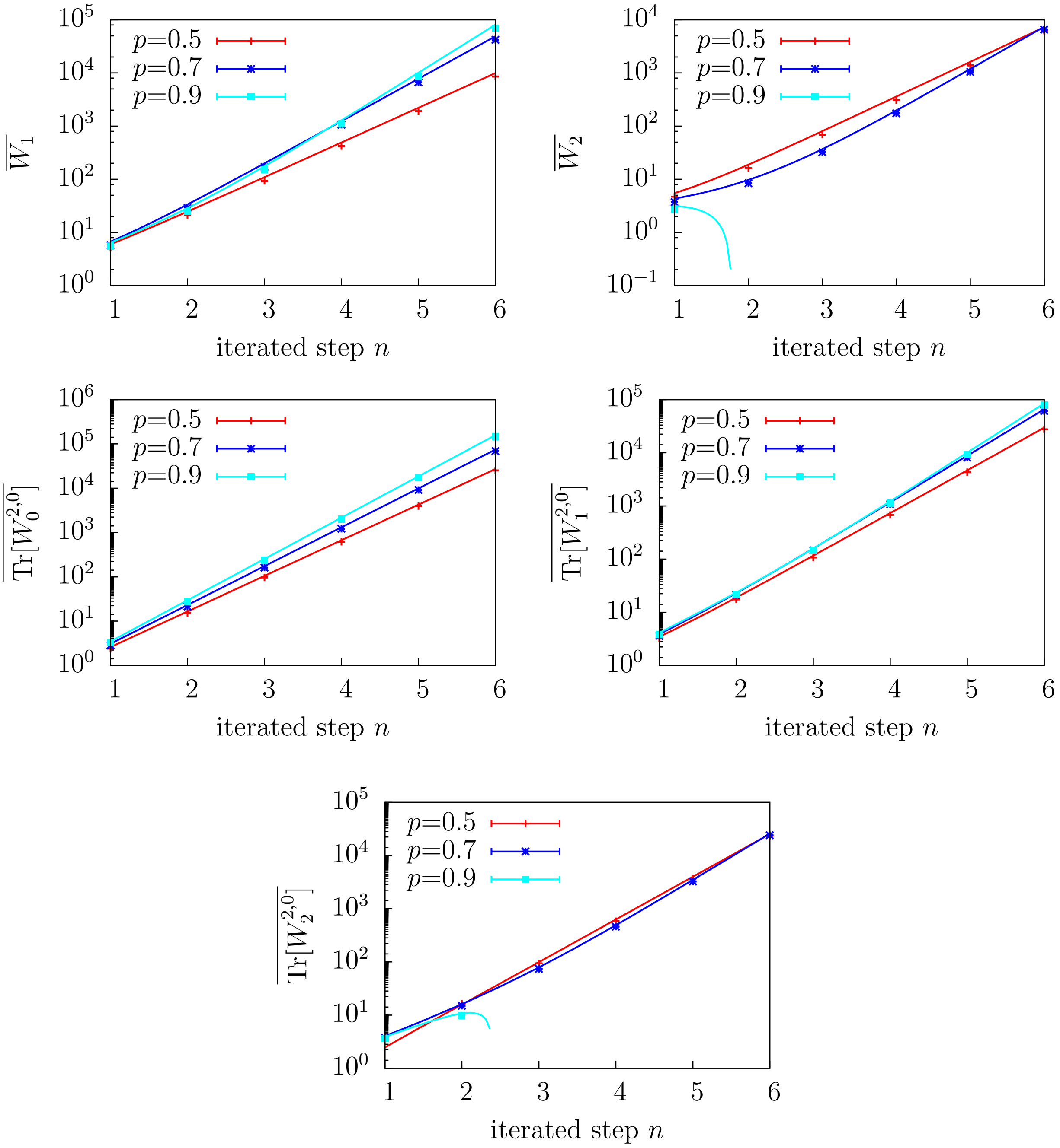

Figure 4.8.: The mean Minkowski functionals of 10,000 ${}_3$MPC clusters in two dimensions are plotted. Additionally, the analytically calculated progressions with the parameters listed in Table 4.2 are shown.

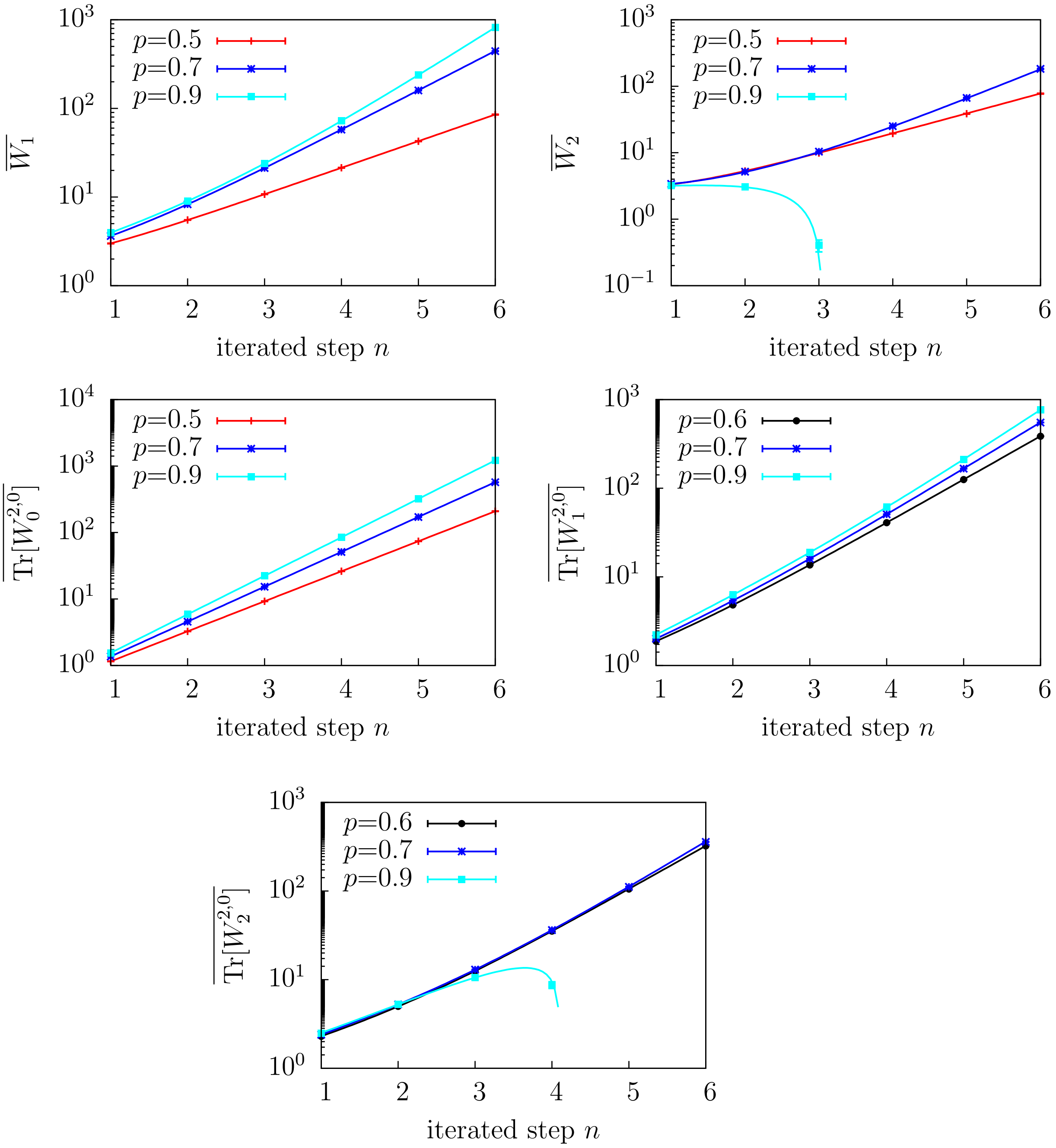

Figure 4.9.: The mean Minkowski functionals of 10,000 $_2$MPC clusters in two dimensions are plotted. Additionally, the analytically calculated progressions with the parameters listed in Table 4.3 are shown.

ν	0	1	2	3
d_ν	$\log_3 9p$	$\log_3 3p^2$	$\log_3 p^4$	$d_0 - 2$
$w_{0;\nu}$	1	–	–	–
$w_{1;\nu}$	$\frac{6(1-p)}{3-p}$	$\frac{4p}{3-p}$	–	–
$w_{2;\nu}$	$\frac{9(3-5p+p^3+p^4)}{(3-p)(9-p^3)}\pi$	$\frac{12p(1-p^2)}{(3-p)(3-p^2)}\pi$	$\frac{4p^3(3+p^2)}{(3-p^2)(9-p^3)}\pi$	–
$w_{0;\nu}^{2,0}$	$\frac{1}{6}$	–	–	0
$w_{1;\nu}^{0,2}$	$\frac{6(1-p)}{3-p}$	$\frac{4p}{3-p}$	–	–
$w_{1;\nu}^{2,0}$	$\frac{1-p}{3-p}$	$-\frac{4p(1+p)}{3(1-3p)(3-p)}$	–	$\frac{1-p}{3(1-3p)}$
$w_{2;\nu}^{2,0}$	$\frac{(1-p)(2187-1458p-1458p^2-725p^3+4p^4)}{486(3-p)(9-p^3)}\pi$	$-\frac{2p(1-p)(459+487p)(1+p)}{243(1-3p)(3-p)(3-p^2)}\pi$	$\frac{2p(216+208p+235p^2+219p^3+84p^4+9p^5+9p^6)}{81(3-p^2)(9-p^3)(1+p+p^2)}\pi$	$\frac{27-18p+30p^2-35p^3-2p^4}{81(1-3p)(1+p+p^2)}\pi$

Table 4.2.: This table determines the mean Minkowski functionals of ${}_3$MPC up to the rank-2 tensors (see Eq. (3.11) and Appendix C). The fractal dimension, the subdimensions, and the fractal amplitudes are listed.

ν	0	1	2	3
d_ν	$\log_2 4p$	$\log_2 2p^2$	$\log_2 p^4$	$d_0 - 2$
$w_{0;\nu}$	1	–	–	–
$w_{1;\nu}$	$\frac{4(1-p)}{2-p}$	$\frac{2p}{2-p}$	–	–
$w_{2;\nu}$	$\frac{4(2-3p+p^4)}{(2-p)(4-p^3)}\pi$	$\frac{4p(1-p^2)}{(2-p)(2-p^2)}\pi$	$\frac{p^3(2+p^2)}{(2-p^2)(4-p^3)}\pi$	–
$w_{0;\nu}^{2,0}$	$\frac{1}{6}$	–	–	0
$w_{1;\nu}^{0,2}$	$\frac{4(1-p)}{2-p}$	$\frac{2p}{2-p}$	–	–
$w_{1;\nu}^{2,0}$	$\frac{2(1-p)}{3(2-p)}$	$-\frac{p(1+p)}{3(1-2p)(2-p)}$	–	$\frac{1-p}{3(1-2p)}$
$w_{2;\nu}^{2,0}$	$\frac{(1-p)(64-32p-32p^2-31p^3+p^4)}{48(2-p)(4-p^3)}\pi$	$-\frac{p(1-p)(8+11p)(1+p)}{16(1-2p)(2-p)(2-p^2)}\pi$	$\frac{p(8+7p+7p^2+6p^3+2p^4)}{8(2-p^2)(4-p^3)(1+p+p^2)}\pi$	$\frac{8-4p+2p^2-11p^3-p^4}{24(1-2p)(1+p+p^2)}\pi$

Table 4.3.: This table determines the mean Minkowski functionals of ${}_2$MPC up to the rank-2 tensors (see Eq. (3.11) and Appendix C). The fractal dimension, the subdimensions and the fractal amplitudes are listed.

The calculated Minkowski functionals show the same behavior as observed in Eq. (3.11) for the Sierpiński carpet. This assumption is thus confirmed for the random iterated fractals. Particularly as W_2 has a surface term despite it could not be determined for the Sierpiński carpet. Even though $W_0^{2,0}$ has no fractal term, the functionals have the predicted pyramid shape that every Minkowski functional concerning the measure of the next smallest topological dimension gets an additional subdimensional term. The original intuitive guess of chapter 3.2 is not observable again because the dimension differences $\Delta_1 d = \log_3 \frac{p}{3}$ and $\Delta_1 d = \log_2 \frac{p}{2}$ are unequal to -1 and even dependent of p. Therefore, one can argue that the subdimensions are not directly dependent of the fractal dimension.

5. Information of Fractal Subterms

After the existence of subdimensions by both simulations/computational analysis and by analytical calculations has been shown, it has to be discussed what kind of informations the additional terms contain. In the course of this, two different approaches are considered. For the first approach the term of dimension are extended from the real to the complex world to get more knowledge about fractal geometry. Therefore, fractal springs and sprays are defined [43]. In the second approach we take a closer look at the Sandbox method to calculate the dimensions.

5.1. Fractal Strings and Fractal Sprays

A *fractal string* $\mathcal{L}$ is a bounded open subset $\Omega \subset \mathbb{R}$ which consists of countable intervals. These intervals have specific lengths l_i which are also known as length of the strings. Without loss of generality one can assume that $l_i \geq l_j \geq 0 \ \forall i, j \in \mathbb{N}\colon i < j$. Ω can also be a finite union of intervals. In that case the number K of lengths $\{l_i\}_{i=1}^{K}$ is finite.

5.1.1. Geometric Zeta Function

Let $\mathcal{L}$ be a fractal string with lengths $\{l_i\}_{i=1}^{\infty}$, then the *geometric zeta function* is defined as

$$\zeta_{\mathcal{L}}(s) := \sum_{i=1}^{\infty} l_i^s = \sum_{l} \omega_l l^s \tag{5.1}$$

with ω_l being the *multiplicity* of l: $\omega_l = \#\{j \geq 1\colon l_j = l\}$.

It is shown that the zeta functions contain geometric and spectral information about the string. In addition to the measurability they also contain the fractal dimension of the string [43]. One can show that there exists a $\sigma \in \mathbb{R}$ for which the series of $\zeta_{\mathcal{L}}$ converges in the half plane $\Re s > \sigma$. However, at $s = \sigma$ the geometric zeta function diverges. σ is called the *abscissa of convergence* of the fractal string. For infinitely many lengths the abscissa of convergence is identical with the Hausdorff-Besicovitch-dimension and the fractal dimension of the string thereby. It yields

$$D_{f,\mathcal{L}} := \sigma_{\mathcal{L}} = \inf\{a \in \mathbb{R}\colon \sum_{i=1}^{\infty} l_i^a < \infty\}. \tag{5.2}$$

5.1.2. Spectral Zeta Function

The fractal string $\mathcal{L}$ is often defined by frequencies instead of lengths. Also in this thesis frequencies are used for transition from structures living in one dimensions (fractal string) to structures in higher dimensions (fractal sprays) [43, 44]. Therefore, $\Omega \subset \mathbb{R}$ is considered together with the Dirichlet Laplacian $\Delta = -\frac{\mathrm{d}^2}{\mathrm{dx}^2}$ on Ω. The frequencies of $\mathcal{L}$ are $f_j = k \cdot l_j^{-1}$ with $k, i \in \mathbb{N}$. The multiplicity of f is $\omega_f = \sum\limits_{j\colon f \cdot l_j \in \mathbb{N}} 1$.

The definition of the *spectral zeta function* is analogous to the geometric zeta function

$$\zeta_\nu(s) := \sum_{k,i=1}^{\infty} (k \cdot l_i^{-1})^{-s} = \sum_f \omega_f f^{-s}. \tag{5.3}$$

An other way to calculate the spectral zeta function is to put it in dependence of $\zeta_{\mathcal{L}}$

$$\zeta_\nu(s) = \sum_{k,i=1}^{\infty} k^{-s} l_i^s = \sum_{k=1}^{\infty} k^{-s} \sum_{i=1}^{\infty} l_i^s = \zeta(s)\zeta_{\mathcal{L}}(s). \tag{5.4}$$

$\zeta(s)$ is the Riemann zeta function

$$\zeta(s) = \sum_{k=1}^{\infty} k^{-s} \tag{5.5}$$

which is equivalent to the spectral zeta function on an interval with length 1.

The next step is to generalize the fractal strings in $d = 1$ to fractal sprays in $d \geq 2$. Let $B \subset \mathbb{R}^d$ be a nonempty bounded open set. The set Ω is called fractal spray $\mathcal{L}$ of B if there is a disjoint union of open sets Ω_i $i \in \mathbb{N}$ where Ω_i is congruent to $l_i \cdot B$. This definition of a fractal spray coincides with the fractal string. A fractal string can be seen as a fractal spray with B being an interval on $\mathbb{R}$. To calculate the spectral zeta function of the fractal spray, the spectral zeta function of B is needed: $\zeta_B = \sum_{k=1}^{\infty} f_k(B)^{-s}$. $f_k(B)$ are the frequencies of the Laplacian Δ on B and are in relation to the eigenvalues $\lambda_k(B)$ of Δ: $f_k(B) = \pi^2\sqrt{\lambda_k(B)}$. Consequently, it yields for $\zeta_B(s)$

$$\zeta_B(s) = \sum_{k=1}^{\infty} f_k(B)^{-s} = \pi^s \sum_{k=1}^{\infty} \lambda_k(B)^{-\frac{s}{2}}. \tag{5.6}$$

It follows that the spectral zeta function of the fractal spray is a generalization of Eq. (5.4)

$$\zeta_\nu(s) = \zeta_{\mathcal{L}}(s)\zeta_B(s). \tag{5.7}$$

5.1.3. Self-Similar Fractal Strings/Sprays

After the definition of the zeta functions and the fractal strings/sprays is discussed, we take a brief look at fractal self-similar strings/sprays [4, 43, 45].
Let $I \subset \mathbb{R}^d$ be a closed interval in $d \geq 1$ dimensions of volume V. $\mathcal{L}$ becomes a self-similar string by constructing it with $N \geq 2$ maps $\phi_i \colon I \to I \; i \in \{1, \dots, N\}$ which contracts I with the factors r_i with $\sum_{i=1}^{N} r_i < 1$. The sets $\phi_i(I)$ and $\phi_j(I)$ do not overlap $\phi_i(I) \cup \phi_j(I) = \emptyset \; \forall i, j \in \{1, \dots, N\} \colon i \neq j$. I is divided into N subintervals thereby. The remaining $K \geq 1$ intervals G_k are called gaps with a volume $v_k = g_k V \; k \in \{1, \dots, K\}$. It follows

$$I = \bigcup_{i=1}^{N} \phi_i(I) \cup \bigcup_{j=1}^{K} G_k. \tag{5.8}$$

The gap volumes v_k are the first strings of the fractal string. Repeating this with the remaining intervals after every step, one gets a set $F \subset I$

$$F := \bigcap_{n=0}^{\infty} \bigcup_{J \in \mathcal{J}_n} \Phi_J(I) \tag{5.9}$$

where each integer

$$\mathcal{J}_n := \{1, \dots, N\}^n \tag{5.10}$$

denotes the set of all finite sequences of length n in the symbols 1,. . . ,N and for $J = (j_1, \dots, j_n) \in \mathcal{J}_n$

$$\Phi_J := \phi_{j_n} \circ \dots \circ \phi_{j_2} \circ \phi_{j_1}. \tag{5.11}$$

The set F now satisfies the fixed point equation

$$F = \bigcup_{i=1}^{N} \phi_i(F). \tag{5.12}$$

F is then called a self-similar set. This procedure should remind the reader of the construction algorithm explained in chapter 3.1. By comparing both algorithms, one notices that for every step n the structure obtained by the just introduced algorithm is equal to the structure constructed with the algorithm of chapter 3.1 normalized on I. Nevertheless, the algorithms are not equal. The major differences are explained later in chapter 5.3.

The calculation of the geometric zeta function is straightforward. The lengths of the self-similar fractal spray $\mathcal{L}$ of F are in terms of $l = r_{\nu_1} r_{\nu_2} \dots r_{\nu_q} g_k L$ with $q \in \mathbb{N}$, $\nu_i \in \{1, \dots, N\}$ and $k \in \{1, \dots, K\}$. From Eq. (5.1) it yields for the geometric zeta function

$$\begin{aligned}\zeta_{\mathcal{L}}(s) &= \sum_{k=1}^{K} \sum_{q=1}^{\infty} \left(\sum_{\nu_1=1}^{N} \cdots \sum_{\nu_q=1}^{N} (r_{\nu_1} r_{\nu_2} \dots r_{\nu_q} g_k L)^s \right) \\ &= \sum_{k=1}^{K} (g_k L)^s \sum_{q=1}^{\infty} \left(\sum_{j=1}^{N} r_j^s \right)^q \\ &= \frac{L^s \sum\limits_{k=1}^{K} g_k^s}{1 - \sum\limits_{j=1}^{N} r_j^s}.\end{aligned} \tag{5.13}$$

5.1.4. Zeta Function of Iterated Fractals

To demonstrate the calculation with fractal sprays, the spray of the Sierpiński carpet introduced in chapter 3.2 is determined first. Therefore, one starts with the union square $I = [0,1]^2 \subset \mathbb{R}^3$. The Sierpiński Carpet has eight contraction mappings $\phi_1, \dots, \phi_8$ with $\phi_i \colon I \to I$ $\phi_i = \frac{x}{3} + (a_i, b_i)^\top$ for $a_i, b_i \in \{0, \frac{1}{3}, \frac{2}{3}\}$ without $a_i = b_i = \frac{1}{3}$. Consequently, the contraction factors are $r_i = \frac{1}{3}$ and the gap size is $g = \frac{1}{3}$. Now these values and the length of the unit square $L = 1$ into Eq. (5.13) are inverted

$$\zeta_{\mathcal{L}_{\text{Sierp}}}(s) = \frac{3^{-s}}{1 - 8 \cdot 3^{-s}}. \tag{5.14}$$

This is the geometric zeta function of the string characterizing the Sierpiński carpet. The spectral zeta function of the Sierpiński carpet is

$$\zeta_{\nu_{\text{Sierp}}}(s) = \frac{3^{-s}}{1 - 8 \cdot 3^{-s}} \sum_{m_1, m_2 = 1}^{\infty} (m_1^2 + m_2^2)^{-\frac{s}{2}}. \tag{5.15}$$

Here Eq. 5.7 and the spectral zeta function of the unit square $\zeta_{[0,1]^2}(s)$ are used with

$$\zeta_{[0,1]^2}(s) = \sum_{m_1,m_2=1}^{\infty} (m_1^2 + m_2^2)^{-\frac{s}{2}}. \tag{5.16}$$

To determine the fractal dimension, the discontinuity of $\zeta_{\nu_{\text{Sierp}}}$ is examined. The equation $0 = 1 - 8 \cdot 3^{-s}$ results in the fractal dimension of the Sierpiński carpet $s = D_f = \log_3 8$. By extending the values of s into the complex domain, one gets further results for the equation $0 = 1 - 8 \cdot 3^{-s}$. In this way the period $p = \frac{2\pi}{\ln 3}$ has to be added, called the *oscillatory period*. As a result, a set of dimensions characterizing the carpet is stated

$$D_{\text{Sierp}} = \{\log_3 8 + in\frac{2\pi}{\ln 3} : n \in \mathbb{Z}\}. \tag{5.17}$$

This shows that the dimension of the Sierpiński carpet is not a purely real number. Consequently, it is expected that oscillations reflect geometric properties (see Fig 5.1).

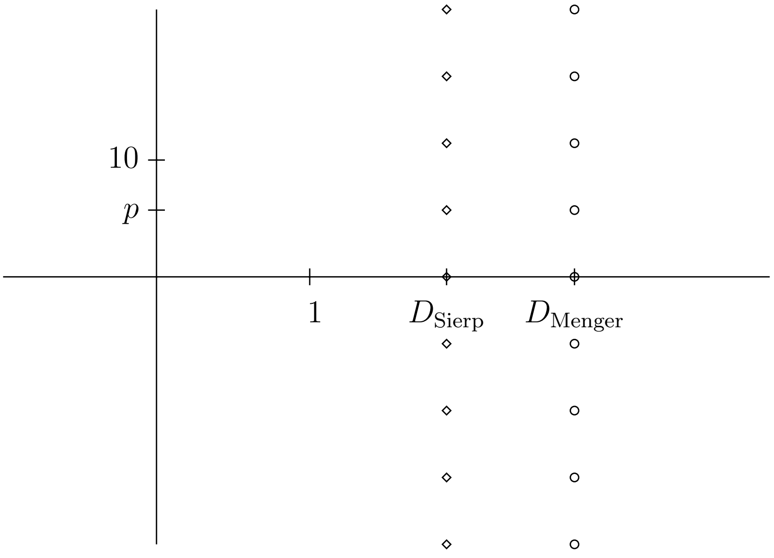

Figure 5.1.: The complex dimensions of the Sierpiński carpet (◇) and the Menger's sponge (○) are plotted (see Eq. (5.17) and Eq. (5.21)). $D_{\text{Sierp}} = \log_3 8$, $D_{\text{Menger}} = \log_3 20$ and $p = \frac{2\pi}{\ln 3}$.

The calculation of the zeta function of the Menger's sponge is analogous (see chapter 3.3). The starting set is the union cube $I = [0,1]^3 \subset \mathbb{R}^3$. It has 20 contraction maps $\phi_i\colon I \to I$ $\phi_i = \frac{x}{3} + (a_i, b_i, c_i)^\top$ with $a_i, b_i, c_i \in \{0, \frac{1}{3}, \frac{2}{3}\}$ except the cases $\forall x, y \in \{a_i, b_i, c_i\}$ $x \neq y\colon x = y = \frac{1}{3}$. Consequently, there are 20 maps with the contraction factors $r_i = \frac{1}{3}$ $\forall i$ and seven gaps with gap size $g_k = \frac{1}{3}$ $\forall k$. Eq. 5.13 denotes the geometric zeta function

$$\zeta_{\mathcal{L}_{\text{Menger}}}(s) = \frac{7 \cdot 3^{-s}}{1 - 20 \cdot 3^{-s}}. \tag{5.18}$$

Together with Eq. (5.7) and the spectral zeta function of the unit cube

$$\zeta_{[0,1]^3}(s) = \sum_{m_1, m_2, m_3 = 1}^{\infty} (m_1^2 + m_2^2 + m_3^2)^{-\frac{s}{2}}, \tag{5.19}$$

the spectral zeta function of the Menger's sponge is given by

$$\zeta_{\nu_{\text{Menger}}}(s) = \frac{7 \cdot 3^{-s}}{1 - 20 \cdot 3^{-s}} \sum_{m_1, m_2, m_3 = 1}^{\infty} (m_1^2 + m_2^2 + m_3^2)^{-\frac{s}{2}}. \tag{5.20}$$

The set of dimensions characterizing the Menger's sponge is

$$D_{\text{Menger}} = \{\log_3 20 + in\frac{2\pi}{\ln 3}\colon n \in \mathbb{Z}\}. \tag{5.21}$$

$\log_3 20$ coincides with the fractal dimension of the Menger's sponge (see Fig 5.1). Hence, the Menger's sponge also contains oscillations.

5.2. Random Fractal String and Random Fractal Sprays

In addition to the Sierpiński carpet and the Menger's sponge another fractal the Mandelbrot percolation cluster was introduced in this thesis. This fractal also can be defined as a fractal spray. However, it is a special fractal spray, namely a random fractal spray. The random fractal strings are precisely discussed especially by Hambly et al. [46].

As the random fractal spray is not built like a typical fractal spray, the differences from the self-similar sprays have to be mentioned. Let I be a closed interval $I \subset \mathbb{R}^d$ $d \geq 1$ and $\phi_i, \dots, \phi_N$ with $\phi_i\colon I \to I$ N maps which contract I with the factors $r_1, \dots, r_N$ with $\sum_{i=1}^{N} r_i^d = 1$. The images $\phi_i(I)$ and $\phi_j(I)$ do not overlap, i.e. $\phi_I \cap \phi_j = \emptyset$ $\forall i, j \in \{1, \dots, N\}$. For every iterated step n the set is mapped by each ϕ_i independently with the probability p. Consequently, one gets two sets M_n and $\overline{M_n}$

$$\begin{aligned} M_n &= \{i \in \{1, \dots, N\} \colon \text{ structure is mapped by } \phi_i \text{ in step } n\} \\ \overline{M_n} &= \{i \in \{1, \dots, N\} \colon \text{ structure is not mapped by } \phi_i \text{ in step } n\}\,. \end{aligned} \tag{5.22}$$

It follows $M_n \cup \overline{M_n} = \{1, \dots, N\}$ and $M_n \cap \overline{M_n} = \emptyset$.

The contraction factors r_i $i \in M_n$ and the gap sizes $g_k = r_k$ $k \in \overline{M_n}$ can be determined from the functions which map the structure. Now let $\Phi_{J_n}(I) = \phi_{j_n} \circ \dots \circ \phi_{j_1}(I)$ with $j_i \in M_n$ be the image of I after the n-th step characterized by the symbol $J_n = \{j_1, \dots, j_n\}$. $\mathcal{J}_n = \{1_n, \dots, N_n\}$ is the set of all N_n maps after n steps determining the fractal. As for the ordinary fractal spray the gaps are the elements of the random fractal spray $\mathcal{L}$. The fractal set F can be defined as

$$F := \bigcap_{n=1}^{\infty} \bigcup_{i \in \mathcal{J}_n} \Phi_i(I). \tag{5.23}$$

It has been shown that the mean geometric zeta function of a random fractal spray can be calculated by the expectation values $\mathbb{E}[\sum\limits_{k \in \overline{M}} g_k^s]$ and $\mathbb{E}[\sum\limits_{i \in M} r_i^s]$ and a modification of Eq. (5.13) [46]

$$\mathbb{E}[\zeta_{\mathcal{L}}](s) = \frac{L^s \mathbb{E}[\sum\limits_{k \in \overline{M}} g_k^s]}{1 - \mathbb{E}[\sum\limits_{i \in M} r_i^s]}. \tag{5.24}$$

The necessary probabilities for certain $\sum\limits_{k \in \overline{M}} g_k^s$ and $\sum\limits_{i \in M} r_i^s$ are the probabilities $P(\overline{M})$ and $P(M)$. The indices k and i are represented by the sets $\overline{M}$ and M. The mean zeta function contains like the zeta function of an ordinary fractal spray the fractal dimension and its oscillatory periods.

For the two examples already covered in this thesis – ${}_2$MPC and ${}_3$MPC – the mean geometric zeta functions are calculated. The initiator of ${}_\eta$MPC is the union square $I = [0, 1]^2$. The contraction maps are in case of ${}_3$MPC $\phi_i(x) = \frac{x}{3} + (a_i, b_i)^\top$ with $a_i, b_i \in \{0, \frac{1}{3}, \frac{2}{3}\}$. The map with $a_i = b_i = \frac{1}{3}$ is also included for the fractal, such that there are 9 maps $\phi_i \colon I \to I$. In the case of ${}_2$MPC there are four contraction maps $\phi_i \colon I \to I$ $\phi_i(x) = \frac{x}{2} + (a_i, b_i)^\top$ with $a_i, b_i \in \{0, \frac{1}{2}\}$. The scaling factors r_i and the gap sizes g_i corresponding to ϕ_i are $r_i = g_i = \frac{1}{3}$ and $r_i = g_i = \frac{1}{2}$, respectively.

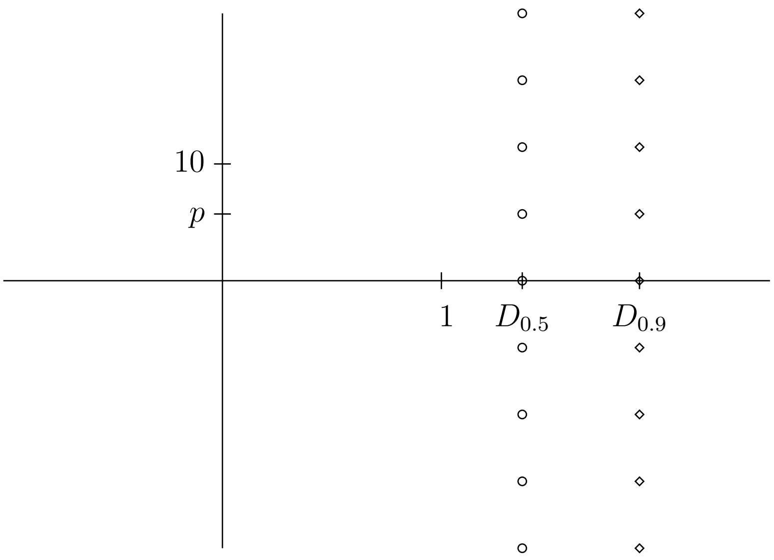

Figure 5.2.: The complex dimensions of ${}_3$MPC with probability $p = 0.9$ ($\diamond$) and probability $p = 0.5$ ($\circ$) are plotted (see Eq. (5.28)). $D_{0.5} = \log_3 4.5$, $D_{0.9} = \log_3 8.1$ and $p = \frac{2\pi}{\ln 3}$.

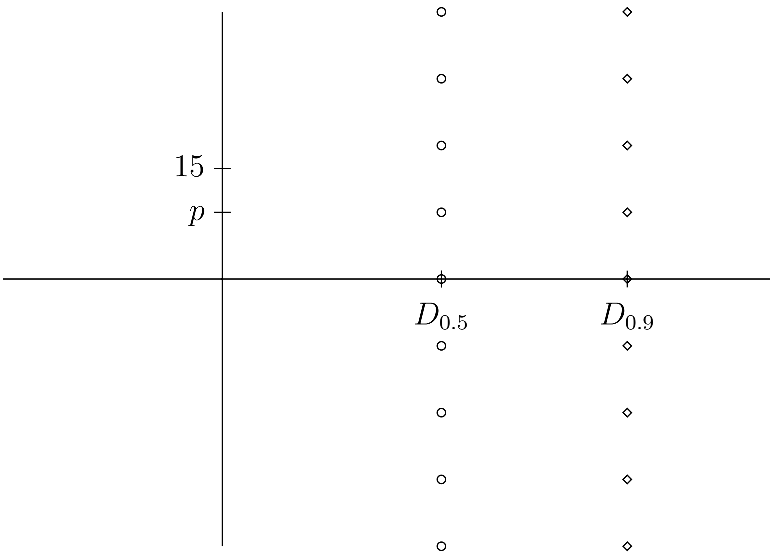

Figure 5.3.: The complex dimensions of ${}_2$MPC with probability $p = 0.9$ ($\diamond$) and probability $p = 0.5$ ($\circ$) are plotted (see Eq. (5.29)). $D_{0.5} = 1$, $D_{0.9} = \log_2 3.6$ and $p = \frac{2\pi}{\ln 2}$.

The probability that the maps ϕ_i $i \in M$ build a certain IFS is

$$P(M,\eta) = p^m(1-p)^{\eta^2-m} \tag{5.25}$$

where $m = |M|$ and p is the probability for every ϕ_i that the interval is mapped. Analogously it yields $P(\overline{M}) = p^{\eta^2-m}(1-p)^m$. With these probabilities one can calculate the mean values

$$\begin{aligned}\mathbb{E}[\sum_{i\in M} r_i^s] &= \eta^2 p \cdot \eta^{-s} \text{ and}\\ \mathbb{E}[\sum_{k\in\overline{M}} g_k^s] &= \eta^2(1-p)\cdot\eta^{-s}.\end{aligned} \tag{5.26}$$

Eq. (5.24) and Eq. (5.26) define the spectral mean zeta function

$$\begin{aligned}\mathbb{E}[\zeta_{3\mathrm{MPC}}](s) &= \frac{9(1-p)\cdot 3^{-s}}{1-9p\cdot 3^{-s}} \text{ and}\\ \mathbb{E}[\zeta_{2\mathrm{MPC}}](s) &= \frac{4(1-p)\cdot 2^{-s}}{1-4p\cdot 2^{-s}}.\end{aligned} \tag{5.27}$$

The complex fractal dimension are

$$D_{3\mathrm{MPC}}(p) = \{\log_3 9p + \mathrm{i}n\frac{2\pi}{\ln 3} : n \in \mathbb{Z}\} \tag{5.28}$$

and

$$D_{2\mathrm{MPC}}(p) = \{\log_2 4p + \mathrm{i}n\frac{2\pi}{\ln 2} : n \in \mathbb{Z}\} \tag{5.29}$$

as plotted in Fig. 5.2 and Fig. 5.3.

5.3. Zeta Functions and Subdimensions

The approach of working with zeta functions has shown that there is a consistency between calculating the fractal dimension of a fractal by $\zeta_{\mathcal{L}}$ and determining the fractal dimension with the Minkowski functionals where D_f first and foremost describes the relation between volume and structure size. The question concerning the subterms is, are the subdimensions also included directly within the zeta function of the fractal?

5.3.1. Spectral Zeta Functions and Subdimensions

Let it be supposed for the moment that the zeta function contains the subdimensions. Therefore, information has to be included either in the oscillatory period or in the spectral zeta function of the motif B. Nevertheless, the spectral zeta function of B is ineligible. If it is responsible for the subdimensions or the dimension differences, all fractals based on the same B would have the same subdimensions or dimension difference, respectively. However, the investigations of the Sierpiński carpet and the Mandelbrot percolation or even of the different Mandelbrot percolation clusters themselves which all are based on a square show that this is not the case. And also the other consideration, the oscillation, can not contain the subdimensions. This can be explained with the differences and the consequent effects of the construction algorithms between the fractal strings and the actual fractals described in chapter 3.1 and 5.1.3 and in chapter 4.1 and 5.2, respectively.

5.3.2. Oscillation and Inversion of Limit Processes

In order to resolve why the oscillations of the iterated and random iterated fractals do not contain the additional information of the Minkowski functionals next to the fractal dimension, the two construction algorithms which are used in this thesis so far have to be compared.

The first algorithm follows a more physical idea. The starting structure I is copied and translated multiple times by characteristic maps of the fractal (see chapter 3.1). For every iterated step the structure gets r-times bigger[1]. This procedure is equivalent to investigating a structure of much higher n within observation windows with suitable, smaller length. An iterated step corresponds to the increase of the window length by the factor r, such that more of the structure is considered. For every iterated step the Minkowski functionals are calculable.

In the other algorithm that is constructed more mathematically the starting structure I is copied and contracted multiple times by characteristic maps of the fractal (see chapter 5.1.3). The size of the structure remains the same for every iterated step. This is done infinitely many times to achieve the fractal set F. As some Minkowski functionals diverge for the fractal set, mathematicians often use the uniform neighbourhood

$$V(\epsilon) = \{x \in \mathbb{R}^d \colon d(x, F) < \epsilon\} \tag{5.30}$$

---

[1] r is the scaling factor.

to characterize the fractal by Minkowski functionals [47]. The functionals are then calculated as functions of ϵ. The equivalent of this algorithm is the investigation of the fractal with a fixed resolution. An iterated step corresponds to the improvement of the resolution, such that contours that are r times smaller than the previous contours which were barely considered become visible.

These two approaches have a crucial difference. For both procedures two limit processes can be identified. The first limit process is the construction of the fractal set itself. The second process is the decrease of ϵ towards 0 for $V(\epsilon)$. Before building the fractal, ϵ is automatically set to 0 for the initiator in the physical approach, such that this limit is performed first. After this, the morphology of the fractal is analyzed in dependence of the iterated steps. As a consequence, the fractal has even for the limit $n = \infty$ a smallest scale defined by the length of the initiator I. In the mathematical approach this order is switched. First, the fractal set is constructed completely with a fixed $\epsilon > 0$. After this, the Minkowski functionals are calculated for decreasing ϵ. There is no smallest scale in contrast to the physical approach for the limit $n = \infty$.

Correctly speaking, the structures which have been calculated by Minkowski functionals so far must not be called fractals but pre-fractals. It concerns some sort of quantization in building the set out of smallest units. Though this quantization has no effect on the fractal dimension, it removes the oscillations. For the pre-fractal the sum in Eq. (5.13) becomes finite. Hence, the discontinuity becomes removable such that no oscillations appear.

As an additional second proof to that, one notices that both fractals have the same oscillation period $p = \frac{2\pi}{\ln 3}$ by investigating the oscillation periods of the Sierpiński carpet and the Menger's sponge. Even though two subdimensions match each other, the number of subdimensions differ. That would mean that the periods contain different amount of information. This is a contradiction.

The question is if our method of building the fractal with smallest units is legitimate? This questions leads to the third type of fractals which are described later in chapter 6. These fractals are natural fractals. The properties of natural fractals are completely random and structures forming in physical phenomena like phase transitions. Here the structure is built out of particles or small objects which determine a smallest scale. From the physical point of view it is necessary to quantize the fractal according to this. To go one step further, one can even say that the subdimensional terms only occur as quantization effects. However, the dimensions and amplitudes are universal for a specific fractal. While the subdimensions are not dependent of the size of the smallest element, the size is the only degree of freedom of the amplitudes.

5.4. Boundary Effects of the Observation Window

In the last section of chapter 5 geometric and spectral zeta functions of fractal strings were introduced. We investigated oscillatory periods in the dimension of fractals but could prove that these oscillations do not occur for the used prefractals. Hence, another approach to find the information behind the subdimensional terms is needed. A crucial hint is provided by the subdimension of the Menger's sponge. The calculations in Eq. (3.13) revealed that the surface fractal subdimension is $d_{1,\text{Menger}} = \log_3 8$. This is also the fractal dimension of the Sierpiński carpet (see Eq. (3.9)). Of course, this could be a coincidence. But because the Menger's sponge is the three dimensional analogous to the Sierpiński carpet, let us investigate the Menger's sponge a little further.

Consider the Menger's sponge being built with the method of chapter 3.1. For every iterated step n the fractal F_n is observed within the observation box $W^{[n]}$. To calculate the fractal dimension the structure $F_n \cap W^{[n]}$ is considered. A possible way to construct the carpet of the n-th iterated step out of F_n is to observe the intersection $F_n \cap \partial W^{[n]}$ between the Menger's sponge and the boundary faces of $W^{[n]}$. One reduces the investigated structure to the next smallest topological dimension hereby. At all six faces of the box the motif of the Sierpiński carpet after n steps emerges (see Fig. 5.4). Consequently, this intersection scales like the Sierpiński carpet with the fractal dimension $d_{\text{Sierp}} = d_{F\cap\partial W} = \log_3 8$ due to the zeta function of Eq. (5.15). This zeta function is called *face zeta function* of the Menger's sponge $\zeta_f(s)$.

The topological dimension is repeatedly lowered to find structures which have a fractal dimension equal to the mean curvature fractal subdimension $d_{2,\text{Menger}} = 1$ and the Gaussian curvature fractal subdimension $d_{3,\text{Menger}} = 0$. First, the intersection $F_n \cap \partial^2 W^{[n]}$ between F_n and the frame of the observation box is considered. The intersection with the frame of the box yields in this case the box frame again. The zeta function is called the *edge zeta function* of the Menger's sponge $\zeta_e(s)$. Because the intersection has no holes, the edge zeta function of this structure is the Riemann zeta function (see Eq. (5.5)). The function converges for every $k > 1 = \sigma$. This abscissa of convergence σ can be identified as the fractal dimension of the observation window frame $d_{F\cap\partial^2 W} = \sigma = 1$.

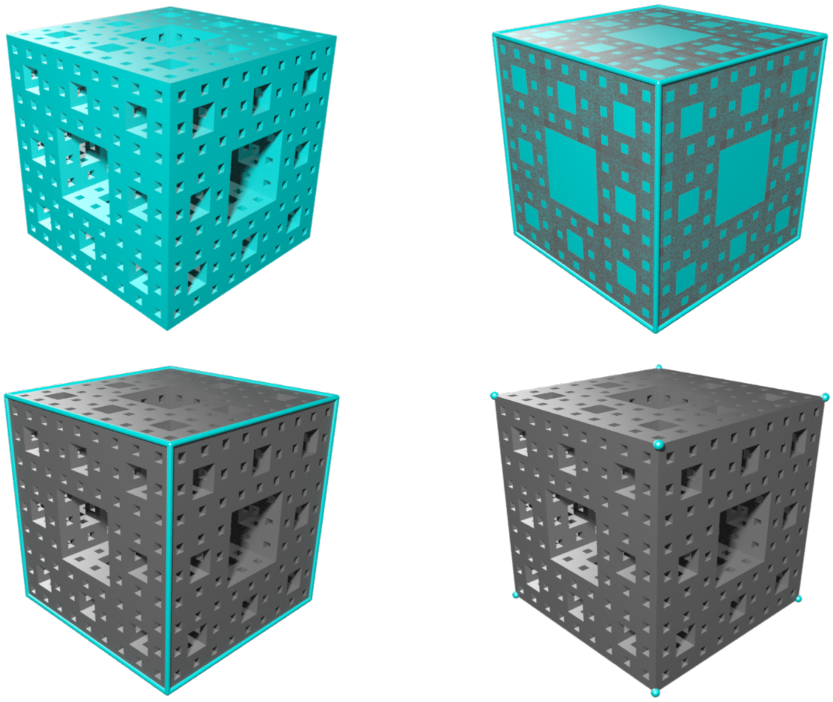

Figure 5.4.: This figure sketches the approach how to obtain the subdimension and resolves their appearance using the example of the Menger's sponge. In the top lefthand corner, the whole fractal (blue) is considered to calculate the fractal dimension. In the top righthand corner, the intersection between the observation window boundary faces (blue) and the fractal is observed. The fractal dimension of the emerging structure, the Sierpiński carpet, is equal to the surface subdimension of the fractal. In the bottom lefthand corner, the intersection between the observation window frame (blue) and the Menger's sponge is taken into account. The fractal dimension of the emerging structure is equal to the mean curvature subdimension of the fractal. In the bottom righthand corner, the intersection between the observation window vertices (blue) and the fractal is considered. The fractal dimension of the emerging structure is equal to the Gaussian curvature subdimension of the fractal.

To reduce the topological dimension further, the intersection with the vertices of the box are considered. Because this is a set of single points, the zeta function is not defined. However, F_n is defined on all eight vertices of the box for every iterated step. The number of points which are formed by the intersection stays constant. The fractal dimension is 0. For the Sierpiński carpet we can proceed similar and see that the subdimensions coincide with the fractal dimensions of the structure on the observation window edges and vertices, respectively. The procedure is sketched in Fig 5.4.

To verify the just obtained results, the fractal dimensions of the intersection of the random iterated fractals and the rim of the observation window have to be calculated. First, the edge zeta function of ${}_2$MPC is considered.

The initiator set is an interval on $\mathbb{R}$. Two functions ψ_1 and ψ_2 which divide the fractal into two pieces ($r_1 = r_2 = \frac{1}{2}$) are defined. The mapping probability of ψ_i is the same probability p of mapping the unit square with ϕ_i. The mean values are $\mathbb{E}[\sum r_i^s] = 2p \cdot 2^{-s}$ and $\mathbb{E}[\sum g_i^s] = 2(1-p) \cdot 2^{-s}$. The mean edge zeta function is

$$\mathbb{E}[\zeta_e](s) = \frac{2(1-p) \cdot 2^{-s}}{1 - 2p \cdot 2^{-s}}. \tag{5.31}$$

The fractal dimension is $D_f = \log_2 2p$. However, this dimension differs from the fractal surface dimension $d_{1,\mathrm{MPC}} = \log_2 2p^2$ which was calculated in Appendix C and listed in Table 4.3. The procedure has to be modified already in this case.

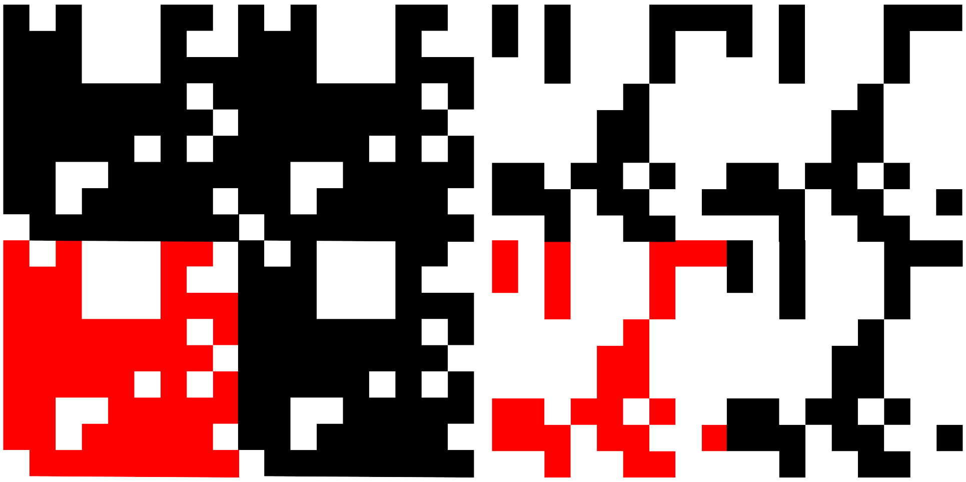

Figure 5.5.: The ${}_3$MPC with $p = 0.8$ on the lefthand side and $p = 0.5$ on the righthand side is depicted. To calculate the subdimensions , it is assumed that the fractals within the observation window (red) have periodic boundary conditions (black). Only the edges and vertices of the fractal which are touching the neighboring MPC are taken into account.

The missing factor p within the logarithm can be explained by taking periodic boundary conditions into account. The structure is then defined as intersecting the frame of the observation window at a certain point P if the structure touches the frame at point P from inside as well as from the outside of the observation window as depicted in Fig. 5.5. With this change of the definition of intersecting the widow frame, the probability of mapping with ψ_i changes to p^2, the edge zeta function to

$$\mathbb{E}[\zeta_e](s) = \frac{2(1-p^2)\cdot 2^{-s}}{1-2p^2\cdot 2^{-s}}, \tag{5.32}$$

and the fractal dimension to the expected value $D_f = \log_2 2p^2$ (see Fig. 5.6). By checking the vertices of the observation window, the anticipated curvature subdimension is calculated. The vertex P is defined as intersected if P is touched by the structure from all 4 quadrants. The probability that the vertex is mapped is p^4. As for the Sierpińskt carpet a zeta function out of the set of single points can not be determined. However, as the mean number of vertices after n iterated step is $4\cdot(p^4)^n$ and the window increases every time by the factor 2, one can argue that the fractal dimension is $D_f = \log_2 p^4$. The analogue calculations for $_3$MPC yield the edge zeta function

$$\mathbb{E}[\zeta_e](s) = \frac{3(1-p^2)\cdot 3^{-s}}{1-3p^2\cdot 3^{-s}}, \tag{5.33}$$

the edge fractal dimension $D_f = \log_3 3p^2$ (see Fig. 5.7), and the vertex fractal dimension $D_f = \log_3 p^4$. With this small modification the fractal dimensions at the edges of the Sierpiński carpet and Menger's sponge do not change because with periodic boundary conditions the faces, edges, and vertices are always intersected from all sides. In a nutshell, the subdimensions of a fractal can be affiliated to fractals with lower topological dimension which are hidden within the fractal. These fractals are the results of the intersection between the structure and the boundaries of the observation window.

5.5. Subtermal Amplitudes

After the subdimensions were reproduced by geometric properties, the effort on the amplitudes is intensified. However, this is difficult to do for both iterated fractals because one has no structure of comparison for the two and three dimensional structures. This does not hold for MPC. The two different structures $_2$MPC and $_3$MPC can be generated with different probabilities. This is why their amplitudes are considered (see Table 4.2 and Table 4.3). Here two issues become apparent. The first issue appears for $W_1^{2,0}$ and $W_2^{2,0}$ of both structures. These two Minkowski tensors are not defined for all probabilities. The tensors diverge at $p = \frac{1}{2}$ for $_2$MPC

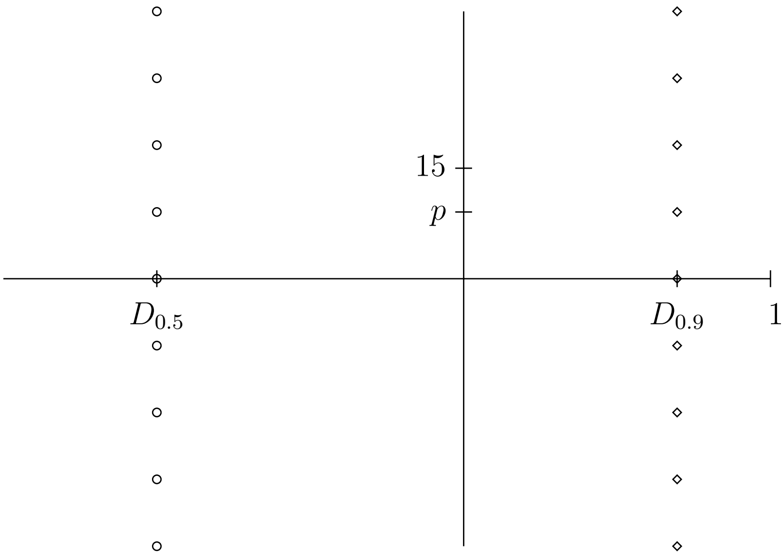

Figure 5.6.: The complex edge dimensions of ${}_2$MPC with probability $p = 0.9$ ($\diamond$) and probability $p = 0.5$ ($\circ$) are plotted (see Eq. (5.32)). $D_{0.5} = \log_2 0.5$, $D_{0.9} = \log_2 1.62$ and $p = \frac{2\pi}{\ln 2}$.

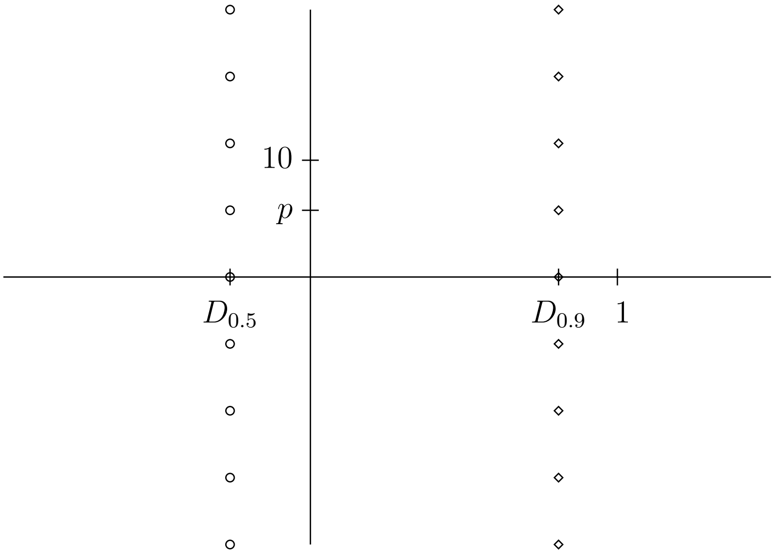

Figure 5.7.: The complex edge dimensions of ${}_3$MPC with probability $p = 0.9$ ($\diamond$) and probability $p = 0.5$ ($\circ$) are plotted (see Eq. (5.33)). $D_{0.5} = \log_3 0.75$, $D_{0.9} = \log_3 2.43$ and $p = \frac{2\pi}{\ln 3}$.

and $p = \frac{1}{3}$ for ${}_3$MPC. This happens exactly when the subdimension $\log_2 8p^2$ and $\log_3 27p^2$ become equal to the fractal dimension $\log_2 4p$ and $\log_3 9p$. These two probabilities can be identified as the critical transition threshold $p_{II \to V}$ between the dust and the cluster phases which already have been calculated in chapter 4.2.3. That is also the reason why $W_1^{2,0}$ and $W_2^{2,0}$ are not plotted with $p = 0.5$ in Fig. 4.9. This raises the possibility that also the other transition points are determinable out of the amplitudes. However, apart from the mentioned discontinuity there is no other one between 0 and 1. So the probabilities have to be determined in other ways. Particularly conspicuous is the change of the sign of the fractal amplitude for W_2 and $W_2^{2,0}$. Here we concentrate just on ${}_2$MPC. This sign change happens exactly at

$$0 = 2 - 3p_1 + p_1^4$$
$$0 = 64 - 32p_2 - 32p_2^2 - 31p_2^3 + p_2^4.$$

The two different, distinguished probabilities are $p_1 \approx 0.811$ and $p_2 \approx 0.817$. However, these two can not be identified with p_c. Firstly, they lie just outside the calculated boundaries (see Eq. (4.16)) and secondly, they do not match with the numerical calculations which are shown in chapter 4.2.3. Furthermore, one can evaluate p at the second sign change of the amplitude of $W_2^{2,0}$ which results in $p_3 \approx 0.802$ from

$$0 = 8 - 4p_3 + 2p_3^2 - 11p_3^3 - p_3^4.$$

However, this one is not even within the boundaries. The same yields for ${}_3$MPC.

At further investigations, the assumption that the critical point is contained in the amplitudes can be precluded. In order to do this one has to consider that the Minkowski functionals not only describe the Mandelbrot percolation cluster but also the general random carpet. If the amplitudes include information of the percolation transition, the critical point of both structures had to be the same. However, in chapter 4.2.3 it is discussed that the critical point of ${}_2$GRCs with different types do not match. Consequently, the amplitudes are not described by p_c.

If p_1, p_2, and p_3 do not determine percolation, how does the structure changes at the point round about $p \approx 0.81$? The structure changes from a set which is dominated by many single clusters to a set which has less clusters with many holes. It means that the clusters get so large that they merge and create more holes than single clusters. This can be interpreted as an additional phase between phase V and VI (see Fig. 5.8).

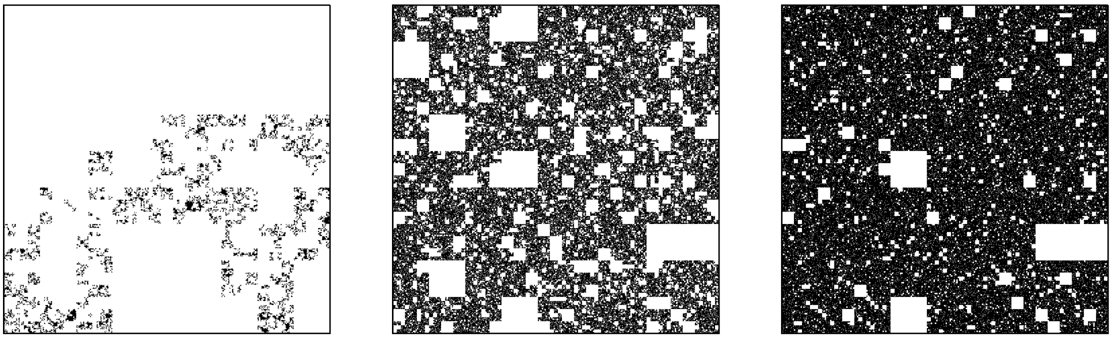

Figure 5.8.: The ${}_3$MPC with different probabilities is depicteded. On the lefthand side the probability is $p = 0.6$. It consist out of many separated clusters. The MPC in the middle has the probability $p = 0.88$. It has a few structures with many holes. The last MPC is built out of one single cluster and thus percolates. The probability is $p = 0.95$.

From this example it becomes apparent that the subdimensions and subdmensional amplitudes do contain structural information. More precisely the behavior at the boundaries of the observation windows and some phase transition points can be derived from the subdimensions and its amplitudes. However, it can be argued that more interesting properties like the percolation threshold is not determined by them. In the next chapter this knowledge is adapted to random fractals and therefore, to physical structures.

6. Random Fractals

The third type of fractals which are covered in the following chapter is the *random fractals*. In contrast to the structures which have been described so far the random fractals can not be built by iterated steps of mapping sets or represented by such a set. Typically these macro-sized structures come into existence at physical processes through the interaction and self-organization of micro-sized particles. The two fractals discussed in this thesis are very well studied structures. The first fractals are the diffusion limited aggregation clusters in two and three dimensions. After this, percolation clusters are considered.

6.1. Diffusion Limited Aggregation in 2D

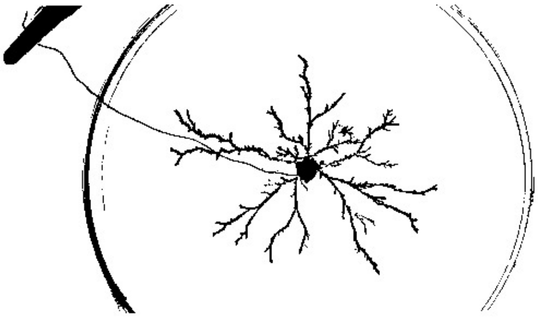

Figure 6.1.: A DLA structure is formed by the electrolysis of $CuSO_4$.[1]

The first representative of a random fractal in this thesis is a structure known as the *diffusion limited aggregation* (DLA) clusters. These kind of fractals were first described in 1981 by T. A. Witten and L. M. Sander [48]. In nature DLAs are emerging often in processes where the behavior of small single particles is dominated by diffusion. This means they move under Brownian motion in a dilute medium from a distance which can be seen as from infinity and stick together when in contact. In the growing process the particles form characteristic branches which prevent the remaining single particles from getting deep into the center of the structure. A standard example where this fractal occurs is the electrolysis of copper sulfate ($CuSO_4$) (see Fig. 6.1). Since their discovery, DLAs have been studied intensively

---

[1] http://classes.yale.edu/fractals/panorama/physics/dla/Electrodeposition/Electrodeposition.html

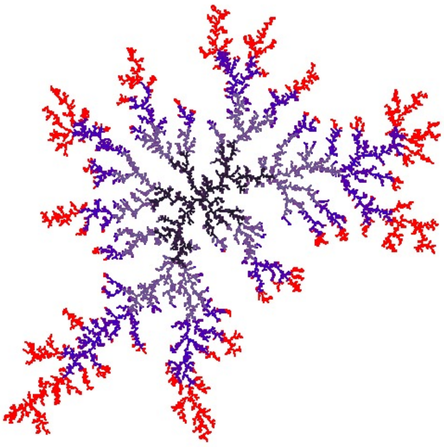

Figure 6.2.: This picture shows the growth process of a DLA cluster which is built with the Witten and Sander algorithm after 1,000 (black), 3,300 (grey), 6,600 (blue), and 10,000 (red) particles.

being stochastic, random, and spontaneously created structures which can be constructed with great numbers of particles $n > 10^7$. Numerical calculations determined the fractal dimension very close to 1.71 in two dimension [49]. To analyze the subdimensions, a method is used to construct DLA-clusters which is explained in the following section.

6.1.1. Construction

The first DLA cluster is constructed in two dimensions in the way introduced by Witten and Sander [48]: In this method the DLA is generated on a lattice with its particles sitting on the lattice points. It is very important that the grid is large enough, otherwise the borders influence the growth process. The progress begins with a single particle fixed in the center. Every particle is represented by a 1×1 square. After the foundation is set, a second particle is produced randomly somewhere on a circle around the cluster center. The radius r_{start} has to be large enough that the particle is not touching the cluster. The particle then moves by a random-walk (no diagonal steps) due to Brownian motion on the lattice until at least one vertex is touching the cluster. It is then fixed on this spot on the lattice and the next particle is created in the same way. If the particle walks in the wrong direction away from the cluster and is too far away, the particle is removed and a new one is produced on the starting circle. For the distance r_{kill} at which the particle is removed $r_{kill} > r_{start}$ holds. This reduces the running time of the simulation. A second implementation to increase efficiency is a special jumping

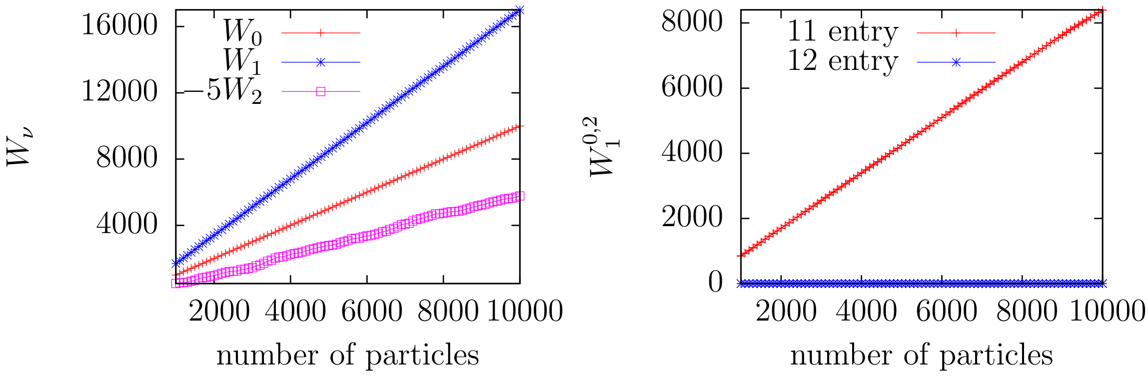

Figure 6.3.: The progressions of the Minkowski scalars and $W_1^{0,2}$ during the process of growth of a two dimensional DLA-cluster are shown. The final number of particles is 10,000.

area. If the particle is located further away from the lattice center than r_{jump} with $r_{kill} > r_{jump} > r_{start}$, the particle moves not under random-walk anymore. It now jumps to a random spot on the circle around its temporary position with the radius $r - r_{start}$. This does not change the random-walk character because the possibility for the particle to reach a point on the circle by random-walk is distributed uniformly. As the particles are discretized on the lattice, the minimum radius $r_{jump} - r_{start}$ has to be at least 10 to minimize errors. All three radii r_{kill}, r_{jump}, and r_{start} have to grow with the cluster as well, such that the cluster never intersects one of the circles.

This process continues until all n particles are connected and the cluster is constructed. It is then possible to calculate the Minkowski functionals of the whole DLA with Papaya. For the calculations, the origin of the coordinate system is set as the center of the lattice.

6.1.2. Construction test

To test the DLA construction program and the conversion to a Papaya-readable file and to get a first impression about the Minkowski functionals of DLAs, a DLA with 10,000 particles is constructed. In Fig. 6.2 one can see its growth. After every 100th particle the Minkowski functionals are calculated for the whole structure (see Fig. 6.3). The graphs show that the cluster is constructed correctly. Especially W_0 shows the behavior as expected. W_0 is always equal to the number of particles n. The graph of W_1 also implies that it is constructed correctly. In the first approximation one gets a straight line with a slope of 1.7. For every new particle the increase of the circumference is either +2 if the new particle shares an edge with an other particle of the cluster or +4 if the new particle only shares one vertex with another particle. Thus the slope has to be between 1 and 2. Because it is more likely that the particle is sticking diagonal to the other one – for the random-walk used in this thesis there are two ways to get to a diagonal position in the cluster and one way to get to a directly neighboring position – 1.7 is reasonable. However, there is no literature value for this scaling. W_2 displays a strictly monotonically decreasing behavior which shows that only holes are occurring with increasing number of particles. However, the fractal is never divided into multiple clusters which would cause an increase of the Euler characteristic. Not only the Minkowski scalars show that the DLA is constructed correctly, also the tensors especially the off-diagonal entries of $W_1^{0,2}$ strengthen the validity of the constructed DLAs. For every number of particles $W_1^{0,2}$ is diagonal. This results from the fact that the cluster is built out of squares. The normal vector is either pointing parallel to the x-axis or parallel to the y-axis. According to Eq. (2.3) the off-diagonal entries of $W_1^{0,2}$ become 0 for every edge and as a result for the whole DLA. Additionally to that, $\mathrm{Tr}[W_1^{0,2}]$ is equal to W_1 for the very same reason. Consequently, $\mathrm{Tr}[W_1^{0,2}]$ has not to be considered further.

6.1.3. DLA Minkowski Functionals

For better investigation of the DLA, larger clusters containing 100,000 particles are generated. To calculate the mean Minkowski functionals 1,000 different DLAs are constructed. The Minkowski functionals are now computed within observation windows according to the extended Minkowski density method, explained in chapter 2.3.2. The smallest window has a side length of 20, the largest a length of 1,900. The side length is increased in steps of 20. The result of W_0 is plotted in Fig. 6.4. The graph is composed of two regions. In the first region the observation windows are small and the data shows a straight line which indicates that the behavior of the functional depends on Eq. (2.16). There are no boundary effects. In the second region the window is getting larger, such that the effect of saturation slowly eventuate. There is actually also a third region which shows a plateau where the functionals do not change anymore. In this region the observation windows are even larger. This is the saturation range where the number of particles included in the window does not increase anymore by increasing the window size. However, this region is not reached at an observation window length of 1,900. The fractal dimension d_f can be calculated in region I. This region contains all data with $x < 1,200$. The data with larger x are not taken into account for further calculations. The slope indicates that the fractal dimension of the 1,000 DLAs is $d_f \approx 1.70$. The dimension is similar to the actual fractal dimension of a two dimensional DLA [49]. In Fig. 6.4 also the other Minkowski scalars and tensors are

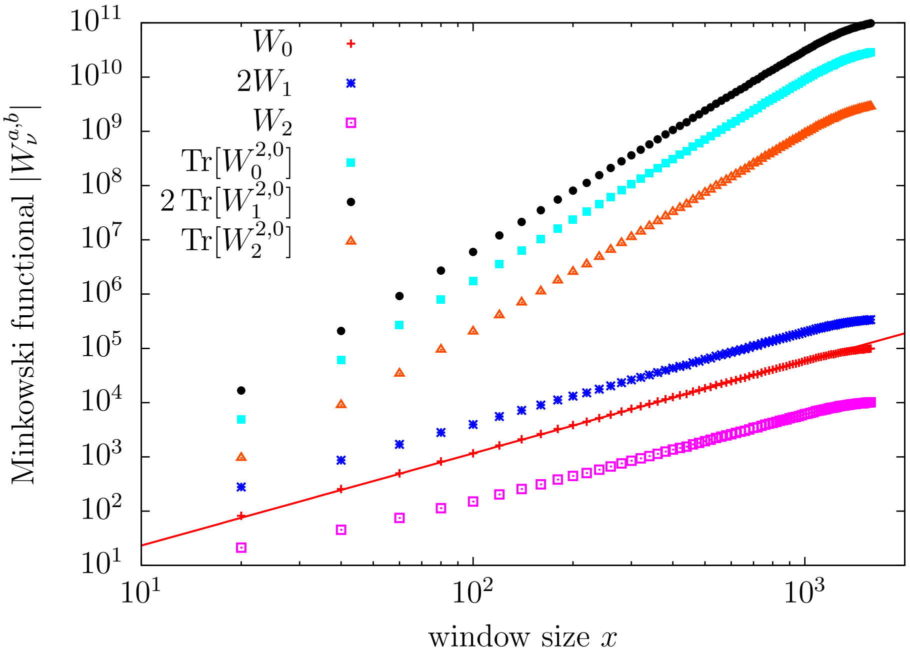

Figure 6.4.: The progression of the mean Minkowski functioals of 1,000 two dimensional DLA clusters due to the observation window size is plotted. The DLAs consist out of 100,000 particles.

shown. As in the case of the Sierpiński carpet the functionals $W_\nu^{a,b}$ are primarily determined by the dominant fractal term.

To see potential subdimensions of the functionals, the data which is modified in the way described in chapter 2.3.2 is plotted first (see Fig. 6.5). It turns out that the subdimensions are observed (see Tabular 6.1) even by examining DLA clusters with a small amount of particles ($n \leq 10^6$) . The calculated slopes are $\Delta_1 d_{W_1} \approx -1.028$ and $\Delta_1 d_{W_2} \approx -1.022$ for the Minkowski scalars. $\Delta_1 d_{W_1}$ is close to identical with $\Delta_1 d_{W_2}$, such that one can argue that this is in good accordance to Eq. (3.11) – at least for the scalars – where the fractal surface term is subdominant for both W_1 and W_2. The fractal surface subdimension is close to -1. This result would correspond to the hipothesis from the hypothesis postulated in chapter 3.2.

Now the rank-2 tensors are investigated. As for the other structures the trace of each tensor is examined. The results are also shown in Fig. 6.5. However, it is difficult to obtain slopes out of the data. Especially $W_0^{2,0}$ and $W_1^{2,0}$ are difficult to analyze. For both functionals the region where the data straightens the slope is calculated narrows down to between 150 and 600. Nevertheless, at this range the

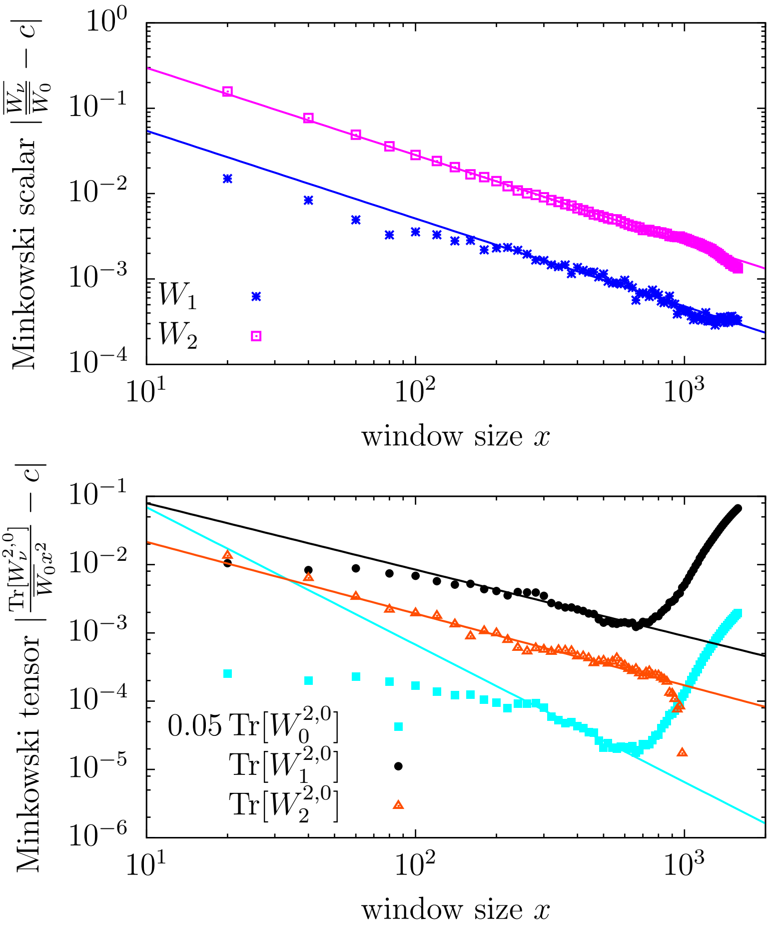

Figure 6.5.: The mean Minkowski functioals of 1,000 two dimensional DLA clusters due to the observation window size is plotted. The DLAs consist out of 100,000 particles. The data is modified in the way described in chapter 2.3.2. c and Δd can be seen in Table 6.1.

calculated dimension difference are close to the expected values $\Delta_3 d_{W_0^{2,0}} \approx -2$ and $\Delta_1 d_{W_1^{2,0}} \approx -1$ (see Table 6.1). At least for $W_2^{2,0}$ the slopes are more distinct. The range is between 100 and 900. The dimension difference $\Delta_1 d_{W_2^{2,0}}$ is close to -1. In general, the DLA exhibits the same behavior as the iterated and random iterated fractals.

However, this approach to calculate the subdimensions turns out to be unsatisfying. Firstly, it is hard to determine the constants c which has to be subtracted correctly. This causes an error. Secondly, the signal of the data is so small that

functional $W_\nu^{a,b}$	constant c	slope $\Delta_1 d$	first subdimension d_1
W_1	1.707	-1.028±0.082	0.672±0.082
W_2	-0.101	-1.022±0.006	0.678±0.006
$\mathrm{Tr}[W_0^{2,0}]$	0.1548	-2.012±0.122	1.688±0.122
$\mathrm{Tr}[W_1^{2,0}]$	0.2648	-0.973±0.062	2.727±0.062
$\mathrm{Tr}[W_2^{2,0}]$	0.0157	-1.050±0.033	2.650±0.033

Table 6.1.: The mean values of the subtracted constants, slopes, and calculated subdimensions for 1,000 two dimensional DLAs with 100,000 particles built with the Witten and Sander algorithm are listed which are obtained from Fig. 6.5. The fractal dimension is $d_f \approx 1.70$.

the noise is high in comparison. And thirdly, the curvature terms can not be calculated if the subdominant term is the surface term without increasing the errors even further.

6.1.4. Boundary fractals

Because there was not much success with the first approach to calculate all subdimensions, another method is used. According to chapter 5.4 the subdimensions are the fractal dimensions of the structures which occur at the intersection between

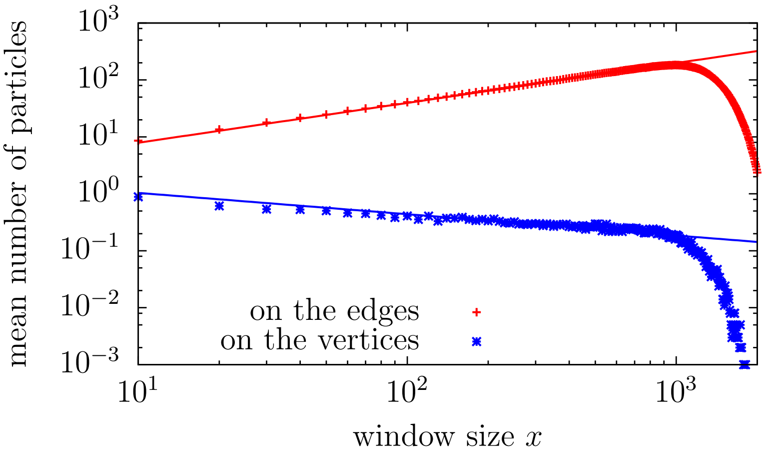

Figure 6.6.: The mean number of particles on the edges and vertices of the observation window of 1,000 two dimensional DLA clusters due to the observation window size is plotted. The DLAs consist out of 100,000 particles.

the fractal and the rim of the observation window. To calculate the fractal dimension of the fractal at the observation window edge for every observation window size, the particles on the edge are counted. The result is plotted in Fig. 6.6. The calculated fractal dimension is $d_1 \approx 0.70$. The difference to the fractal dimension is $\Delta_1 d \approx -1.00$. This result is in good agreement with the results of the Sandbox method above. The curvature subdimension is also calculated by counting the number of particles at the vertex of the observation window (see Fig. 6.6). The slope gives the fractal dimension $d_2 \approx -0.302$. The difference is $\Delta_2 d \approx -2.002$. The results indicate that a rule is found to determine the subdimensions. For the hidden fractals living on the ν-th smaller topological dimension the fractal dimension $\tilde{d_f}$ is as conjectured

$$\tilde{d_f} = d_\nu = d_f - \nu. \tag{6.1}$$

As discussed in chapter 5.4 one has to be careful to use periodic boundary conditions. This consideration can be circumvented. The observation windows are chosen, such that their boundaries divide the particles on the edge in half. Therefore, the observation window is intersected form both sides.

To calculate the amplitudes the data is fitted with the functions of Eq. (3.11)

ν	0	1	2	3
d_ν	1.70	0.70	-0.30	$d_0 - 2$
$w_{0;\nu}$	0.663 ± 0.050	–	–	–
$w_{1;\nu}$	1.129 ± 0.085	-0.325 ± 0.011	–	–
$w_{2;\nu}$	-0.087 ± 0.006	-1.691 ± 0.175	??	–
$w_{0;\nu}^{2,0}$	0.096 ± 0.018	–	–	??
$w_{1;\nu}^{0,2}$	1.129 ± 0.085	-0.325 ± 0.011	–	–
$w_{1;\nu}^{2,0}$	0.187 ± 0.016	-0.605 ± 0.204	–	??
$w_{2;\nu}^{2,0}$	-0.010 ± 0.001	0.141 ± 0.051	??	!!$_2$

Table 6.2.: This table determines the mean Minkowski functionals of 1,000 two dimensional DLAs with 100,000 particles up to the rank-2 tensors (see Eq. (3.11)). The fractal dimension, the subdimensions, and the corresponding fractal amplitudes are listed. The sign "??" means that the standard deviation is too large, such that the information is not useful. The sign "!!" is intended to call attention that the term of this amplitude has the same exponent as one of the terms before. The index shows to which term this applies.

using $d_f = 1.7$. However, one has to be careful when fitting $W_2^{2,0}$. This tensor has three additional terms next to the fractal term. However, on closer examination one notices that the curvature term and the unmodified fractal term have the same exponent due to Eq. (6.1). Hence, these two terms are merged.

Not all of the amplitudes can be fitted reasonably. Though all of them can be calculated by fitting, the noise is too high to provide any informations about the second and higher subdimensional amplitudes, nevertheless. As a consequence, these amplitudes are not listed in Table 6.2.

6.2. Diffusion Limited Aggregation in 3D

6.2.1. Construction

The three dimensional DLA cluster is built analogous to the Witten and Sander Model in two dimensions with a few differences. First, a three dimensional lattice is constructed. To avoid any disturbance of the borders of the lattice, the lattice has to be chosen large enough. As in two dimensions the first fixed particle is centered in the middle of the grid. The other particles are created with an uniformly distributed probability on a random spot on a spherical surface around the cluster and move by a random walk until they touch the cluster. As in two dimensions the particles can not walk diagonally within the lattice. However, this time the walking particle is defined as sticking to the cluster if it shares a face or an edge with another particle. The reason is Bilimbi has to be used instead of Karambola. Karambola has the disadvantage that it can not calculate the system if a particle

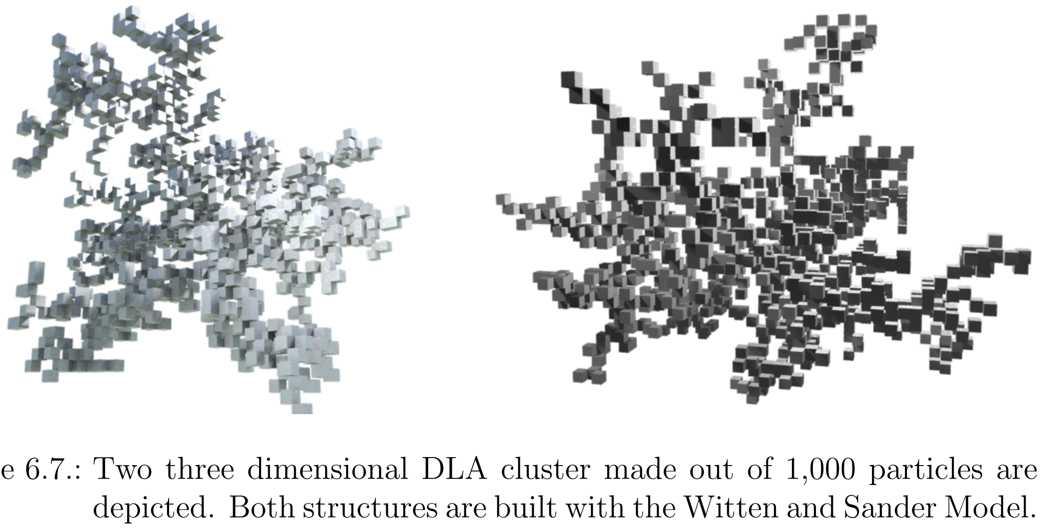

Figure 6.7.: Two three dimensional DLA cluster made out of 1,000 particles are depicted. Both structures are built with the Witten and Sander Model.

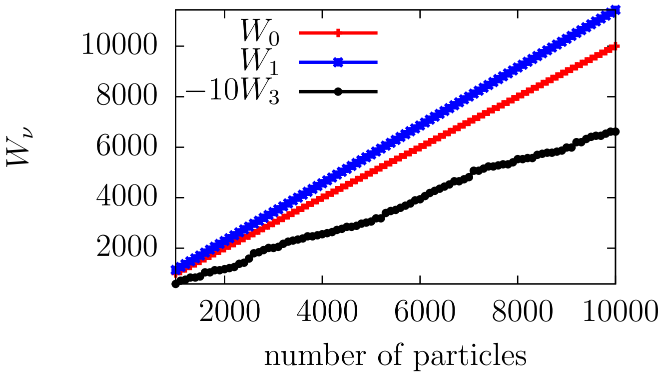

Figure 6.8.: The progression of the Minkowski scalars during the process of growth of a three dimensional DLA cluster is depicted. Its final number of particles is 10,000.

just shares an edge or a vertex with the rest of the structure. However, Bilimbi can use data with critical edges. As already explained Bilimbi calculates the Minkowski functionals with the marching cubes algorithm which prevents the possibility to build a DLA cluster with particles only linked by a single vertex. The features described in chapter 6.1.1 to speed up the simulations by removing the particle from the distance r_{kill} and letting the particle jump instead of walk from the distance r_{jump} are also implemented here. Two representative structures which are constructed with this method are depicted in Fig. 6.7.

6.2.2. Construction test

As a testing calculation a 3D DLA cluster containing 10,000 particles is generated. After every 100th particle, the Minkowski scalars are calculated (see Fig. 6.8). The expected behavior is appearing for the scalars. W_0 is proportional to the number of particles of the cluster. W_1 is again a straight line with slope 1.14 which also agrees with the borders of increase of the surface. W_3 is strictly monotonously decreasing which indicates rings in three dimensions and no multiple clusters.

6.2.3. DLA Minkowski functionals

The DLA clusters which are constructed to calculate the Minkowski functionals contain 1,000,000 particles. As in two dimensions 1,000 of these clusters are built. The observation boxes varied between 10 and 800 in size. However, only within the region I between 100 to 370 one can calculate the dimensions (see Fig. 6.9). The determination of the fractal dimension yields $d_f = 2.41$. The fractal dimension

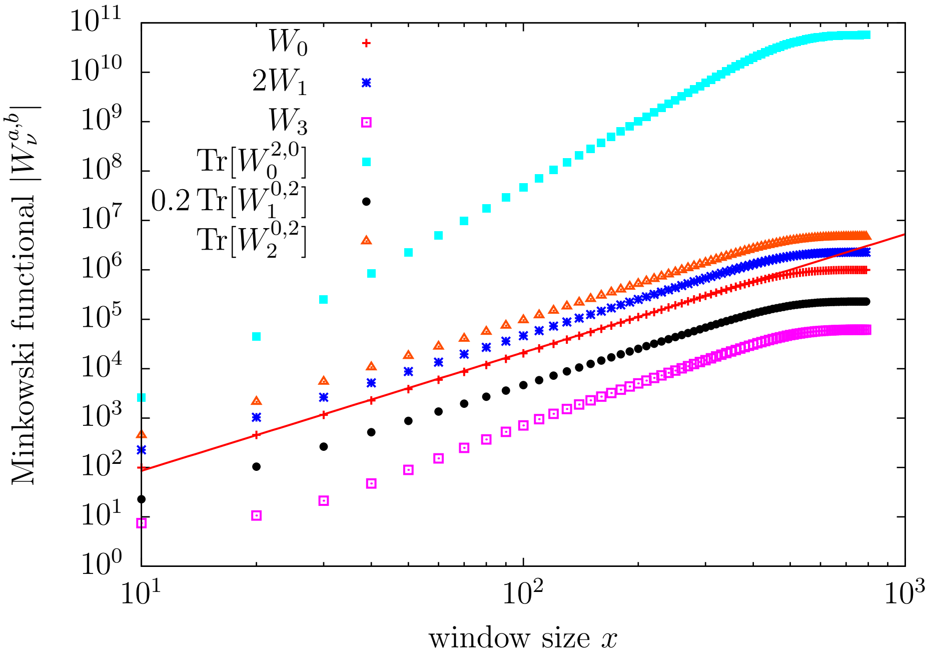

Figure 6.9.: The progression of the mean Minkowski functionals of 1,000 three dimensional DLA clusters due to the observation window size is plotted. The DLAs consist out of 1,000,000 particles.

determined in the latest numerical calculations is $d_{f,\mathrm{lit}} = 2.5$ [50]. However, the difference can be explained. For the calculation in Ref. [50] an off-lattice method is used. Different from this algorithm, the particles only occupy the space on a lattice point in the algorithm in chapter 6.2.1. Intermediate states are not possible. This kind of restraint causes a smaller dimension. This effect also occurs

functional $W_\nu^{a,b}$	constant c	slope $\Delta_1 d$	first subdimension d_1
W_1	1.1422	-0.985±0.024	1.425±0.024
W_3	0.0581	-0.981±0.024	1.429±0.024
$\mathrm{Tr}[W_0^{2,0}]$	0.200	–	–
$\mathrm{Tr}[W_1^{0,2}]$	1.1422	-0..985±0.024	1.425±0.024
$\mathrm{Tr}[W_2^{0,2}]$	3.1298	-0.974±0.027	1.526±0.027

Table 6.3.: The mean values of the subtracted constants, slopes, and calculated subdimensions for 1,000 three dimensional DLAs with 1,000,000 particles built with the Witten and Sander algorithm are listed which are obtained from Fig. 6.10. The fractal dimension is $d_f \approx 2.41$.

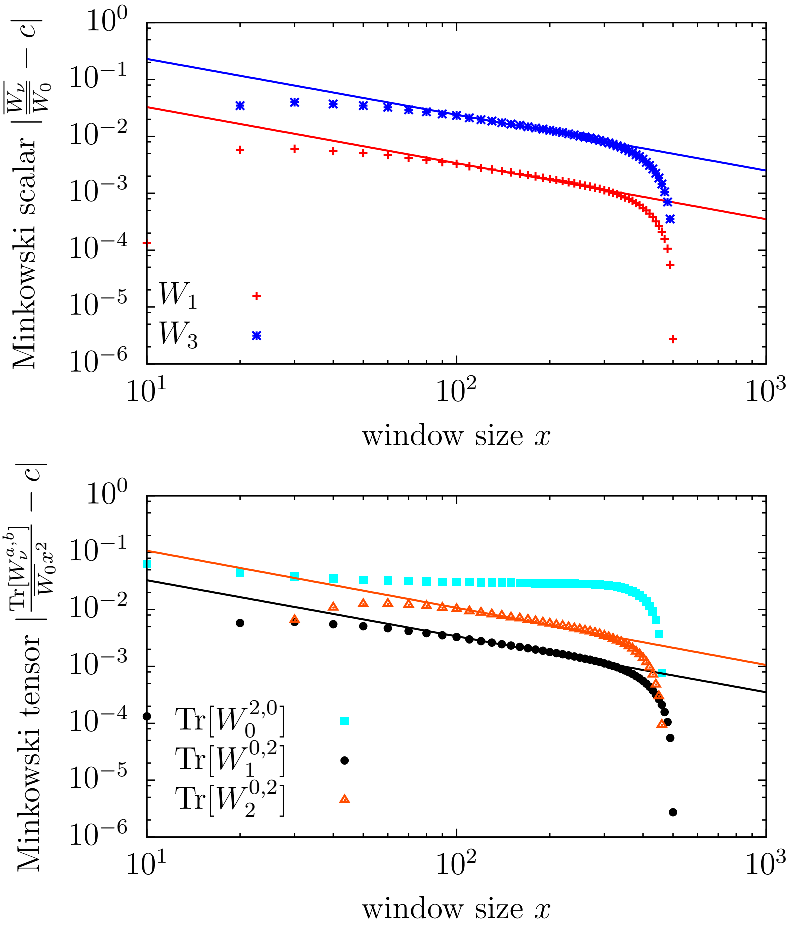

Figure 6.10.: The mean Minkowski functionals of 1,000 three dimensional DLA clusters due to the observation window size is plotted. The DLAs consist out of 1,000,000 particles. The data is modified in the way described in chapter 2.3.2. c and Δd can be seen in Table 6.3.

in two dimensions. However, the possibility of particles also touching just at a vertex reduces the effect in this case. The off-latice method is not used because it is costlier in simulation time to voxelize the DLA cluster. Also for the other functionals the fractal term is dominant as one can see in Fig. 6.9 considering the addition of 2 for $W_0^{2,0}$ again (see Eq. (2.4)).

The first way to make the subdimensions observable is the modified Sandbox method. The data is plotted in Fig. 6.10 and the fit parameters are listed in Table 6.3. The calculated dimensions show similarity to the calculations in two dimensions. The difference between the fractal dimension and the second term exponent of W_1 and W_3 is close to -1. As examined in two dimensions the contour and the Gaussian curvature have a subdominant fractal surface term which is close to the hypothesis in chapter 3.2. The tensors $W_1^{0,2}$ and $W_2^{0,2}$ have the subdimension $d_1 = d_f - 1$ as well. All of these examinations are in good correspondence with the previous results. The only functional for which no subdimension can be calculated is $W_0^{2,0}$. The problem is again the determination of the subtracting constant c. This is due to the fact that the subterm has a small amplitude close to 0. Consequently, the results of the Sandbox method point to the validity of Eq. (3.15) for the three dimensional DLA as well. To get better results and also the hidden dimensions, the boundary fractals of the structure are considered.

6.2.4. Boundary Fractals

The first boundary fractal set is the intersection between the DLA and the boundary faces of the observation windows. As in the case of the Sandbox method for every observation window size between 10 and 800 the number of particles on the faces are counted. The data is plotted in Fig. 6.11. The fractal dimension of the structure is $d_{f,\text{face}} = 1.400 \pm 0.009$. By also comparing this to the results of the Sandbox method, one notices that the surface subdimension is indeed equal to $d_1 = d_f - 1$.

The next fractal set is the intersection between the observation box frame and

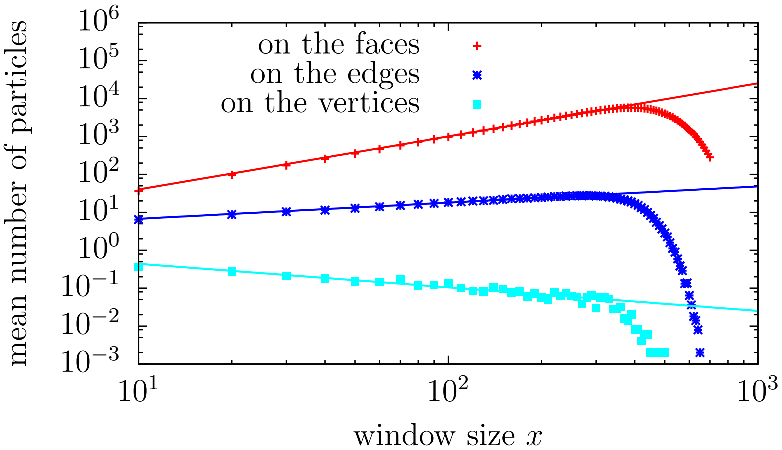

Figure 6.11.: The mean number of particles on the faces, edges, and vertices of the observation box of 1,000 three dimensional DLA clusters due to the observation box size is plotted. The DLAs consist out of 1,000,000 particles

ν	0	1	2	3	4	5
d_ν	2.41	1.41	0.41	-0.59	$d_0 - 2$	$d_1 - 2$
$w_{0;\nu}$	0.344 ± 0.015	–	–	–	–	–
$w_{1;\nu}$	0.389 ± 0.017	-0.109 ± 0.013	–	–	–	–
$w_{3;\nu}$	$-0.0041 \pm 6.56 \cdot 10^{-5}$	0.757 ± 0.093	??	??	–	–
$w_{0;\nu}^{2,0}$	0.161 ± 0.016	–	–	–	??	–
$w_{1;\nu}^{0,2}$	0.389 ± 0.017	0.109 ± 0.0133	–	–	–	–
$w_{2;\nu}^{0,2}$	1.634 ± 0.072	0.375 ± 0.011	??	–	–	–

Table 6.4.: This table determines the mean Minkowski functionals of 1,000 three dimensional DLAs with 1,000,000 particles up to the rank-2 tensors (see Eq. (3.15)). The fractal dimension, the subdimensions, and the corresponding fractal amplitudes are listed. The sign "**??**" means that the standard deviation is too large, such that the information is not useful.

the DLA structure. Here the number of particles on the frame of each observation box is counted and plotted in Fig. 6.11. The fractal dimension of this fractal is $d_{f,\text{edge}} = 0.427 \pm 0.016$. This dimension can be identified as the mean curvature subdimension $d_2 = d_f - 2$.
The last fractal set is the intersection of the DLA cluster and the vertices of the observation window. The particles on the vertices are counted for each observation box and plotted in Fig 6.11 as well. The fractal dimension of this fractal set is $d_{f,\text{vertex}} = -0.621 \pm 0.007 \approx d_f - 3$. This is the Gaussian curvature subdimension d_3 of the 3D DLA. These calculation show the same rule Eq. (6.1) for the dimensions of the hidden fractals living on the ν-th smaller topological dimension.

To determine the amplitudes, the data is fitted by the functions of Eq. (3.15) using $d_f = 2.41$. As in two dimensions there are terms of $W_2^{2,0}$ and $W_3^{2,0}$ which have to be merged. The exponents are equal due to Eq. (6.1). However, the standard deviations of some amplitudes are too large to state accurate results. They are not plotted in Table 6.4.

6.3. Percolation

Another often used model for many physical, biological, and material scientific processes is the so called percolation theory. The field of percolations is very broad which can be seen by the number of models covered by percolation theory. For instance, a model which is related with percolation theory; namely the Mandelbrot percolation in chapter 4.2 was already mentioned in this thesis. In chapter 4.2.3 the site-percolation was also addressed. This site-percolation is the most studied percolation model as well as the bond-percolation. Both are introduced by S. R. Broadbental and J. M. Hammersley [51]. Often the passage of liquids in porous materials and the deposition of oil are mentioned as explicit examples of processes described by site- and bond-percolation [52, 53].

The *site-percolation* is based on a lattice which does not necessarily has to be finite. Every lattice point is occupied with a probability p independently from all other lattice points. Two directly adjacent points – with regards to the chosen lattice – are defined as linked if both points are occupied. An typical site-percolation system on a square grid is shown in Fig. 6.12.
The *bond-percolation* is based on a periodic lattice as well. Here the lattice points are all occupied. However, the points are not linked with their direct neighbours automatically. The edges between two points symbolize that the link only exists with the probability p independently from the existence of all other links. To picture this structure between the lattice points further points are inserted which denote the links. A typical system emerging out of bond-percolation on a square grid is shown in Fig. 6.12.

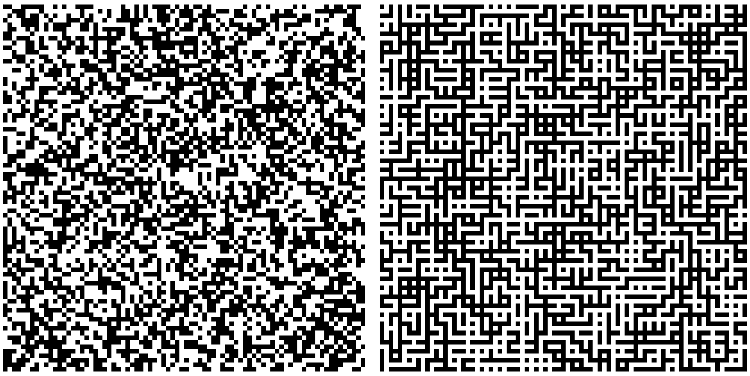

Figure 6.12.: Site- (left) and bond-percolation (right) on a 40×40 square lattice.

6.3.1. Critical Behavior and Self Similarity

In this section one has to clarify what type of fractal is investigate. Possible fractals to investigate are the whole percolation systems built with different probability p. However, these fractals are related to the already analyzed random iterated fractals in chapter 4. Especially the similarity with the IRC was revealed (compare

dimension	lattice type	site	bond
2	triangular	0.5	$2\sin(\frac{\pi}{18}) \approx 0.34729$
	square	≈ 0.592746	0.5
	honeycomb	≈ 0.6962	$1 - 2\sin(\frac{\pi}{18}) \approx 0.65271$
3	cubic	≈ 0.3116	≈ 0.2488
	diamond	≈ 0.43	≈ 0.388
	bcc	≈ 0.2464	≈ 0.1803
	fcc	≈ 0.198	≈ 0.119

Table 6.5.: The critical probabilities on different type of lattices in 2 and three dimensions are listed [40]. The elements of the clusters are only linked with the nearest neighbors and there are no correlations between different points or links.

with chapter 4.2.3). This would give no further information.

To generate another, more interesting fractal the probability of percolation p_{perc} and the critical probability p_c has to be considered as for the Mandelbrot percolation. Percolation indicates if at least one cluster exists which connects the bottom with the top boundary of the lattice. If the lattice is infinitely large, percolation indicates if there exists at least one cluster which connects two parallel lines with arbitrary distance. By observing the relation between p and p_{perc}, one notices a phase transition. For an infinite lattice p_{perc} jumps form 0 to 1 at the critical probability p_c. At that point the system barely percolates. The cluster which traverses the system is called the *percolation cluster* (PC). The crucial property of these clusters is that they are self similar under scaling. Consequently, the percolation cluster is a random fractal structure.

Now a suitable lattice to construct the fractal structures has to be chosen. Some of the critical probabilities are listed in Table 6.5. The probabilities show that some of them are determined exactly and some are approximated. To investigate a proper fractal, only the lattice types with exact critical probability are appropriate for further investigations. These percolations are the site-percolation on a triangular grid and the bond-percolation on a triangular, square and honeycomb grid. Because it is simplest to implement a percolation cluster on a square lattice, the bond-percolation on this grid is chosen. The exact procedure of building PCs with this kind of grid is discussed in the next section.

6.3.2. Construction

Constructing a bond-percolation on a square grid, the lattice points of the first row of the grid are alternatingly occupied and not occupied. This is done for every uneven row. In every even row the lattice points are not occupied, such that every occupied point is separated by an unoccupied point with another occupied point. This is the preparation for the actual percolation. Every occupied lattice point represents an element of the bond-percolation.

The second part is to introduce the links between neighboring percolation lattice points. Firstly, the first element in the first row is chosen. This point is connected with the next point in the same row with probability $p_c = 0.5$ and with the next point in the same column with probability $p_c = 0.5$. This procedure is done for every element of the percolation grid. Now the connections are set. If two neighboring elements are connected, the lattice points between both elements is occupied representing the link. In addition the percolation system is clustered and tested if there are clusters which traverse the lattice from the top to the bottom. The algorithm which is used here to check percolation is the Hoshen-Kopelman algorithm [55]. The non percolating clusters are removed. The remaining structure is the percolation cluster. A sketch of the construction is shown in Fig. 6.13.

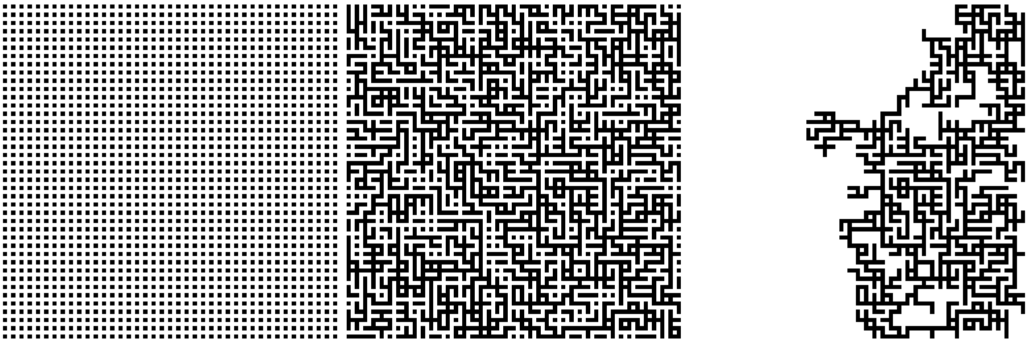

Figure 6.13.: The steps of constructing the percolation clusters is sketched in this figure on a 40×40 square lattice. In the first picture the initial setup is seen. In the second picture the links are introduced individually with the probability $p = 0.5$. In the last picture only the non percolating clusters are removed. Only the PC is left.

6.3.3. Minkowski functionals

To calculate the Minkowski functionals 1,000 bond-percolation clusters on a 2,000×2,000 large lattice are constructed. Therefore, the cluster is saved by an im-

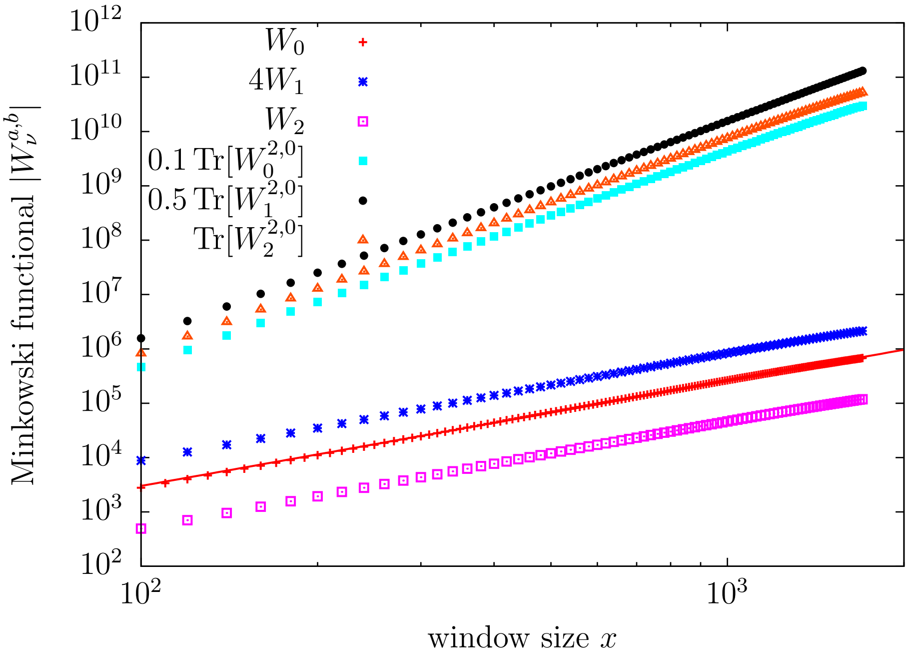

Figure 6.14.: The progression of the Minkowski functioals of 1000 two dimensional bond-percolation clusters due to the observation window size is plotted. The clusters are built on a 2000x2000 square lattice with $p = 0.5$.

age. The Minkowski functionals of the pixelated data is calculated by Papaya for different observation window sizes. The results can be seen in Fig. 6.14. The mean fractal dimension of the clusters is $d_f = 1.927 \pm 0.002$. This is in agreement with the literature value $d_{f,lit} = \frac{91}{48} \approx 1.896$ [54]. In this plot also the other Minkowski functionals show the expected scaling. The dominant terms are d_f and $d_f + 2$ for

functional $W_\nu^{a,b}$	constant c	slope $\Delta_1 d$	first subdimension d_1
W_1	0.79077	-1.087±0.130	0.840±0.130
W_2	0.1747	-1.017±0.043	0.910±0.043
$\mathrm{Tr}[W_0^{2,0}]$	0.160	–	–
$\mathrm{Tr}[W_1^{2,0}]$	0.1312	–	–
$\mathrm{Tr}[W_2^{2,0}]$	0.0284	–	–

Table 6.6.: The mean values of the subtracted constants, slopes, and calculated subdimensions of 1,000 percolation clusters are listed. The clusters are built on a 2,000×2,000 square lattice using bond-percolation and the critical probability $p_c = 0.5$. The fractal dimension is $d_f \approx 1.927$.

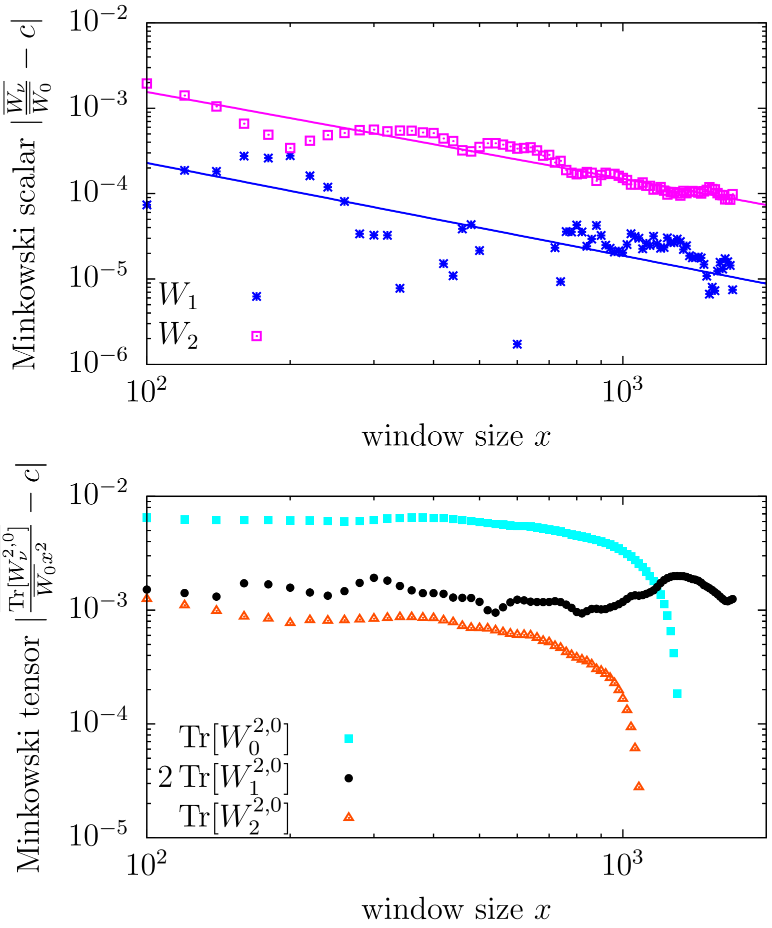

Figure 6.15.: The modified data of the Minkowski functionals of 1,000 two dimensional bond-percolation clusters due to the observation window size is plotted. The clusters are built on a 2,000×2,000 square lattice with $p = 0.5$. The data is modified in the way described in chapter 2.3.2. The constants c and the slopes Δd can be seen in Tabular 6.6.

all functionals.

The first analysis of the Minkowski functionals with the modified Sandbox method indicates a surface subdimension $d_1 \approx 0.840$ in the case of percolation (see Fig. 6.15 and Table 6.6). This is calculated from the slope of W_1. By calculating the dimension difference $\Delta_1 d \approx -1$ the similarity to the DLA clusters becomes apparent. It seems that for random fractals strengthen our hypothesis that $\Delta_1 d = -1$. Also for W_2 the subdominant dimension is close to $d_f - 1$. Nevertheless, the investigation of the tensors proves to be difficult. On the one hand

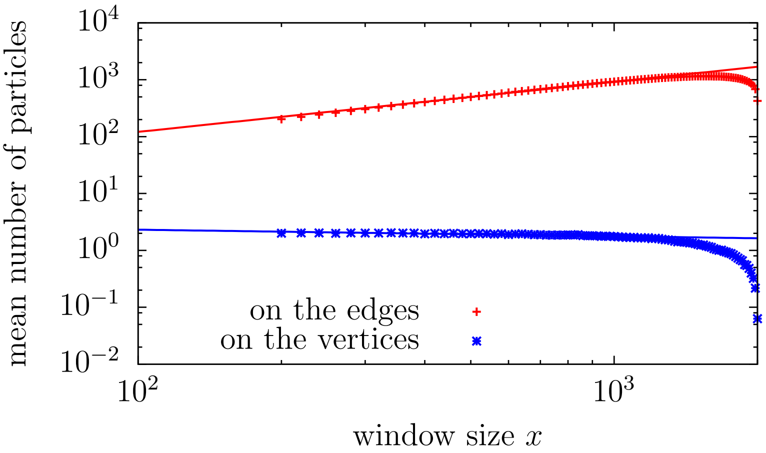

Figure 6.16.: The number of particles on the edges and vertices of the observation window of 1,000 two dimensional bond-percolation clusters due to the observation window size is plotted. The clusters are built on a 2,000×2,000 square lattice with $p = 0.5$.

the tensors show clearly the existence of subdimensions. On the other hand c is difficult to determine and the data does not straighten up properly due to high noise. The calculation of the slopes is not reasonable (see Fig. 6.15). Thus, no subdimension are given for the tensors in Table 6.6.

6.3.4. Boundary Fractals

To get more precise results, the fractal dimensions of the observation window boundary fractals have to be calculated. The fractal dimensions of these are calculated analogously to the dimensions of the DLA. For every observation window size the lattice points which belong to the percolation cluster and lie on the rim and the vertex, respectively, are counted. The data is plotted in Fig 6.16. The resulting subdimensions are $d_1 = 0.880 \pm 0.007$ which is the same as calculated with the modified Sandbox method and $d_2 = -0.116 \pm 0.008$. This strengthens the assumption that the subdimensions are determined by the boundary fractals. The simple rule in Eq. (6.1) seems to pertain for this random fractal as well.

To calculate the amplitudes the data of the functionals is fitted by the corresponding functions of Eq. (3.11) using $d_f = 1.927$. The amplitudes are shown in Table 6.7. Some subdimensional amplitudes are not given because the standard deviations of the subdimensional amplitudes are too large again. Along with it the tensors $W_\nu^{2,0}$ are difficult to analyze properly, such that we restrict ourselves

ν	0	1	2	3
d_ν	1.927	0.927	-0.073	$d_0 - 2$
$w_{0;\nu}$	0.436 ± 0.007	–	–	–
$w_{1;\nu}$	0.347 ± 0.008	-0.017 ± 0.016	–	–
$w_{2;\nu}$	-0.0775 ± 0.0018	-0.073 ± 0.022	**??**	–
$w_{0;\nu}^{2,0}$	$0.121(\pm 0.004)$	–	–	**??**
$w_{1;\nu}^{0,2}$	0.347 ± 0.008	-0.017 ± 0.016	–	–
$w_{1;\nu}^{2,0}$	$0.029(\pm 0.0001)$	**??**	–	**??**
$w_{2;\nu}^{2,0}$	$-0.021(\pm 0.0007)$	**??**	**??**	**!!**$_2$

Table 6.7.: This table defines the mean Minkowski fuctionals of the 1,000 2,000×2,000 PCs up to the rank-2 tensors (see Eq. (3.11)). The fractal dimension, the subdimensions, and the corresponding fractal amplitudes are listed. The sign "**??**" means that the standard deviation is too large, such that the information is not useful. The sign "**!!**" is intended to call attention that the term of this amplitude has the same exponent as one of the terms before. The index shows to which term this applies.

exponent	α	β	γ	η	ν	σ	τ
values	$-\frac{2}{3}$	$\frac{5}{36}$	$\frac{43}{18}$	$\frac{5}{24}$	$\frac{4}{3}$	$\frac{36}{91}$	$\frac{187}{91}$

Table 6.8.: The critical exponents of the two dimensional percolation system is listed [40, 41].

to the dominant term in these cases.

The question arises: do these amplitudes contain any information about the percolation threshold? The quantities which come in mind by talking about percolation threshold are the critical exponents. The critical exponents are already addressed in the beginning of my thesis (see chapter 1). They describe the behavior of certain quantities at p close or at p_c. For the site- and bond-percolation the critical exponents are equal due to universality. They are listed in Table 6.8. Comparing them with the dominant amplitudes no accordance and no direct dependence is observable. Admittedly some critical exponents lie close to the subdimensional terms, but they do not lie within the numerical errors. As a consequence, it can not be proven if the amplitudes reveal informations about percolation.

7. Conclusion

The aim of this thesis was to analyze and investigate fractal structures in two and three dimensional by extending the method of fractal dimensions. The scaling behavior of different properties namely the Minkowski functionals were examined. The fractals were constructed and the Minkowski functionals were calculated within different sized observation windows for the purpose of the Sandbox method. This is done numerically and analytically if possible. First, iterated fractals in two and three dimensions were obtained. The calculation showed that the Minkowski functionals possess subdominant terms next to the fractal terms. Also for the random iterated and fully random fractals these subterms became observable. In general, a pyramidic shape became apparent. For every quantity which is based on the next smallest topological dimension the corresponding Minkowski scalar aquires an additional term. The tensors $W_\nu^{0,2}$ have the same subdimensions as the scalars W_ν they are based on. By calculating the tensors $W_\nu^{2,0}$ one has to be careful that the subdimensions increase by 2. Next to these terms the unmodified fractal term and in the three dimensional case also the unmodified surface subterm is existent. From some examples, namely the diffusion limited aggregation and the bond-percolation, it was shown that the subdimensions are $d_1 = d_f - 1$, $d_2 = d_f - 2$, and $d_3 = d_f - 3$. However, some iterated fractals, like the Sierpiński carpet and the Menger's sponge, and random iterated fractals, like the Mandelbrot percolation cluster and the generalized random carpet, serve as counterexamples that this behavior does not hold for all subdimensions. Consequently, the subdimensions are not directly dependent of the fractal dimension.

To determine the cause of the subterms complex dimensions, zeta functions, and the involved dimensional oscillations were investigated. It was proven that the construction algorithm of the iterated fractals cancels the oscillation. Eventually the subdimensions could be identified with the fractal dimensions of structures which are hidden in the observed fractal. Therefore, the topological dimension of the fractals is lowered by observing the intersection between the fractal and the contour of the window. The zeta functions of these structures are called face and edge zeta functions.

The subdimensional amplitudes do contain structural information. This was shown by analyzing the Mandelbrot percolation, the generalized random carpet, and the bond-percolation cluster. Therefore, the clusters were separated into different phases with respect to the system parameter p. Thus, it was shown that some transition thresholds of the Mandelbrot percolation are contained within the subdimensional terms. Even more, in addition to the three known thresholds [36, 37] another threshold within the third phase can be introduced. It separates a non percolating cluster dominated system and a non percolating hole dominated system. A fifth phase was determined. However, links between the most interesting transition, the percolation threshold, could either be discounted or not determined. This yields both for the percolation probability and the critical exponents. In course of this the percolation thresholds of the Mandelbrot percolation and the generalized random carpet was calculated numerically performing finite size scaling. Despite the Minkowski fuctionals of both clusters being statistically equal, the thresholds differ. Furthermore, a transition due to p_c from the random carpet to the bond-percolation was discovered. This is done by choosing different types of generalized random carpets.

Nevertheless, it became obvious that the modified Sandbox method which makes just the subdominant terms visible is not satisfying. The problem of this method is that the constants which have to be subtracted are very hard to determine. Particularly since it is rather sensitive on small variations. Additionally, only the subdominant terms can be determined. A better method is to calculate the fractal dimensions of the hidden fractals withn the boundary of the observation window and determine the subdimensional amplitudes by fitting properly though the standard deviations of the subdimensions become large as well. It is wise to rethink and to improve this methods.

Further on, it is interesting to continue to treat the subterms and the fractal structures. Here some issues are worth thinking about.

- Analyzing a wider range of fractals to detect possible connections between geometry and, i.e., phase transitions. In the course of this it is reasonable to analyze structures with similar fractal dimensions or Minkowski functionals to determine similarities which affects the subdimensional amplitudes.
- Clarifying the use of the Minkowski tensors for different structures. One noticed that the exponents of the tensors do not contain additional information. The question arises if this also pertains for the subdimensional amplitudes of the tensors.
- Increasing the structures in size to get more accurate results. Thus it is also worthwhile to reinvestigate the random fractals covered in this thesis (number of particles, size of the grid).

- Finding ways to determine subamplitudes in a better way.
- Extending the topological dimension to arbitrary dimensions.
- Analyzing the Mandelbrot percolation and the generalized random carpets further also in addition to the subdimensions. These fractals are hardly covered in literature. The only research results are to give limits in which p_c is located analytically [38].

In general, the whole topic of fractal subterms is an interesting subject which still has potential for more investigations.

Bibliography

[1] MANDELBROT B.B., 1983, *The fractal geometry of nature* W. H. Freeman and Company, New York, vol. **3**

[2] KATZ D.M., 2010, *How Long is the Coastline of the Law: Additional Thoughts on the Fractal Nature of Legal Systems* URL: http://computationallegalstudies.com/2010/10/18/how-long-is-the-coastline-of-the-law-additional-thoughts-on-the-fractal-nature-of-legal-systems

[3] MANDELBROT B.B., 1967, *How long is the coast of Britain? Statistical self-similarity and fractional dimension* Science, vol. **156** pp. 636–638

[4] FALCONER K.J., 1993, *Fraktale Geometrie: mathematische Grundlagen und Anwendungen* Spektrum, Akad. Verl., Heidelberg Berlin Oxford

[5] HALVIN S., BULDYREV. S.V., GOLDBERGER A.L., MANTENGA R.N., OSSADNIK S.M.,PENG C.K., SIMONS M., STANLEY H.E., 1995, *Fractals in biology and medicine* Chaos Solitons & Fractals, vol. **6** pp. 171–201

[6] KENKEL N.C., WALKER D.J., 1996, *Fractals in the biological sciences* Coenoses, vol. **11** pp. 77-100

[7] EVERTSZ C.J.G., 1995, *Fractal Geometry of Financial Time Series* Fractals, vol. **3** no. 3 pp. 609–616

[8] MARTINS C.J.A.P., SHELLARD E.P., 2006, *Fractal properties and small-scale structure of cosmic string networks* Physical Review D, vol. **73**

[9] HECK A., PERDANG J.M., 1991, *Applying Fractals in Astronomy* Springer-Verlag, Berlin Heidelberg New York, vol. **3**

[10] SUZUKI M., 1983, *Phase Transition and Fractals* Progress of Theoretical Physics, vol. **69** Issue 1 pp. 65–76

[11] STINCHCOMBE R.B., COURTENS E., 1989, *Fractal, Phase Transition and Criticality [and Discussion]* Proceedings of the Royal Society A, vol. **423** no. 1864 pp. 17-33

[12] GLEICK J., 1988, *Vorstoß in Grenzbereiche der modernen Physik* Droemer Knaur, München, p. 142

[13] VICSEK T., 1983, *Fractal models for diffusion controlled aggregation* Journal of Physics A: Mathematical and General, vol. **16** L647

[14] FRASER S.J., 1988, *Solvable random-decimation model of cluster scaling* Physical Review A, vol. **38** pp. 953–961

[15] MECKE K., 2000, *Additivity, Convexity, and Beyond: Applications of Minkowski Functionals in Statistical Physics* Lecture Notes in Physics, vol. **554** pp. 111–184

[16] STANLEY H.E., 1971, *Introduction to phase transitions and critical phenomena* Oxford University Press, London, vol. **1** pp. 39–52

[17] GEBHARD W.,KREY U., 1980, *Phasenübergänge und kritische Phänomene* Vieweg, Braunschweig Wiesbaden, pp. 74–81

[18] ARNS C., KNACKSTEDT M., MECKE K., 2004, *Characterisation of irregular spatial structures by parallel sets and integral geometric measures* Colloids and Surfaces A, vol. **241** no. 1–3 pp. 351–372

[19] MECKE K. and ARNS C., 2005, *Fluids in porous media: a morphometric approach* Journal of Physics: Condensed Matter, vol. **17** pp. 503–534

[20] MECKE K., 2000, *Additivity, convexity, and beyond: Applications of Minkowski functionals in statistical physics, in Statistical Physics and Spatial Statistics – The Art of Analyzing and Modeling Spatial Structures and Patterns* ser. Lecture Notes in Physics, K. Mecke and D. Stoyan, Eds., Springer Verlag, vol. **554** pp. 111–184

[21] BLACKADDER D., GRAY R., McCRUM N., 1976, .*The anisotropy of linear polyethylene single crystal mats* Journal of Polymer Science: Polymer Physics Edition, vol. **14** pp. 769–771

[22] ATANASOV I.S., DURRELL J.H., VULKOVA L.A., BARBER Z.H., YORDANOV O.I., 2006, *Statistical characterization of surface morphologies* Physica A, vol. **371** pp. 361–367

[23] MECKE K., WAGNER H., 1991, *Euler characteristic and related measures for random geometric sets* Journal of Statistical Physics, vol. **64** Issue 3-4 pp 843-850

[24] MECKE K., BUCHERT T., WAGNER H., 1994, *Robust Morphological Measures for Large-Scale Structure in the Universe* Astronomy & Astrophysics, vol. **288** pp. 697–704

[25] SCHRÖDER-TURK G.E., KAPFER S., BREIDENBACH B., BEISBART C., MECKE K., 2010, *Tensorial Minkowski functionals and anisotropy measures for planar patterns* Journal of Microscopy, vol. **238** pt. 1 pp. 57–74

[26] SCHRÖDER-TURK G.E., MICKEL W., KAPFER S.C., SCHALLER F.M., BREIDENBACH B., HUG D., MECKE K., 2013, *Minkowski Tensors of Anisotropic Spatial Structure* New Journal of Physics, vol. **15**

[27] MÜLLER H., 1953, *Über Momente ersten und zweiten Grades in der Integralgeometrie* Rendiconti del Circolo Matematico di Palermo (Series II), vol. **2** pp. 119– 140

[28] HUG D., SCHNEIDER R., SCHUSTER R., 2008, *Integral geometry of tensor valuations* Advances in Applied Mathematics, vol. **41** pp. 482–509

[29] ALESKER S., 1999, *Description of continuous isometry covariant valuations on convex sets* Geometriae Dedicata, vol. **74** pp. 241–248

[30] KNÜFING L., SCHOLLMEYER H., RIEGLER H., MECKE K., 2005 *Fractal Analysis Methods for Solid Alkane Monolayer Domains at* SiO_2*/Air Interfaces* Langmuir , vol. **21** pp. 992–1000

[31] STEEB W., 2008, *THE NONLINEAR WORKBOOK – Forth EDITION: Chaos, Fractals, Cellular Automata, Neutral Networks, Genetic Algorithms, Gene Expression Programming, Support Vector Machine, Wavelets, Hidden Markov Models, Fuzzy Logic with C++, Java and Symbolic C++ Programs* World Scientific Publishing Co. Pte. Ltd., vol. **4** p. 219f

[32] SIERPIŃSKI, W., 1916, *Sur une courbe cantorienne qui contient une image biunivoque et continue de toute courbe donnée* Comptes Rendus Hebdomadaires des Séances de l'Académie des Sciences Paris, vol. **162** pp. 629–632

[33] FEDER J., 1988, *Fractals* Plenum Press, New York, vol. **3** p. 24f.

[34] MENGER K., 1926, *Allgemeine Räume und Cartesische Räume* I. Mitteilung, Proc. Ac. Amsterdam, vol. **29** p. 476

[35] MANDELBROT B.B., 1974, *Intermittent turbulence in self-similar cascades divergence of high moments and dimension of the carrier* Journal of Fluid Mechanics, vol. **62** pp. 331–358

[36] DEKKING F.M., MEESTER R.W.J., 1989, *On the Structure of Mandelbrot's Percolation Process and Other Random Cantor Sets* Journal of Statistical Physics, vol. **58** pp. 1109–1126

[37] FALCONER K.J., GRIMMETT G., 1992, *On the Geometry of Random Cantor Sets and Fractal Percolation* Journal of Probability, vol. **5** pp. 465–485

[38] DON H., 2014, *New Methods to Bound the Critical Probability in Fractal Percolation* Wiley Online Library (wileyonlinelibrary.com), DOI 10.1002/rsa.20566

[39] CARDY L., 1988, *Finite-Size Scaling* Elsevier Science Publishers, Amsterdam, vol. **2**

[40] STAUFFER D., 1985, *Introduction to percolation theory* Taylor & Francis Ltd, London

[41] GRIMMETT G., 1999, *Percolation* Springer, New York, 1. edition pp. 232–279

[42] JACOBSEN J.L., 2014, *High-precision percolation thresholds and Potts-model critical manifolds from graph polynomials* Journal of Physics A: Mathematical and Theoretical, vol. **47** 135001

[43] LAPIDUS M.L., van FRANKENHUIJSEN M., 2006, *Fractal Geometry, Complex Dimensions and Zeta Functions: Geometry and Spectra of Fractal Strings* Springer, New York, 1. edition

[44] LAPIDUS M.L., POMERANCE C., 1996, *Counterexamples to the modified Weyl-Berry conjecture on fractal drums* Mathematical Proceedings of the Cambridge Philosophical Society, vol. **119** pp. 167–178

[45] HUTCHINSON J.E., 1981, *Fractals and self-similarity* Indiana University Mathematics Journal, vol. **30** pp. 713–747

[46] HAMBLY B.M., LAPIDUS M.L., 2006, *Random fractal strings: Their zeta functions, complex dimensions and spectral asymptotics* Transactions of the American Mathematical Society, vol. **358** pp. 285–314

[47] LAPIDUS M.L., ROCK J.A., ŽUBRINIĆ D., 2013, *Box-counting fractal strings, zeta functions, and equivalent forms of Minkowski dimension* Contemporary Mathematics – American Mathematical Society, Providence, RI

[48] WITTEN T.A., SANDER L.M., 1981, *Diffusion-Limited Aggregation, a Kinetic Critical Phenomenon* Physical Review Letters, vol. **47** pp. 1400–1403

[49] MANDELBROT B.B., VESPIGNANI A., KAUFMAN H., 1995, *Crosscut analysis of large radial DLA: departures from self-similarity and lacunarity effects* Europhysics Letters, vol. **32** pp. 199–204.

[50] TOLMAN S., MEAKIN P., 1989, *Off-lattice and hypercubic-lattice models for diffusion-limited aggregation indimensionalities 2–8* Physical Review A, vol. **40** pp. 428–437

[51] BROADBENT S.R., HAMMERSLEY J.M., 1957, *Percolation processes I. Crystals and mazes* Proceedings of the Cambridge Philosophical Society, vol. **53**, pp. 629–641

[52] BERKOWITZ B., EWING R.P., 1998, *Percolation Theory and Network Modeling Applications in Soil Physics* Surveys in Geophysics, vol. **19** pp. 23–72

[53] KING P., ANDRARE Jr. J.S., BULDYREV S.V.,DOKHOLYAN N., LEE Y., HALVIN S., STANLEY H.E., 1999, *Predicting oil recovery using percolation* Physica A: Statistical Mechanics and its Applications, vol. **266** pp. 107–114

[54] SAHIMI M., 1994, *Applications of percolation theory* Taylor & Francis Ltd, London

[55] HOSHEN J., KOPELMAN R., 1976, *Percolation and cluster distribution. I. Cluster multiple labeling technique and critical concentration algorithm* Physical Review B, vol. **14** p. 3438

A. Analytical Calculation of the Sierpiński Carpet

In this Appendix the Minkowski functionals of the Sierpiński carpet are calculated analytically.
We start with $\mathbf{W_0}$. For every iterated step n the pre fractal set is simply translated by eight maps. It yields

$$\begin{aligned} W_0(n+1) = & 8W_0(n) \qquad W_0(0) = 1 \\ \Rightarrow & W_0(n) = 8^n. \end{aligned} \tag{A.1}$$

For the calculation of $\mathbf{W_1}$ next to the eight maps some edges at the rim has to be removed for every step

$$W_1(n+1) = 8W_1(n) - 8 \cdot 3^n. \tag{A.2}$$

Consequently, the ansatz is $W_1(n) = A \cdot 8^n + B \cdot 3^n$ by which simply an equation system has to be calculated

$$\begin{aligned} W_1(0) &= 2 = A + B \\ W_1(1) &= 8 = 8A + 3B \\ \Rightarrow W_1(n) &= \frac{2}{5}8^n + \frac{8}{5}3^n. \end{aligned} \tag{A.3}$$

The progression of $\mathbf{W_2}$ is

$$W_2(n+1) = 8W_2(n) - 8\pi. \tag{A.4}$$

The equation system is

$$\begin{aligned} W_2(0) &= \pi = A + B \\ W_2(1) &= 0 = 8A + B \\ \Rightarrow W_2(n) &= -\frac{1}{7}\pi 8^n + \frac{8}{7}\pi. \end{aligned} \tag{A.5}$$

The same yields for $\mathrm{Tr}[\mathbf{W_1^{0,2}}]$.

To calculate $\mathrm{Tr}[W_\nu^{2,0}]$ the formula of Eq. (2.6) is needed with $t_{ij} = 3^{2n}\delta_{ij}$. So it yields for $\mathrm{Tr}[\mathbf{W_0^{2,0}}]$

$$\begin{aligned}\mathrm{Tr}[W_0^{2,0}](n+1) &= 8\,\mathrm{Tr}[W_0^{2,0}](n) + 6\cdot 3^{2n}\cdot 2W_0(n)\\ &= 8\,\mathrm{Tr}[W_0^{2,0}](n) + 12\cdot 72^n.\end{aligned} \tag{A.6}$$

The equation system is

$$\begin{aligned}\mathrm{Tr}[W_0^{2,0}](0) &= \frac{1}{6} = A + B\\ \mathrm{Tr}[W_0^{2,0}](1) &= \frac{40}{3} = 72A + 8B\\ \Rightarrow \mathrm{Tr}[W_0^{2,0}](n) &= \frac{3}{16}72^n - \frac{1}{48}8^n.\end{aligned} \tag{A.7}$$

For $\mathrm{Tr}[\mathbf{W_1^{2,0}}]$ it yields

$$\begin{aligned}\mathrm{Tr}[W_1^{2,0}](n+1) &= 8\,\mathrm{Tr}[W_1^{2,0}](n) + 6\cdot 3^{2n}\cdot 2W_1(n) - \frac{26}{3}27^n - 27^n\\ &= 8\,\mathrm{Tr}[W_1^{2,0}](n) + \frac{24}{5}72^n + \frac{143}{15}27^n.\end{aligned} \tag{A.8}$$

The equation system is

$$\begin{aligned}\mathrm{Tr}[W_1^{2,0}](0) &= \frac{2}{3} = A + B + C\\ \mathrm{Tr}[W_1^{2,0}](1) &= \frac{56}{3} = 72A + 27B + 8C\\ \mathrm{Tr}[W_1^{2,0}](2) &= \frac{2176}{3} = 5184A + 729B + 64C\\ \Rightarrow \mathrm{Tr}[W_1^{2,0}](n) &= \frac{3}{40}72^n + \frac{128}{285}27^n + \frac{65}{456}8^n.\end{aligned} \tag{A.9}$$

For $\mathrm{Tr}[\mathbf{W_2^{2,0}}]$ it yields

$$\begin{aligned}\mathrm{Tr}[W_2^{2,0}](n+1) &= 8\,\mathrm{Tr}[W_2^{2,0}](n) + 6\cdot 3^{2n}\cdot 2W_2(n) - 3\pi 9^n\\ &= 8\,\mathrm{Tr}[W_2^{2,0}](n) - \frac{12\pi}{7}72^n + \frac{75\pi}{7}9^n.\end{aligned} \tag{A.10}$$

The equation system is

$$\begin{aligned}
\mathrm{Tr}[W_2^{2,0}](0) &= \frac{\pi}{2} = A + B + C \\
\mathrm{Tr}[W_2^{2,0}](1) &= 4\pi = 72A + 9B + 8C \\
\mathrm{Tr}[W_2^{2,0}](2) &= -76\pi = 5184A + 81B + 64C \\
\Rightarrow \mathrm{Tr}[W_2^{2,0}](n) &= -\frac{3}{112}\pi 72^n + \frac{12}{7}\pi 9^n - \frac{19}{16}\pi 8^n.
\end{aligned} \tag{A.11}$$

B. Analytical Calculations of the Menger's Sponge

In this Appendix the Minkowski functionals of the Menger's sponge are calculated analytically. One proceeds as in Appendix A.
We start with $\mathbf{W_0}$. For every iterated step n the pre fractal set is simply translated by 20 maps. It yields

$$\begin{aligned} W_0(n+1) =& 20W_0(n) \qquad W_0(0) = 1 \\ \Rightarrow& W_0(n) = 20^n. \end{aligned} \tag{B.1}$$

For the calculation of $\mathbf{W_1}$ next to the 20 maps, some faces at the rim has to be removed for every step which are the Sierpiński carpet at this step

$$W_1(n+1) = 20W_1(n) - 2 \cdot 8 \cdot W_0(n)^{\text{Sierp}} = 20W_1(n) - 16 \cdot 8^n. \tag{B.2}$$

Consequently, the ansatz is $W_1(n) = A \cdot 20^n + B \cdot 8^n$ by which simply an equation system has to be calculated

$$\begin{aligned} W_1(0) &= 2 = A + B \\ W_1(1) &= 24 = 20A + 8B \\ \Rightarrow W_1(n) &= \frac{2}{3}20^n + \frac{4}{3}8^n. \end{aligned} \tag{B.3}$$

The progression of $\mathbf{W_2}$ is

$$W_2(n+1) = 20W_2(n) - 8\pi W_1(n)^{\text{Sierp}} = 20W_2(n) - \frac{16\pi}{5}8^n - \frac{64\pi}{5}3^n. \tag{B.4}$$

The equation system is

$$\begin{aligned} W_2(0) &= \pi = A + B + C \\ W_2(1) &= 4\pi = 20A + 8B + 3C \\ W_2(2) &= 16\pi = 400A + 64B + 9C \\ \Rightarrow W_2(n) &= -\frac{1}{51}\pi 20^n + \frac{4}{15}\pi 8^n + \frac{64}{85}\pi 3^n. \end{aligned} \tag{B.5}$$

The same yields for $\mathrm{Tr}[\mathbf{W_1^{0,2}}]$.

The progression of $\mathbf{W_3}$ is

$$W_3(n+1) = 20W_3(n) - 32\pi W_2(n)^{\mathrm{Sierp}} = 20W_3(n) + \frac{32\pi}{7}8^n - \frac{256\pi}{7}. \tag{B.6}$$

The equation system is

$$\begin{aligned} W_3(0) &= \frac{4\pi}{3} = A + B + C \\ W_3(1) &= -\frac{16\pi}{3} = 20A + 8B + C \\ W_3(2) &= -\frac{320\pi}{3} = 400A + 64B + C \\ \Rightarrow W_3(n) &= -\frac{4}{19}\pi 20^n - \frac{8}{21}\pi 8^n + \frac{256}{133}\pi. \end{aligned} \tag{B.7}$$

The same yields for $\mathrm{Tr}[\mathbf{W_2^{0,2}}]$.

To calculate $\mathrm{Tr}[W_\nu^{2,0}]$ the formula of Eq. (2.6) is needed with $t_{ij} = 3^{2n}\delta_{ij}$. So it yields for $\mathrm{Tr}[\mathbf{W_0^{2,0}}]$

$$\begin{aligned} \mathrm{Tr}[W_0^{2,0}](n+1) &= 20\,\mathrm{Tr}[W_0^{2,0}](n) + 16 \cdot 3^{2n} \cdot 3W_0(n) \\ &= 20\,\mathrm{Tr}[W_0^{2,0}](n) + 48 \cdot 180^n. \end{aligned} \tag{B.8}$$

The equation system is

$$\begin{aligned} \mathrm{Tr}[W_0^{2,0}](0) &= \frac{1}{4} = A + B \\ \mathrm{Tr}[W_0^{2,0}](1) &= 53 = 180A + 20B \\ \Rightarrow \mathrm{Tr}[W_0^{2,0}](n) &= \frac{3}{10}180^n - \frac{1}{20}20^n. \end{aligned} \tag{B.9}$$

For $\mathrm{Tr}[\mathbf{W_1^{2,0}}]$ it yields

$$\begin{aligned}\mathrm{Tr}[W_1^{2,0}](n+1) &= 20\,\mathrm{Tr}[W_1^{2,0}](n) + 16 \cdot 3^{2n} \cdot 3W_1(n) - 16\,\mathrm{Tr}[W_0^{2,0}](n)^{\text{ Sierp}} \\ &\quad - 36 \cdot 3^{2n} \cdot W_0(n)^{\text{ Sierp}} \\ &= 20\,\mathrm{Tr}[W_1^{2,0}](n) + 32 \cdot 180^n + 25 \cdot 72^n + \frac{1}{3}8^n.\end{aligned} \tag{B.10}$$

The equation system is

$$\begin{aligned}\mathrm{Tr}[W_1^{2,0}](0) &= \frac{5}{6} = A + B + C + D \\ \mathrm{Tr}[W_1^{2,0}](1) &= 74 = 180A + 72B + 20C + 8D \\ \mathrm{Tr}[W_1^{2,0}](2) &= \frac{27128}{3} = 180^2A + 72^2B + 20^2C + 8^2D \\ \mathrm{Tr}[W_1^{2,0}](3) &= \frac{4041824}{3} = 180^3A + 72^3B + 20^3C + 8^3D \\ \Rightarrow \mathrm{Tr}[W_1^{2,0}](n) &= \frac{1}{5}180^n + \frac{25}{52}72^n + \frac{211}{1170}20^n - \frac{1}{36}8^n.\end{aligned} \tag{B.11}$$

For $\mathrm{Tr}[\mathbf{W_2^{2,0}}]$ it yields

$$\begin{aligned}\mathrm{Tr}[W_2^{2,0}](n+1) &= 20\,\mathrm{Tr}[W_2^{2,0}](n) + 16 \cdot 3^{2n} \cdot 3W_2(n) - 8\pi\,\mathrm{Tr}[W_1^{2,0}](n)^{\text{Sierp}} \\ &\quad - 18\pi W_1(n)^{\text{ Sierp}} \\ &= 20\,\mathrm{Tr}[W_2^{2,0}](n) - \frac{48\pi}{51}180^n + 5\pi 72^n + \frac{3632\pi}{969}27^n - \frac{65\pi}{57}8^n.\end{aligned} \tag{B.12}$$

The equation system is

$$\begin{aligned}\mathrm{Tr}[W_2^{2,0}](0) &= \frac{7\pi}{12} = A + B + C + D + E \\ \mathrm{Tr}[W_2^{2,0}](1) &= \frac{55\pi}{3} = 180A + 72B + 27C + 20D + 8E \\ \mathrm{Tr}[W_2^{2,0}](2) &= \frac{1948\pi}{3} = 180^2A + 72^2B + 27^2C + 20^2D + 8^2E \\ \mathrm{Tr}[W_2^{2,0}](3) &= 11072\pi = 180^3A + 72^3B + 27^3C + 20^3D + 8^3E \\ \mathrm{Tr}[W_2^{2,0}](4) &= -\frac{9984208\pi}{3} = 180^4A + 72^4B + 27^4C + 20^4D + 8^4E \\ \Rightarrow \mathrm{Tr}[W_2^{2,0}](n) &= -\frac{1}{170}\pi 180^n + \frac{5}{52}\pi 72^n + \frac{3632}{6783}\pi 27^n - \frac{2251}{16380}\pi 20^n + \frac{65}{684}\pi 8^n.\end{aligned} \tag{B.13}$$

For $\mathrm{Tr}[\mathbf{W_3^{2,0}}]$ it yields

$$\begin{aligned}\mathrm{Tr}[W_3^{2,0}](n+1) &= 20\,\mathrm{Tr}[W_3^{2,0}](n) + 16\cdot 3^{2n}\cdot 3W_3(n) - 32\,\mathrm{Tr}[W_2^{2,0}](n)^{\mathrm{Sierp}} \\ &\quad - 72\cdot W_2(n)^{\ \mathrm{Sierp}} \\ &= 20\,\mathrm{Tr}[W_3^{2,0}](n) - \frac{192\pi}{19}180^n - \frac{50}{7}72^n - \frac{5954\pi}{133}9^n + 30\pi 8^n.\end{aligned} \tag{B.14}$$

The equation system is

$$\begin{aligned}\mathrm{Tr}[W_3^{2,0}](0) &= \pi = A + B + C + D + E \\ \mathrm{Tr}[W_3^{2,0}](1) &= -4\pi = 180A + 72B + 20C + 9D + 8E \\ \mathrm{Tr}[W_3^{2,0}](2) &= -2512\pi = 180^2A + 72^2B + 20^2C + 9^2D + 8^2E \\ \mathrm{Tr}[W_3^{2,0}](3) &= -415872\pi = 180^3A + 72^3B + 20^3C + 9^3D + 8^3E \\ \mathrm{Tr}[W_3^{2,0}](4) &= -69930560\pi = 180^4A + 72^4B + 20^4C + 9^4D + 8^4E \\ \Rightarrow \mathrm{Tr}[W_3^{2,0}](n) &= -\frac{6}{95}\pi 180^n - \frac{25}{182}\pi 72^n + \frac{641}{2145}\pi 20^n + \frac{5952}{1463}\pi 9^n - \frac{19}{6}\pi 8^n.\end{aligned} \tag{B.15}$$

C. Analytical Calculations of the Random Carpet

In this Appendix the mean Minkowski functionals of the Mandelbrot percolation and the generalized random carpet, respectively, are calculated analytically. One exploits that the mean functionals are statistically equal for all of these structures. These are calculated for the easiest structure $_2$RC. The functionals after a certain step are calculated for every possible structure which is constructible for the $_2$RC and weighted with the possibility that this very structure is constructed. To get the mean Minkowski functionals, they are summed up.

For every iterated step n the pre-fractal set is simply translated by four maps with probability p. It yields for $\mathbf{W_0}$

$$\begin{aligned} W_0(n+1) =& 4pW_0(n) \qquad W_0(0) = 1 \\ \Rightarrow& W_0(n) = (4p)^n. \end{aligned} \tag{C.1}$$

For the calculation of $\mathbf{W_1}$ next to the nine maps, some edges at the rim has to be removed for every step with probability p^2

$$W_1(n+1) = 4pW_1(n) - 4 \cdot (2p^2)^n. \tag{C.2}$$

Consequently, the ansatz is $W_1(n) = A \cdot (4p)^n + B \cdot (2p^2)^n$ by which simply an equation system has to be calculated

$$\begin{aligned} W_1(0) &= 2 = A + B \\ W_1(1) &= 8p - 4p^2 = 4pA + 2p^2 B \\ \Rightarrow W_1(n) &= \frac{4(1-p)}{2-p}(4p)^n + \frac{2p}{2-p}(2p^2)^n. \end{aligned} \tag{C.3}$$

For $\mathbf{W_2}$ it is difficult to calculate a progression. However one can proof the ansatz $W_2(n) = A(4p)^n + (2p^2)^n B + (p^4)^n C$ The equation system is

$$\begin{aligned}
&W_2(0) = \pi = A + B + C \\
&W_2(1) = \pi(p^4 - 4p^2 + 4p) = 4pA + 2p^2 B + p^4 C \\
&W_2(1) = \pi(p^8 + 4p^6 + 4p^5 - 8p^4 - 16p^3 + 16p^2) = 16p^2 A + 4p^4 B + p^8 C \\
\Rightarrow &W_2(n) = \frac{4\pi(2 - 3p + p^4)}{(2-p)(4-p^3)}(4p)^n + \frac{4\pi p(1-p^2)}{(2-p)(2-p^2)}(2p^2)^n + \frac{\pi p^3(2+p^2)}{(2-p^2)(4-p^3)}(p^4)^n.
\end{aligned} \tag{C.4}$$

The same yields for Tr[$\mathbf{W_1^{0,2}}$].

Because the assumption of Eq. (3.15) has vindicated so far, the progression is skipped and ansatz Tr[$\mathbf{W_0^{2,0}}$]$(n) = (16p)^n A + (4p)^n B$ is taken. The equation system is

$$\begin{aligned}
\mathrm{Tr}[W_0^{2,0}](0) &= \frac{1}{6} = A + B \\
\mathrm{Tr}[W_0^{2,0}](1) &= \frac{8p}{3} = 16pA + 4pB \\
\Rightarrow \mathrm{Tr}[W_0^{2,0}](n) &= \frac{1}{6}(16p)^n.
\end{aligned} \tag{C.5}$$

The Minkowski functionals of higher steps proves the ansatz true.

Consequently, one avoids the circuitous way of the progression and take directly the ansatz Tr[$\mathbf{W_1^{2,0}}$]$(n) = (16p)^n A + (4p)^n B + (8p^2)^n C$ as well. The equation system is

$$\begin{aligned}
&\mathrm{Tr}[W_1^{2,0}](0) = \frac{2}{3} = A + B + C \\
&\mathrm{Tr}[W_1^{2,0}](1) = \frac{20}{3}p - \frac{4}{3}p^2 = 16pA + 4pB + 8p^2 C \\
&\mathrm{Tr}[W_1^{2,0}](2) = \frac{272}{3}p^2 - \frac{112}{3}p^3 - \frac{32}{3}p^4 = 256p^2 A + 16p^2 B + 64p^4 C \\
&\mathrm{Tr}[W_1^{2,0}](2) = \frac{4160}{3}p^3 - \frac{1984}{3}p^4 - \frac{896}{3}p^5 - \frac{256}{3}p^6 = 4096p^3 A + 64p^3 B + 64512p^6 C \\
\Rightarrow &\mathrm{Tr}[W_1^{2,0}](n) = \frac{2(1-p)}{3(2-p)}(16p)^n + \frac{1-p}{3(1-2p)}(4p)^n - \frac{p(1+p)}{3(1-2p)(2-p)}(8p^2)^n.
\end{aligned} \tag{C.6}$$

The ansatz of $\mathrm{Tr}[\mathbf{W_2^{2,0}}]$ is $\mathrm{Tr}[\mathbf{W_2^{2,0}}](n) = (16p)^n A + (4p)^n B + (8p^2)^n C + (4p^4)^n D$. The equation system is

$$\begin{aligned}
\mathrm{Tr}[W_2^{2,0}](0) &= \pi = A + B + C + D \\
\mathrm{Tr}[W_2^{2,0}](1) &= 4\pi p - 2\pi p^2 = 16pA + 4pB + 8p^2C + 4p^4D \\
\mathrm{Tr}[W_2^{2,0}](2) &= 48\pi p^2 - 40\pi p^3 - 12\pi p^4 + 8\pi p^5 + 4\pi p^6 = 256p^2A + 16p^2B + 64p^4C + 16p^8D \\
\mathrm{Tr}[W_2^{2,0}](2) &= 704\pi p^3 - 672\pi p^4 - 304\pi p^5 + 72\pi p^6 + 144\pi p^7 + 40\pi p^8 + 32\pi p^9 + 16\pi p^{10} \\
&= 4096p^3A + 64p^3B + 64512p^6C + 64p^12D
\end{aligned}$$

$$\begin{aligned}
\Rightarrow \mathrm{Tr}[W_1^{2,0}](n) &= \frac{(1-p)(64-32p-32p^2-31p^3+p^4)}{48(2-p)(4-p^3)}\pi(16p)^n \\
&+ \frac{8-4p+2p^2-11p^3-p^4}{24(1-2p)(1+p+p^2)}\pi(4p)^n - \frac{p(1-p)(8+11p)(1+p)}{16(1-2p)(2-p)(2-p^2)}\pi(8p^2)^n \\
&+ \frac{p(8+7p+7p^2+6p^3+2p^4)}{8(2-p^2)(4-p^3)(1+p+p^2)}\pi(4p^4)^n.
\end{aligned} \tag{C.7}$$

Danksagung

Als Erstes will ich mich bei meinem Betreuer Prof. Dr. Klaus Mecke bedanken. Er hat es mir ermöglicht, über dieses sehr interessante und spannende Thema der Fraktale am Institut für Theoretische Physik I diese Masterarbeit zu schreiben. Durch seine stete Hilfe und seine Anmerkungen konnte ich sehr produktiv arbeiten. Die Diskussionen habe ich dabei sehr genossen, in denen er sehr offen für meine Vorschläge war. Ich konnte dadurch sehr viel lernen und mich als Physiker weiterentwickeln.

Als Zweites danke ich meinem zweiten Betreuer Matthias Hoffmann, der mir immer sehr gute Ratschläge gegeben hat. Vor allem bei Fragen zu Algorithmen und Simulationen hat er sich Zeit genommen und konnte mir immer weiterhelfen.

Des Weiteren danke ich PD Dr. Gerd Schröder-Turk und Fabian Schaller, die mir bei Fragen zu Papaya und Karambola zur Seite standen.

Ich danke Dr. Myfanwy Evans, Dr. Sebastian Kapfer, Ellen Fischermeier und Holger Mitschke für ihre Ratschläge.

Großer Dank geht auch an das ganze Institut für Theoretische Physik I, in der eine sehr entspannte Atmosphäre herrscht, sodass es sich dort sowohl sehr einfach arbeiten als auch diskutieren lässt.

Schlussendlich will ich ganz besonders meinen Eltern und meinem Bruder danken, die mich durch das ganze Studium tatkräftig begleitet und unterstützt haben. Ich konnte und kann mich immer auf sie verlassen.

Erklärung

Hiermit versichere ich, dass die vorliegende Masterarbeit von mir selbständig verfasst wurde und keine anderen Hilfsmittel oder Quellen neben den Angegebenen benutzt wurden. Zudem erkläre ich, dass alle Stellen dieser Arbeit, wenn sie wörtlich oder sinngemäß aus anderen Quellen übernommen wurden, so gut als möglich kenntlich gemacht sind und dass diese Arbeit in gleicher oder ähnlicher Form noch keiner anderen Prüfungsbehörde vorgelegt wurde.

Ort, Datum

Unterschrift